Temperature dependent segregation behaviour of stepped surfaces

Temperature dependent segregation behaviour of stepped surfaces

PROEFSCHRIFT

ter verkrijging van de graad van doctor aan de
Technische Universiteit Eindhoven, op gezag van de
Rector Magnificus, prof.dr. R.A. van Santen, voor een
commissie aangewezen door het College voor
Promoties in het openbaar te verdedigen
op donderdag 25 maart 2004 om 16.00 uur

door

Bearrach Moest

geboren te Eindhoven

Dit proefschrift is goedgekeurd door de promotoren:

prof.dr. H.H. Brongersma

en

prof.dr. B.E. Nieuwenhuys

Copromotor (postuum):

dr. A.W. Denier van der Gon

Voor de goede zorgen; aan mijn ouders

Introduction

<div align="right">

1

</div>

1.1 General introduction

Nature tries to minimize surfaces, yet we see them everywhere. The obvious reason is that every object is terminated by a surface. However, this corresponds to an (unfavourable) increase of the total energy as the creation of a surface involves the breaking of atomic bonds. There are several ways to minimize the energy increase. The four most important being adsorption, surface reconstruction, surface relaxation and surface segregation. Surface reconstruction is the reordering of atoms at the surface to decrease the number of broken bonds. In this case the surface structure is different from the truncated bulk structure. Another way to reduce the energy increase is surface relaxation. Surface relaxation is the tightening of atomic bonds between the surface atoms and their neighbours, which usually results in a contraction between the surface and sub-surface layer. Effectively this also causes a reduction of the number of broken bonds. In the case of pure relaxation the lateral surface structure is the same as the truncated bulk structure. Finally, the energy increase can be minimized by surface segregation. Segregation is the occupation of the surface atomic sites by species with the smallest bond energy, resulting in a surface composition that is different from the composition of the bulk material. Adsorption may be regarded as a special case of segregation ("segregation of environmental species to the surface of the material"). As a result of the above processes, which may all occur simultaneously, alloy surfaces often display a different composition and/or different structure than the bulk material.

The fact that surface properties play a prominent role in many applications, catalyst being an obvious example, is one of the drivers of surface science. Catalysts involve the adsorption and conversion of reactants at the surface and the subsequent release from the surface of the reagents. The adsorption and desorption depend, amongst others, on the surface energies of the reagents and reactant with respect to the surface energy of the catalyst. Conversion can only take place when the reactants can interact, which is closely related to the surface mobility of those atoms. The study of surface energies and surface mobilities in relation to the composition and structure of the used materials is one of the fields of surface science. This shows that surface science can have important contributions to the field of catalysis. However, also the growth of multi-layers, used for instance in mirrors and the read/write heads of hard drives, requires a detailed

knowledge of the processes at the surface to promote layer-by-layer growth instead of island growth. Summarizing: the study of surfaces is not only interesting from a fundamental point of view, but can also be used to aid the technological fields that depend on the surface properties of the used materials.

1.2 Step-edges

Step-edges separate terraces from each other at the surface. Therefore they can be regarded as "super-surfaces", being special with respect to the surface and the bulk just like the surface is special with respect to the bulk (see figure 1.1). Step-edges offer additional adsorption sites, have a different local structure and can cause enhanced segregation [1]. As a result the vicinal surfaces may show properties that are not shared by the defect free low index counterparts. An example is CO adsorption on stepped Pt(111) which shows a diffusion of the adsorbed CO from the terraces to the step-edges [2]. Also important for catalysis is the possible enhanced dissociation of adsorbed species, like in the case of NO on clean Rh(111) respectively Rh(311), which shows a increased activity of the latter [3]. However, also the opposite can be true like in the case of Pt(410) versus Pt(210), which shows a smaller reactivity of Pt(210) towards NO decomposition even though it's larger step-density [4]. Step-edges are not only interesting from a technological point of view, but can also be used to gain more knowledge about the fundamentals of segregation. Since bond breaking is generally regarded as the driving force of segregation [5], the step-edges should show enhanced segregation with respect to the surface. Low-Energy Ion Scattering (LEIS) [6] and Scanning Tunnelling Microscopy (STM) [7]
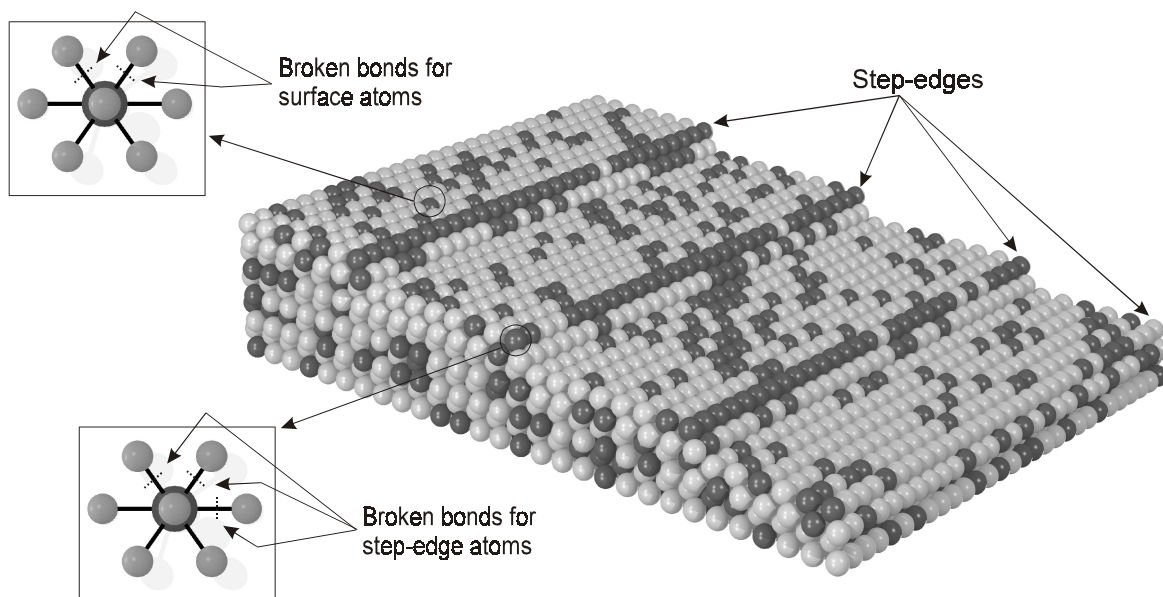
Figure 1.1: *Example of a stepped (vicinal) surface, showing the broken bonds of the surface atoms and the step-edge atoms.*

are two of the few measurement techniques that are capable to measure the local composition of step-edges [8, 9]. LEIS is the only one of these which can be applied over the wide temperature range which is required to study the temperature dependent segregation.

1.3 Scope and outline of this thesis

The goal of this thesis is to determine the morphology and/or composition of the surface region of single crystal model systems. The emphasis is put on establishing a relation between the temperature dependent step-edge and surface segregation of vicinal bimetallic alloys and to verify this relation using Low Energy Ion Scattering (LEIS). The measurement of the step-edge composition with LEIS requires a special scattering geometry that was not available at the start of my PhD period. Therefore a near 180 degrees back scattering Time Of Flight (TOF) has been added to the Energy and Angle Resolved Ion Scattering Spectrometer (EARISS). The properties of this backscattering TOF and the additional measuring tools mentioned in this thesis are described in chapter 2. Also the basic segregation equations are presented in chapter 2 and from them a functional form is derived that can be applied to vicinal surfaces.

In chapter 3 the bond length and the adsorption site are determined of potassium after room temperature deposition on Fe(110). The K/Fe system is extensively used in ammonia synthesis [10]. The conversion rate of the potassium promoted catalyst is increased with respect to the pure iron catalyst due to the enhanced sticking, increased maximum coverage and easier bond breaking of N_2 on the potassium covered surface [11, 12]. Potassium on iron acts as an 'electronic' promoter rather than a 'structural' promoter. However, the fact that potassium would not be expected to stick on iron at catalytic conditions initiated structural investigations of the K/Fe system [13]. Our measurements on K/Fe(110) have been performed using X-Ray Standing Waves (XSW) and Low Energy Electron Diffraction (LEED). Based on the XSW results a real-space model is proposed for K/Fe(110) that explains all the observed features in the XSW and the LEED measurements.

In chapter 4 and 5 the temperature dependent step-edge and surface composition of $Pt_{25}Rh_{75}(410)$ respectively $Pt_{50}Rh_{50}(511)$ are compared with the calculated step-edge and surface composition according to a simple broken bond model. PtRh is extensively used in the so called three-way-catalyst for the reduction of NOx and complete combustion of CO and hydrocarbons in automotive exhaust gasses [14]. Single crystal PtRh model catalysts with the same bulk Pt concentration but different surface orientations show large differences in selectivity and activity. To investigate whether the different catalytic properties are due to a different structure or due to a different surface composition we have also studied the step-edge and surface-composition of oxidized $Pt_{50}Rh_{50}(511)$. In contrast to the clean PtRh crystals, which show much stronger Pt segregation to the step-edges than to the terraces, the step-edge composition of oxidized $Pt_{50}Rh_{50}(511)$ is nearly the same as the terrace composition.

In chapter 6 the temperature dependent step-edge and surface composition of $Cu_3Au(17,1,1)$ are presented. Cu_3Au is widely used as a model system for ordering bimetallic alloys and as such the low index planes have been studied in great detail by various authors using different techniques. The temperature dependent surface composition of $Cu_3Au(100)$ suggests that the ordering inhibits the potentially stronger Au segregation to the surface. Here we investigate the Au segregation to the step-edges of a vicinal Cu_3Au crystal to determine if the lower coordinated sites enable stronger segregation or if that is prevented by the chemical ordering.

References:

1. K. Wandelt, Surf. Sci. 251 (1991) 387

2. J.E. Reutt-Robey, D.J. Doren, Y.J. Chabal, S.B. Christman, Phys. Rev. Letters 61 (1998) 2778

3. L. A. DeLouise, N. Winograd, Surf. Sci. 159 (1985) 199

4. J.M. Gohndrone, Y.O. Park, R.I. Masel, Journal of Catalysis 95 (1985) 244

5. F.L. Williams, D. Nason, Surf. Sci. 45 (1974) 377

6. H. Niehus, W. Heiland, E. Taglauer, Surf. Sci. Reports 17 (1993) 213

7. G. Minnig, H. Rohrer, Surf. Sci. 126 (1983) 236

8. P.T. Wouda, B.E. Nieuwenhuys, M. Schmid, P. Varga, Surf. Sci. 359 (1996) 17

9. B. Moest, P.T. Wouda, A.W. Denier van der Gon, M.C. Langelaar, H.H. Brongersma, B.E. Nieuwenhuys, D.O. Boerma, Surf. Sci. 473 (2001) 159 (chapter 4 of this thesis)

10. R.D. Diehl, R. McGrath, Surf. Sci. Reports 23 (1996) 43

11. L.J. Whitman, C.E. Bartosch, W. Ho, J. Chem. Phys. 85 (1986) 3688

12. D.R. Strongin, G.A. Somorjai, Catalysis Letters 1 (1988) 61

13. G. Ertl, S.B. Lee, M. Weiss, Surf. Sci 114 (1982) 527

14. B.E. Nieuwenhuys, J. Siera, K-I. Tanaka, H. Hirano, ACS. Symp. Series. 552; Environmental Catalysis, ACS, Washington DC, 1994

Segregation models and experimental approach

2

2.1 Segregation models

2.1.1 Introduction

Alloy surfaces can show a distinctive different composition and structure than the bulk due to the breaking of the lattice periodicity at the interface. Thermodynamic models that describe surface segregation minimize the Gibbs free energy [1] by optimizing the distribution of the different atoms over the provided lattice sites. The complexity of the model depends amongst others on the number of distinguishable lattice sites (phases) and the description of the interaction between the atoms. One of the simplest models in this respect is the ideal random alloy model by Mc Lean [2] which uses only two phases (surface and bulk) and the Langmuir adsorption isotherm to describe the interaction between the two phases. Below the surface composition X_s is presented as a function of bulk composition X_b and the temperature T according to the Langmuir-Mc Lean model:

$$\frac{X_s}{1-X_s}(T) \ = \ \frac{X_b}{1-X_b} \ e^{-\frac{\Delta E}{kT}} \quad , \tag{1}$$

with ΔE the heat of adsorption and k the Boltzmann constant. The heat of adsorption can be expressed as $\Delta E=\Delta\gamma*a$, with $\Delta\gamma$ the difference in surface energy and a the specific surface area of a surface atom. Equation (1) can not be applied to vicinal surfaces as it offers no discrimination between step-edges and terraces.

5

In the broken bond segregation model as presented by Williams and Nason [3], the surface energy is calculated based on the atomic bonds between nearest neighbours. It is shown that the segregation driving energy ΔE in equation (1) equals the number of broken bonds N of the surface atoms times the energy difference $\Delta \varepsilon$ per broken bond: $\Delta E = \Delta \varepsilon * N$. An approximation to $\Delta \varepsilon$ is based on the sublimation-enthalpy since that involves the breaking of all bonds N_{tot}:

$$\frac{X_s}{1-X_s}(T) \; = \; \frac{X_b}{1-X_b} \; e^{-\frac{\Delta \varepsilon \cdot N}{kT}} \; \approx \; \frac{X_b}{1-X_b} \; e^{-\frac{\Delta H_{sublimation}}{kT}\frac{N}{N_{tot}}} \qquad \textbf{(2)}$$

According to equation (2) the segregation towards the step-edges will be stronger than segregation towards the terrace due to the larger number of broken bonds (lower coordination). The above equations are applicable for ideal, or random mixing, alloys. For these alloys the segregation energy is independent of the chemical environment. Therefore only the lattice sites with missing neighbours, which are generally restricted to the first two atomic layers, will have a composition that is different from the bulk composition. To calculate the second and deeper layer compositions of quasi-random alloys like PtRh an energy term has to be introduced that corresponds to mixing of the species. Segregation equations for non-ideal alloys have been presented by e.g. Nelson et al. [3] and Ponec et al. [4]. However, due to various initial assumptions and simplifications (e.g. an equal number of atoms in all phases but the bulk), these formulas can not be applied to vicinal crystals. Below the segregation formula, as applied in the rest of this thesis, will be derived.

2.1.2 The segregation equation

The segregation equation will be derived for a binary alloy with a fixed lattice and a constant number of sites (*N*) which are either occupied by atom type *A* or *B*. The number of atoms of a given type, N_A and N_B, remains constant:

$$N \; = \; N_A + N_B \; = \; constant \quad , \quad N_A = constant \quad , \quad N_B = constant \qquad \textbf{(3)}$$

The atoms are distributed over the crystal, which is divided into several phases. A phase is defined as a set of similar lattice sites. The definition of similar, and the corresponding required number of phases, depends on the range of the interaction between the atoms and the mixing behaviour. In the case of a (001) surface of an ideal fcc alloy and assuming nearest neighbour interaction there are only two distinct different sites: the surface and the bulk. However, to describe a slightly ordering vicinal alloy there are at least 4 phases required: the step-edges, the terraces, the second layer and the bulk. Here the second layer is included because ordering crystals show an alternating segregation profile.

The number of atomic sites N_φ within a phase φ is constant, but is not necessarily equal for the different phases. A configuration is defined as an unique distribution of A and B atoms over the phases, without discrimination of the different distributions of those atoms within the

phase (exchanging atoms within a phase thus does not change the configuration). By the above definition the enthalpy corresponding to a given configuration can be calculated from the composition of the phases and the interaction between the phases only. The equilibrium (average/most likely) composition of the system can be calculated by determining the configuration with the minimum Gibbs free energy G [5].

The Gibbs free energy G_i corresponding to configuration i equals (see e.g. [6]):

$$G_i = -kT \ln(p_i) \quad , \quad p_i = \frac{g_i \cdot e^{-\frac{E_i}{kT}}}{Q} \quad , \quad Q = \sum_j g_j \cdot e^{-\frac{E_j}{kT}} \quad , \tag{4}$$

here p_i is the chance on the observation of configuration i with energy E_i, which has a degeneracy g_i and Q is used for normalisation. Only bond energy related energy terms will be considered in the calculation of the change in E_i due to a change in composition. Different effects that may also occur, like frequency shifts in the vibrations of surface atoms, are thus not included. The degeneracy results from the fact that different distributions of A and B atoms within a phase does (by definition) not change that configuration. This is illustrated in figure 2.1 which shows an imaginary 2D crystal consisting of six atoms. Two phases are defined in this system. The
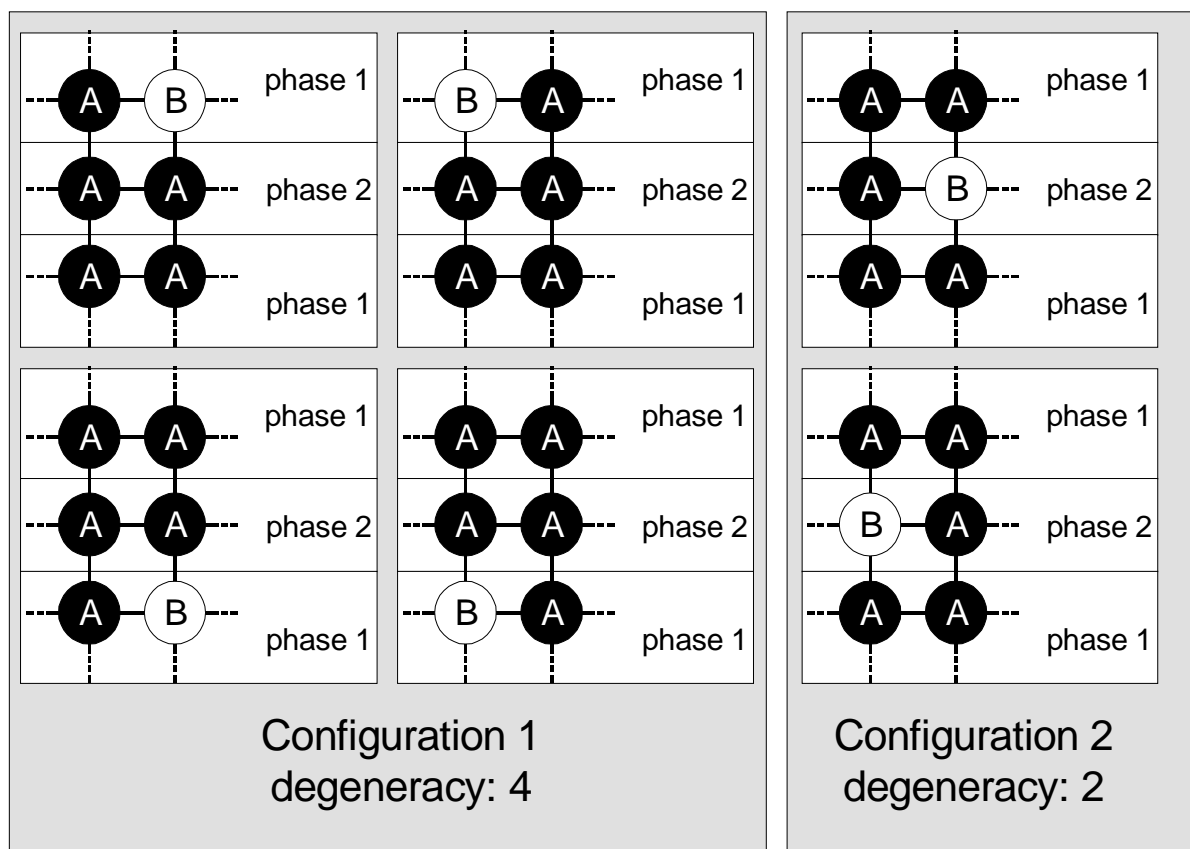
Figure 2.1: *Example of the possible configurations for an imaginary 2D crystal with six atoms. Two phases have been defined within this model system of three atoms each.*

assigned phase depends on the number of missing neighbours, the four sites with two missing neighbours are assigned to phase 1 and the two sites with one missing neighbour are assigned to phase 2. The single B type atom can either be assigned to phase 1 or phase 2. There are four possible distributions of the A and B type atoms when the B atom is assigned to phase 1, when the B atom is assigned to phase 2 there are two possible distributions. Therefore the degeneracy of configuration 1 is $g_1 = 4$ and the degeneration of configuration 2 equals $g_2 = 2$.

Due to the limited number of atoms, the total bond energy of the imaginary model in figure 2.1 can be easily evaluated for all (six) possible distributions of the atoms over the available lattice sites. However, for the upcoming models this will not be possible due to the large number of atoms. According to the earlier definition of a phase, we can calculate the total bond energy of a configuration by the evaluation of the bonds between the phases only. The original problem of calculating the total bond energy for all possible distributions thereby reduces to the calculation of the total bond energies for all possible configurations and the determination of the degeneracy corresponding to each configuration.

The degeneracy g of each configuration equals the product of the degeneracies of all phases φ. The total bond energy E of the configuration equals the sum of the bond energies of all phases:

$$g = \prod_\varphi g_\varphi \quad , \quad E = \sum_\varphi E_\varphi \quad \Rightarrow \quad G = kT \ln(Q) + \sum_\varphi \left\{ E_\varphi - kT \ln(g_\varphi) \right\} \tag{5}$$

First the total bond energy of a given configuration will be determined. The following definitions will be used:

$N_{i,A(B)}$: The number of A(B) atoms in phase i
$n_{AA(AB, BB)}$: The number of AA (AB, BB) bonds
Z_{ij} : The number of bonds per atom of phase i to atoms of phase j
X_i : The concentration of A atoms in phase i
ε_{AB} : The energy corresponding to a single bond between an A and a B atom
E_0 : Non bond-energy related energy contributions (constant)

Following the method of Williams and Nason [7] the total bond energy is calculated by counting all A-A, B-A and B-B bonds. However, we will not make a choice for a particular bond model or crystal type yet. Furthermore it is not assumed that all phases (but the bulk) have an equal number of atoms, which is particularly important in the case of vicinal crystals. Using the above definitions the total bond energy can be calculated:

$$\sum_\varphi E_\varphi = E_0 + n_{AA}*\varepsilon_{AA} + n_{AB}*\varepsilon_{AB} + n_{BB}*\varepsilon_{BB} =$$

$$E_0 + \frac{1}{2}\sum_i^\varphi \sum_j^\varphi N_i Z_{ij} \left\{ X_i X_j \varepsilon_{AA} + [X_i(1-X_j)+X_j(1-X_i)]\varepsilon_{AB} + (1-X_i)(1-X_j)\varepsilon_{BB} \right\} \tag{6}$$

The summation over i and j is performed over all phases φ. The factor ½ prevents double counting of the bonds. By introducing the bond-energy difference $\Delta\varepsilon = \varepsilon_{BB} - \varepsilon_{AA}$ and the regular solution parameter $\Omega = \varepsilon_{AB} - (\varepsilon_{AA} + \varepsilon_{BB})/2$ equation (6) can be rewritten:

$$\sum_\varphi E_\varphi = E_1 + \frac{1}{2}\sum_i^\varphi \sum_j^\varphi N_i Z_{ij} \left\{ \frac{1}{2}\Delta\varepsilon [2-X_i-X_j] + \Omega [X_i+X_j-2X_iX_j] \right\}$$

$$E_1 = E_0 + \frac{\varepsilon_{AA}}{2}\sum_i^\varphi \sum_j^\varphi N_i Z_{ij} \quad , \tag{7}$$

here E_1 is the sum of the non-bonding related energy contributions (E_0) and the constant bond energy contributions of equation (6). The assumption that the enthalpy of a phase is independent of the distribution of atoms over that phase corresponds to the assumption that the atoms within a phase are indistinguishable. This allows to calculate the degeneracy of a phase i:

$$g_i = \frac{(N_{i,A}+N_{i,B})!}{N_{i,A}! \ N_{i,B}!} \tag{8}$$

So the logarithm of the degeneracy, required to evaluate equation (4) respectively equation (5), equals (using the Stirling approximation):

$$\sum_i^\varphi \ln(g_i) = \sum_i^\varphi \ln\left(\frac{(N_{i,A}+N_{i,B})!}{N_{i,A}! \ N_{i,B}!} \right) \cong -\sum_i^\varphi \left\{ N_{i,A}\ln(X_A) + N_{i,B}\ln(X_B) \right\} =$$

$$= -\sum_i^\varphi N_i \left\{ (X_i)\ln(X_i)+(1-X_i)\ln(1-X_i) \right\} \tag{9}$$

For the configuration with the minimum Gibbs free energy, the energy change due to a change in the composition X_k of any phase k will be zero:

$$\forall_k \quad \frac{dG}{dX_k} = 0 \tag{10}$$

Taking the partial differential of G with respect to X_k yields, using (5), (7) and (9):

$$\frac{\partial G}{\partial X_k} = \sum_i^\varphi N_k Z_{ki} \left\{ \Omega[1-2X_i]-\frac{1}{2}\Delta\varepsilon \right\} + kT \ N_k \ \ln\frac{X_k}{1-X_k} \tag{11}$$

Any change in the concentration of phase k will cause a change in the concentration of the other phases due to the exchange of atoms. Since each phase is in equilibrium with all other phases we may assume without loss of generality that the atoms of phase k are exchanged with phase l only:

$$\frac{\partial X_l}{\partial X_k} = -\frac{N_k}{N_l} \tag{12}$$

Combining equation (10), (11) and (12) yields:

$$\frac{dG}{dX_k} = \frac{\partial G}{\partial X_k} + \frac{\partial X_l}{\partial X_k}\frac{\partial G}{\partial X_l} = \frac{\partial G}{\partial X_k} - \frac{N_k}{N_l}\frac{\partial G}{\partial X_l} = 0 \quad \Rightarrow$$

$$kT\left\{\ln[\frac{X_k}{1-X_k}]-\ln[\frac{X_l}{1-X_l}]\right\} = \sum_i^\varphi \left\{\frac{1}{2}\Delta\varepsilon[Z_{li}-Z_{ki}]-\Omega[1-2X_i][Z_{li}-Z_{ki}]\right\} \tag{13}$$

Which can be rewritten to:

$$\forall_{k,l} \quad \frac{X_k}{1-X_k} = \frac{X_l}{1-X_l}\,e^{-\frac{\Delta H}{kT}} \quad , \quad \Delta H = \sum_i^\varphi \left\{\Omega[1-2X_i][Z_{li}-Z_{ki}] - \frac{1}{2}\Delta\varepsilon\,[Z_{li}-Z_{ki}]\right\} \tag{14}$$

In equation (14) there has been made no assumption on the bonding model and it does not require that all phases have an equal number of sites. As such it bridges the gap between simple analytical expressions like equation (2) that can only be applied to fairly simple crystals and the more complex models like the Corrected Effective Medium (CEM) [8] and Surface Modified Pair Potential (SMMP) models [9, 10] that require a lot of computing time. In this respect equation (14) is a useful extension to the existing segregation formula in literature. Equation (14) will transform in equation (2) by the proper choice of the bond model and bond energies (only bonds between nearest neighbours and a regular solution parameter of zero). When the crystal is in full equilibrium it is advantageous to choose phase l as the bulk. The "infinite" reservoir of atoms will simplify the equation for ΔG, as the bonds per atom to all phases other than the bulk equal zero and the composition of the bulk does not change. In the case of partial equilibrium, for instance between the first and second atomic layer, the composition of these layers may be approximated by only evaluating equation (14) for the layers that are in equilibrium.

For most bond models there will be no analytic solution available for equation (14) so the composition of the phases will have to be calculated by successive approximation. A good starting configuration is obtained by setting the composition of all phases equal to the bulk composition, which corresponds to starting at "infinite" temperature. In any algorithm that calculates the final configuration, the combination of phases k and l that yield the largest change

Figure 2.2: a) *Schematic representation of the local environment of a single atom (large dark sphere) in a fcc lattice and it's nearest neighbours (smaller light spheres). The left figure shows the projection of the nearest neighbour positions on the <110> cross-section of the fcc lattice. In the right figure the projection on the <100> cross-section is shown. The number of projected nearest neighbours of the centre atom are indicated by the values in the squares. b) The method of bond counting between the phases, as applied to the $Pt_{25}Rh_{75}(410)$ crystal. In the middle figure the phases are assigned to the sites of the crystal. The thick lines show the borders between the repeating unit cells. One unit cell has the assigned phases indicated in light gray to allow easy comparison with the schematic PtRh(410) crystal, shown in the figure above. The bottom figure shows the actual nearest neighbour counting for the atom below the step-edge (assigned to phase 1). The figure shows the number of bonds (first number) and the corresponding phase (second number).*

in Gibbs free energy according to equation (13) should be selected as the first phases that are updated in the successive approximation (steepest descent). For faster convergence switching between steepest descent (always converging, but possibly slow) and Gauss-Newton (fast, but not guaranteed to converge) may be applied similar to the Levenberg-Marquardt minimization algorithm [11]. The number of bonds per atom between the phases has to be known to apply equation (14). For complicated crystals or bond models these have to be calculated by computer. In figure 2.2 an example is shown how to calculate Z_{ij} for the $Pt_{25}Rh_{75}(410)$ crystal, assuming only bonds between nearest neighbours. First a simple 2D representation of the 3D fcc structure is introduced in figure 2.2a.

An arbitrary fcc atom is shown (large dark sphere) with the 12 nearest neighbours (small grey spheres). The central atom has been assigned a different size and gray-value for easy discrimination between this atom and it's neighbours. In the 2D representation the nearest neighbour atoms in parallel planes are projected to the plane of the central atom. The number in the squares represents the number of projected nearest neighbours. The squares that represent two nearest neighbours are assigned to the same phase as the local geometry and environment for the corresponding atoms are identical. It must be noted that this choice excludes strong chemical ordering of the crystal. Using the above described method it is possible to build a 2D representation of any (n11) or (n10) crystal, assign the phases and count the number of bonds between the interacting phases. This is illustrated in figure 2.2b. To describe $Pt_{25}Rh_{75}(410)$, the cross-section of the fcc lattice in the <100> direction has to be used. An arbitrary number of phases can be defined, depending on the properties of the alloy. From measurements it is known that PtRh has an alternating composition profile, which corresponds to a negative regular solution parameter. Therefore at least the step-edge, surface, second layer and bulk should be allowed to vary in composition (at least four phases). In figure 2.2b the actual layout is shown as used in chapter 4, consisting of nine phases. The assigned phases are denoted in the squares. The number of bonds between the phases can be simply determined by counting the bonds to the surrounding phases for all atoms within one repeating slab (indicated by the thick vertical lines). The inset shows an example of the bond counting for phase 1, using the number of bonds to the surrounding sites (as shown in the right of figure 2.2a) and the defined phases (as shown in the middle of figure 2.2b). There is only one atom assigned to phase 1 for each repeating slab, Z_{1j} therefore equals:

$$Z_{1j} = [\ 1 \ 0 \ 1 \ 4 \ 1 \ 0 \ 0 \ 0 \ 0 \ ] \tag{15}$$

The coordination of the atoms in phase 1 is thus 7, which corresponds to five missing nearest neighbours. Assuming an ideal solution ($\Omega=0$) and equilibrium with the bulk, the segregation enthalpy in equation (14) would thus become $\Delta G=2.5*\Delta\varepsilon$ for phase 1. In table 2.1 the bond matrix is shown for phase 0 (step-edge) to phase 8 (bulk) with all other phases ($N_i Z_{ij}$). To calculate Z_{ij} this number should be divided by the number of atoms in a certain phase (N_i), which is also presented in the table. The table is symmetrical as the number of bonds from phase i to phase j equals the number of bonds from phase j to phase i ($N_i Z_{ij} = N_j Z_{ji}$).

Table 2.1: *Bond matrix of the $Pt_{25}Rh_{75}(410)$ crystal, as shown in figure 2.2b, showing the number of bonds between the phases (N_iZ_{ij}). The number of atoms per phase in the repeating slab is also indicated in the table. Phase 0 corresponds to the step-edges, whereas phase 2 corresponds to the terrace atoms. The surface is the combination of the phases 0, 1 and 2 (the atoms in phase 1 are partly shielded by the step-edge atoms).*

phase										# atoms
i \ j	0	1	2	3	4	5	6	7	8 (bulk)	Ni
0	0	1	2	2	1	0	0	0	0	1
1	1	0	1	4	0	1	0	0	0	1
2	2	1	20	3	22	1	0	0	0	6
3	2	4	3	2	3	7	1	0	0	2
4	1	0	22	3	20	25	1	0	0	6
5	0	1	1	7	25	28	32	2	0	8
6	0	0	0	1	1	32	28	32	2	8
7	0	0	0	0	0	2	32	28	34	8
8 (bulk)	0	0	0	0	0	0	2	34	12N-36	N

In the derivation of equation (14) it was assumed that exchanging atoms within a phase does not change the energy of the configuration. However, for any non-ideal alloy ($\Omega \neq 0$) this will not be true. This is easily demonstrated by considering the exchange of atoms within the bulk of an ordering alloy. In the case of an ordering alloy the AB bonds are energetically favoured over AA and BB bonds (negative regular solution parameter). This means that the total energy corresponding to a random distribution will be larger than the total energy corresponding to an ordered distribution. However the definition of a single bulk phase allows no control on the distribution of the atoms over that phase. Equation (14) should therefore only be used for alloys with small regular solution parameters (contribution to the segregation enthalpy up to about 10%), which are referred to as (quasi) random alloys. For larger regular solution parameters different methods may be applied like e.g. the separation of the bulk in two or more phases to enable phase separation or ordering. However, a better approach for these kind of alloys is calculating the composition using Monte Carlo simulations.

2.1.3 Composition determination by Monte Carlo simulations

Segregation simulations are a good alternative for the above discussed analytical expressions to determine the composition of alloys with a tendency to either order or to cluster. A segregation simulation starts by defining a crystal model and the criteria whether atoms can exchange their positions in the lattice, based on the energy difference before and after the possible exchange. In this chapter we will discuss the Monte Carlo (MC) type of simulations as used to calculate the temperature dependent composition of $Cu_3Au(17,1,1)$ presented in chapter 5. The chosen lattice is rigid and defect free. Furthermore, it is assumed periodic in two dimensions (x and y) and finite in the third dimension (z). Stepped surfaces need special attention to guarantee good boundary conditions (see e.g. figure 2.15, where similar boundary conditions are required for ion trajectory simulations). The surface composition at a certain temperature is calculated by

averaging over a large number (typical 5000) of configurations. Each configuration is generated by performing atom exchange attempts until the number of accepted exchanges or the number of attempts exceed predefined limits that are based on the total number of lattice sites in the crystal model. The simulation method will be discussed in more detail below.

Each exchange attempt consist of several steps. Two sites, k and l, containing different atom species are selected at random from the lattice. Exchanging the atoms of these two sites would transform configuration a into configuration b. The chance P_a respectively P_b on either configuration cannot be calculated separately since the normalization constant Q of equation (4) cannot be determined for reasonable simulation slabs. However, it is possible to calculate the ratio between P_a and P_b using the energy difference $\Delta E_{ba}=E_b-E_a$ between the configurations:

$$P_{ba} = \frac{P_b}{P_a} = \frac{e^{-\frac{E_b}{kT}}}{Q} / \frac{e^{-\frac{E_a}{kT}}}{Q} = e^{-\frac{\Delta E_{ba}}{kT}} \tag{16}$$

According to the general MC simulation method, an exchange attempt is accepted if it will result in an energy decrease ($\Delta E_{ba}<0$). In the case of an energy increase, the atoms are only exchanged if a generated random number between zero and one is smaller than the relative chance on configuration b with respect to configuration a, P_{ba}:

$$\begin{aligned}
&\Delta E_{ba}<0 \quad \Rightarrow \text{ configuration } b \\
&\Delta E_{ba}\geq 0 \quad \Rightarrow \begin{cases} R = rand\ [0,1] \\ R < P_{ba} \quad \Rightarrow \quad \text{configuration } b \\ R \geq P_{ba} \quad \Rightarrow \quad \text{configuration } a \end{cases}
\end{aligned} \tag{17}$$

The total energy corresponding to a configuration n can be calculated using a discrete version of equations (6) and (7). The phase approach will change into the MC approach by choosing the number of phases equal to the number of atoms in the lattice (N) and allowing only discrete values of the concentration. To emphasize that a site is either occupied by atom type A or B, the concentration X_i is replaced by P_i, where $P_i=1$ corresponds to an A type atom at site i and $P_i=0$ to a B type atom. According to the above, the discrete version of equation (7) becomes:

$$\forall_{i \in N} \quad \{ \quad N_i=1 \quad , \quad P_i = \{0,1\} \quad , \quad Z_{ii} = 0 \quad \}$$
$$E_n = E_1 + \frac{1}{2}\sum_i^N \sum_j^N Z_{ij}\left\{\frac{1}{2}\Delta\varepsilon\ [2-P_i-P_j] + \Omega\ [P_i+P_j-2P_iP_j]\right\} \tag{18}$$

As the possible exchange only involves sites k and l it is sufficient to calculate the contribution of these sites to the energy of the configuration:

$$E_n \equiv E_1 + \frac{1}{2}\sum_{i \neq k,l}^{N}\sum_{j \neq k,l}^{N} Z_{ij}\left\{\frac{1}{2}\Delta\varepsilon \; [2 - P_i - P_j] \; + \; \Omega \; [P_i + P_j - 2P_iP_j]\right\} \; + \; E_{n,k} \; + \; E_{n,l}$$

$$E_{n,k} = \sum_{i}^{N} Z_{ij}\left\{\frac{1}{2}\Delta\varepsilon \; [1 - P_k - P_i] \; - \; \Omega \; [P_k + P_i - 2P_kP_i]\right\}$$

(19)

The original configuration has different atom types at the sites k and l ($P_k = 1-P_l$), the energy difference between configuration a and b is therefore:

$$\Delta E_{ba} = \Delta P \sum_{i}^{N}\left\{\Omega[1 - 2P_i][Z_{li} - Z_{ki}] \; - \; \frac{1}{2}\Delta\varepsilon \; [Z_{li} - Z_{ki}]\right\}$$

$$\Delta P = 2P_{k,a} - 1 \quad ,$$

(20)

with $P_{k,a}$ the occupation of lattice site k in configuration a ($P_{k,a}=1$ if lattice site k contains an A type atom in configuration a). Note the similarity between equation (20) and equation (14).

The composition of the crystal is averaged over a large number of generated configurations, using a moving averaging method with selectable averaging length. The advantage of the moving average filter is that the initially calculated surface concentrations will eventually drop out of the averaging scope when they are different from the final calculated surface concentrations. Depending on the length of the moving averaging filter, the simulations can be optimized for speed or accuracy in the final result. The simulation time scales linear with the filter length and the accuracy scales with the reciprocal square root of the filter length. Below an example is shown of a composition simulation for $Cu_3Au(100)$. The simulation slab size has been chosen 32x16x60, corresponding to a total of 32640 atoms of which 8160 Au and 24480 Cu. The surface concentration is calculated over the 2040 sites that are exposed directly to the ion beam. Each configuration has been generated by performing 32640 exchange attempts. For illustration purposes no moving averaging is performed. The next nearest neighbour bond strength is assumed 10% of the nearest neighbour bond strength. The bond energy difference has been chosen $\Delta\varepsilon = 10 \, kJ/mol$ and the regular solution parameter has been chosen $\Omega = -3.9 \, kJ/mol$. At the start of the simulation the Cu and Au atoms are randomly distributed over the lattice sites. The surface concentration and the acceptance rate are calculated after each newly generated configuration for $T = 0 \, K$, $T = 500 \, K$ and $T = 10^6 \, K$. By choosing these extreme temperatures (ignoring the fact that they may not be reached or that the crystal ceases to exist) the properties of the MC simulation are demonstrated easier.

In figure 2.3a the fraction of accepted exchanges is shown versus the total number of exchange attempts. All exchange attempts are accepted at $T = 10^6 \, K$, which is in accordance with equation (17). For $T = 0 \, K$ the exchange attempts are accepted as long as it results in an energy decrease. At the start of the simulation all atoms are located at random positions. Exchanging atoms will therefore likely result in an energy decrease, which corresponds to the large
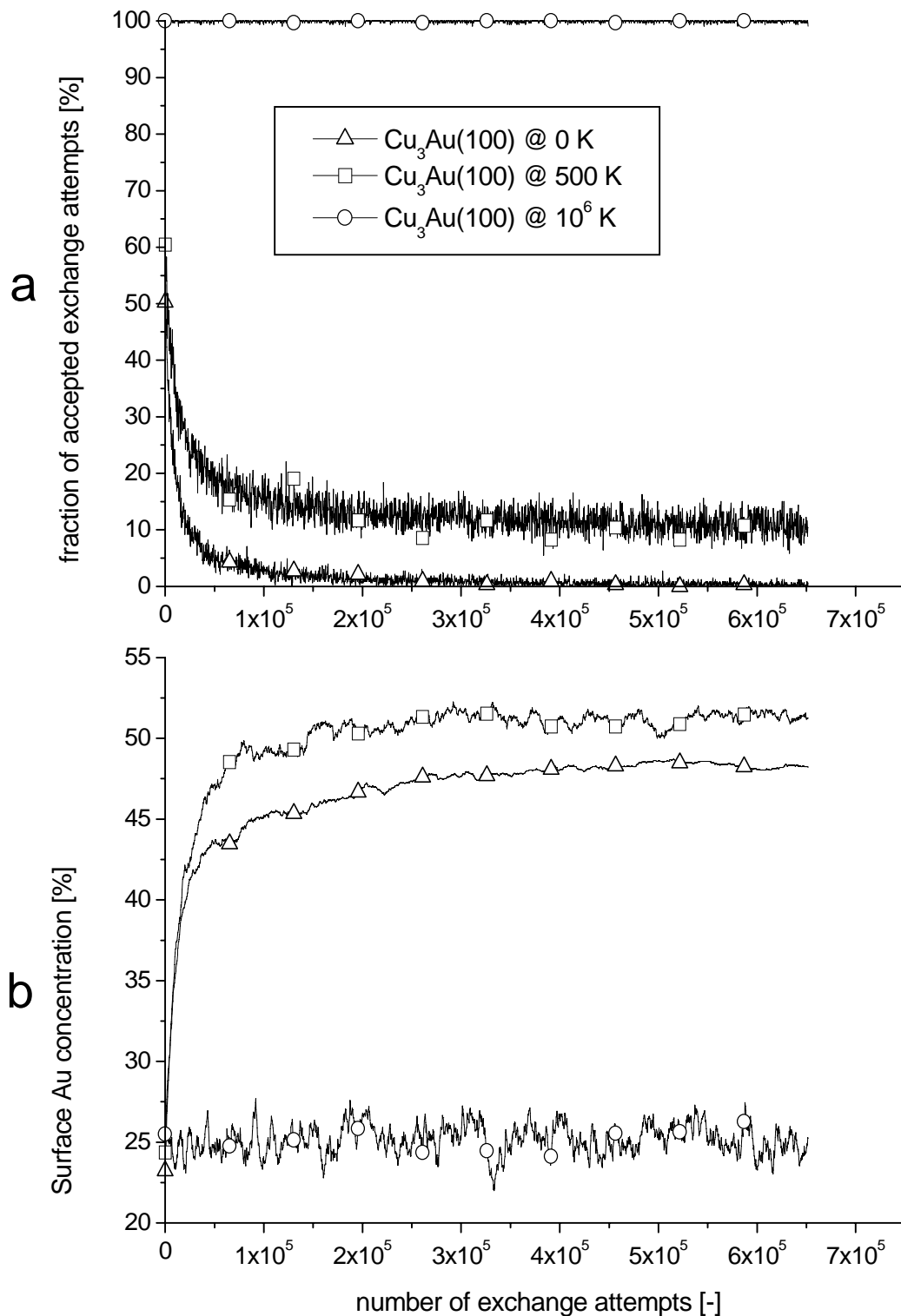
Figure 2.3: *The transient behaviour of the MC simulation to determine the composition of $Cu_3Au(100)$. a) The fraction of accepted exchanges versus the total number of exchange attempts. b) The surface composition versus the total number of exchange attempts*

acceptance rate. Less atoms can be exchanged when the slab is getting ordered, until ultimately the acceptance ratio will become zero. The simulation at T = 500 K shows the intermediate behaviour. The crystal starts to order during the first part of the simulation. However, full ordering will never be achieved since the temperature is still large enough to exchange atoms even if that results in an energy increase. The consequences of this behaviour on the calculated surface concentrations are shown in figure 2.3b. At T = 10^6 K the surface concentration corresponds to the bulk concentration of 25 % Au. The surface concentration at T = 0 K increases faster at the start of the simulation than the surface concentration at T = 500 K. The simulation slab will contain several locally ordered domains. However, these domains cannot combine into a single domain since that would require temporarily configurations with a larger total energy. The final calculated surface concentration is therefore below the 50% Au that is expected for a perfect ordered crystal. This behaviour is comparable to quenching of the real crystal after heating it above the ordering temperature, which will also result in a surface concentration that is somewhere between the surface concentration of the random surface and the ordered surface.

Two additional MC simulations have been performed to further demonstrate this behaviour. In the first simulation the composition has been determined at T = 0 K after starting with a random alloy, without evaluating the configurations at intermediate temperatures. The configuration at the surface is presented in figure 2.4a, which clearly shows the domains (enclosed by the hatched areas) that result from the quenching behaviour as discussed above. In the final configuration there exists several domains (e.g. the encircled domain in the top-right area) that would cause an energy decrease by translation. In the second simulation the configurations have also been evaluated at intermediate temperatures between the starting temperature of 1000 K and the final temperature of 0 K. Above 0 K there is a certain chance that atoms exchange, even if that causes an energy increase. However, since the trend will still be an energy decrease the domains will combine into larger domains until finally a perfectly ordered crystal is obtained. The surface composition after slow cooling is shown in figure 2.4b.
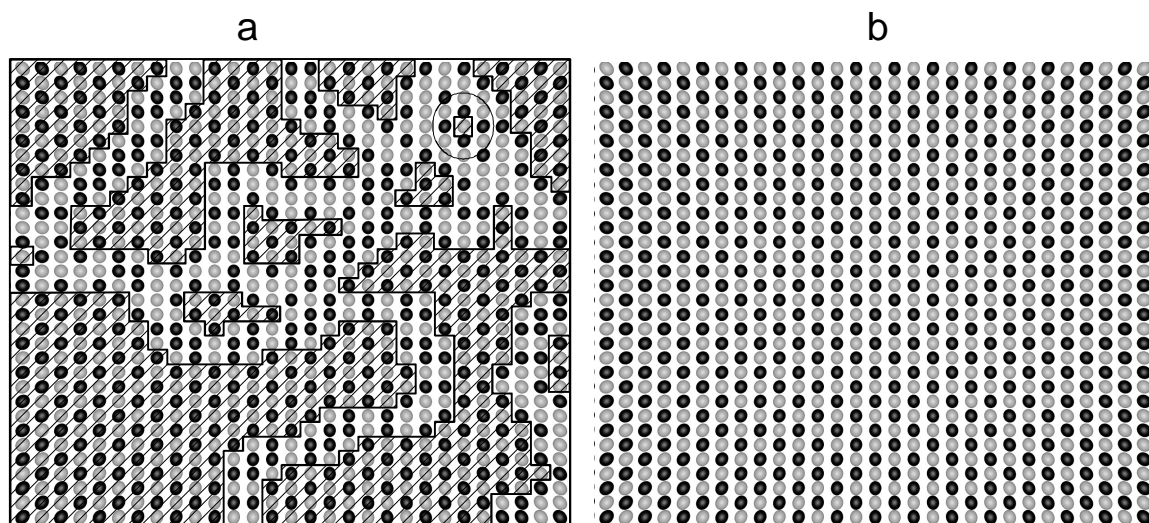
Figure 2.4: *a) Surface composition at the end of the MC simulation for T = 0 K in the case of a)"quenching" and b)"slow cooling" (see text above).*

The above discussed MC simulation will be used to calculate the temperature dependent surface and step-edge composition of $Cu_3Au(17,1,1)$. The bond energy and the regular solution parameter will be used as free parameters to fit the simulated surface concentration to the measured surface concentration. To avoid the above discussed quenching-like behaviour, the composition of the crystal is also computed at intermediate temperatures if the difference in temperature between two points is larger than 25 °C.

2.2 Low Energy Ion Scattering (LEIS)

All chapters about segregation in this thesis include Low Energy Ion Scattering (LEIS) measurements. Below a general introduction will be presented, see the review article of Niehus et al. [12] for more detailed information about LEIS. The LEIS technique is based on the detection of atoms and/or ions after the collision of projectiles with atoms in the studied sample (see figure 2.5). The detected particles may either be scattered projectiles or recoils. Recoils are the atoms at the surface that are knocked out due to the collision with the projectile (two body process, see atom 2 in figure 2.5). Structural information can be extracted from the angular dependence of the scattered yield. The mass of the atoms in the probed area with respect to the mass of the projectile atoms ($A=m_2/m_1$) can be calculated from the kinetic energy of the detected particles according to equation (21).
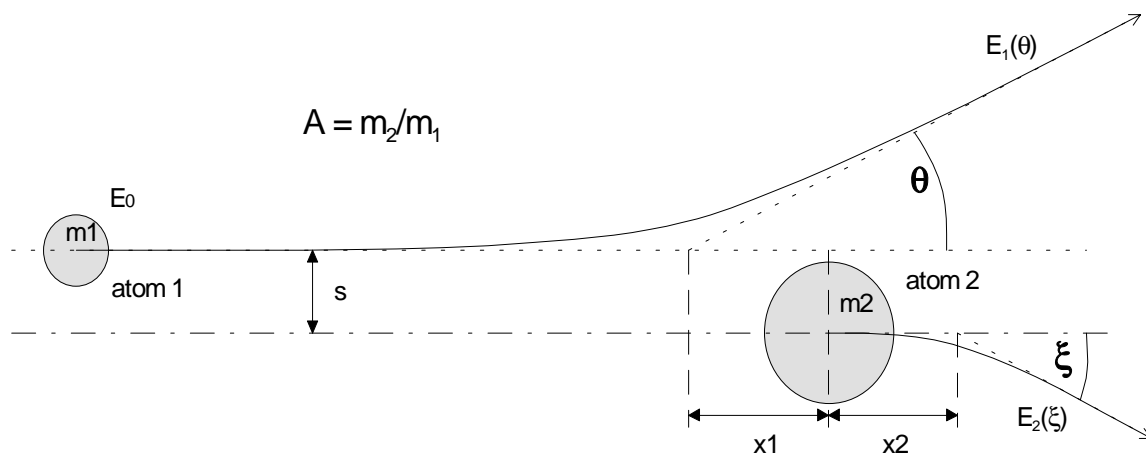
Figure 2.5: *Schematic representation of the projectile (atom 1) and the target atom (atom 2) trajectories (solid lines) for a given impact parameter s. The dotted lines represent the trajectory asymptotes.*

$$\text{scattered particles} \quad : \quad \frac{E_1(\theta)}{E_0} = \left[\frac{\cos\theta \pm \sqrt{(A^2 - \sin^2\theta)}}{1 + A}\right]^2 \quad : \sin(\theta) \le A < 1$$

$$\frac{E_1(\theta)}{E_0} = \left[\frac{\cos\theta + \sqrt{(A^2 - \sin^2\theta)}}{1 + A}\right]^2 \quad : A \ge 1 \qquad (21)$$

$$\text{recoiled particles} \quad : \quad \frac{E_2(\xi)}{E_0} = \left[\frac{2\cos\xi}{1 + A}\right]^2$$

Backscattering LEIS experiments require that the mass of the projectile is smaller than the mass of the target atom (A>1). At these conditions, the best mass resolution ($\Delta E_1/\Delta m_2$) for scattered particles will be achieved at larger scattering angles and projectiles that have almost the same atomic mass as the surface atoms. The best mass resolution for recoiled particles ($\Delta E_2/\Delta m_2$) is achieved for small scattering angles and larger projectile over target atom mass ratios. Recoiling spectroscopy is therefore usually performed in a forward scattering geometry and with relative heavy projectile atoms (Ar^+ & Xe^+) compared to LEIS in the backscattering geometry (He^+ & Ne^+). The energy spectra can be regarded as mass spectra. The area of the peaks is proportional to the surface density of the corresponding elements. The sensitivity towards certain elements can be calibrated using reference samples. There are several implementations of LEIS that are optimized for e.g. yield, structural information or surface sensitivity. Below the implementations that have been used throughout this thesis are discussed.

2.2.1 Techniques: Electro-Static Analyser-Low Energy Ion Scattering (ESA-LEIS)

Charged particles can be energy selected using an electrostatic analyser. ESA-LEIS becomes very surface sensitive when noble gas ions are used. The large neutralization probability of more than 80% per scattering event ensures that the contribution of the first atomic layer to the scattered ion yield will be much larger than the deeper layer contribution. For relatively open structures like the Pd(110) surface, the second layer contribution is only 10% [13] when using 3 keV Ne^+. For closed surfaces like Rh(100), the second layer contribution is even smaller (4%, see chapter 4 of this thesis). See [14] for the crystal orientation dependency of the scattered ion yield. The yield of ESA-LEIS experiments in combination with noble gas ions results in a yield that is mainly caused by single scattering events. The scattered yield can therefore be calculated without detailed knowledge of the trajectories or the scattering geometry:

$$Y_i(E) \approx I*t * n_i * \frac{d\sigma}{d\Omega} * \alpha * \varepsilon * P^+ = S_i * I*t * n_i \quad , \qquad (22)$$

with

Y_i :   Detected yield due to element i

$I*t$:   Applied ion dose

n_i :   Surface density of element i

dσ/dΩ :   Differential scattering cross-section

α :   Steric (roughness) factor describing visibility of the atoms due to e.g. blocking
            (see next section)

ε :   Detector efficiency

P^+ :   Ion survival probability

S_i :   Overall sensitivity towards element i, which can be calibrated by measuring a
            reference sample with known surface density at identical conditions

Deeper atomic layers of a sample can be probed by using projectiles with a small neutralization probability, like alkali ions. However, equation (22) will in general not be valid in this case.

2.2.2 Techniques: Time Of Flight-Scattering And Recoiling Spectroscopy (TOF-SARS)

The Time-Of-Flight (TOF) technique features a pulsed ion beam, which allows the flight time measurement of recoils and projectiles. The kinetic energy of the scattered particles can be calculated using the relation between the measured flight time and the known scattering geometry in combination with the selected primary energy and mass of the primary ion. Neutral particles can also be detected since the TOF technique does not require electrostatic analysers. TOF is therefore suited to perform composition measurements of deeper layers and for scattering geometries that require a long interaction between the projectiles and the sample (e.g. surface roughness measurements using mirror reflection mode at glancing angles of incidence [15]). TOF has to be used in a forward scattering geometry to detect recoils. This geometry will be referred to as Time-Of-Flight, Scattering And Recoiling Spectrometry (TOF-SARS). One of the advantages of recoiling spectroscopy is that all elements can be detected, including hydrogen, which is not true for backscattering LEIS. The scattered yield of TOF-SARS measurements
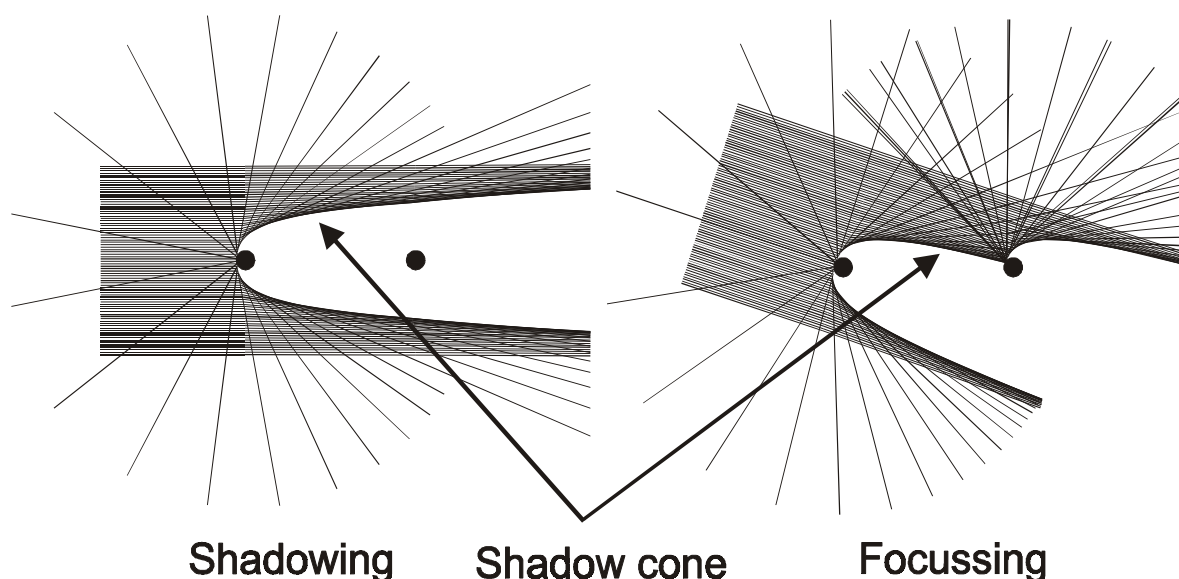

Shadowing   Shadow cone   Focussing

Figure 2.6: *Schematic picture of shadowing and focussing. When atoms are placed in the shadow cone of other atoms it is called shadowing. When the edge of the shadow cone, with increased ion density, is aimed at another atom it is called focussing.*

highly depends on the chosen scattering geometry. Two important scattering conditions, shadowing and focussing, are illustrated in figure 2.6. Shadowing is the obstruction of the ion-beam by atoms that thereby prevent the detection of the shadowed atom(s). This scattering condition will be applied throughout this thesis in the step-edge composition measurements of vicinal crystals, where the terrace-atoms are placed in the shadow cone of the step-edge atom. When projectiles can hit an atom, but cannot return to the detector due to atoms in between, this is referred to as blocking. The second important scattering condition is focussing, which occurs when the envelope of the shadow cone coincides with another atom. In this case the yield due to the latter atom can show a significant increase.

In TOF-SARS the same atomic site can be probed by alternative trajectories. Therefore, unlike ESA-LEIS, the scattering differential cross-section cannot be taken constant but has to be calculated according to the corresponding collision. The relative contributions of atomic sites to the scattered yield in a given geometry are calculated by ion trajectory simulations.

2.2.3 Techniques: Co-Axial Impact Collision Ion Scattering Spectrometry (CAICISS)

The CAICISS technique uses a detector that is mounted in a (near) 180 degrees back-scattering geometry with respect to the ion beam. This can be achieved by deflecting the ions on their way from the source to the sample or by using a detector with a central hole. The advantage of CAICISS is that the ions can travel the same way to and from the sample, thus enabling easier interpretation of the spectra. Initially the CAICISS technique was intended to determine the composition of deeper layers [16]. However, as will be shown in chapters 4 to 6 of this thesis, it can also be used to determine the step-edge composition by using a suitable scattering geometry (small angles of incidence). Due to the long interaction between the projectiles and the surface, this scattering geometry will result in a large neutralization probability. Therefore a TOF type detector has been used.

2.2.4 LEIS setup: Energy and Angle Resolved Ion Scattering Spectrometer (EARISS)

All LEIS experiments have been performed using the EARISS setup, which is described in detail in the thesis of R. Bergmans [17]. The EARISS setup combines a 145 degrees backscattering ESA-LEIS (the actual EARISS analyser and detector), a 35 degrees forward scattering TOF-SARS detector and a 178 degrees backscattering TOF (TOF-CAICISS) detector (see figure 2.7). The advantage of the backscattering geometry is the high resolving power. However, the sensitivity towards lighter elements is small and only species heavier than the projectile can be detected. On the other hand, recoiling spectroscopy is less straightforward to quantify, but is extremely sensitive towards lighter elements. The combination of forward and backscattering LEIS in one machine thus yields complementary information. In this thesis "EARISS setup" refers to the whole setup, including both TOF detectors, whereas "EARISS" refers to the EARISS detector and analyser exclusively.
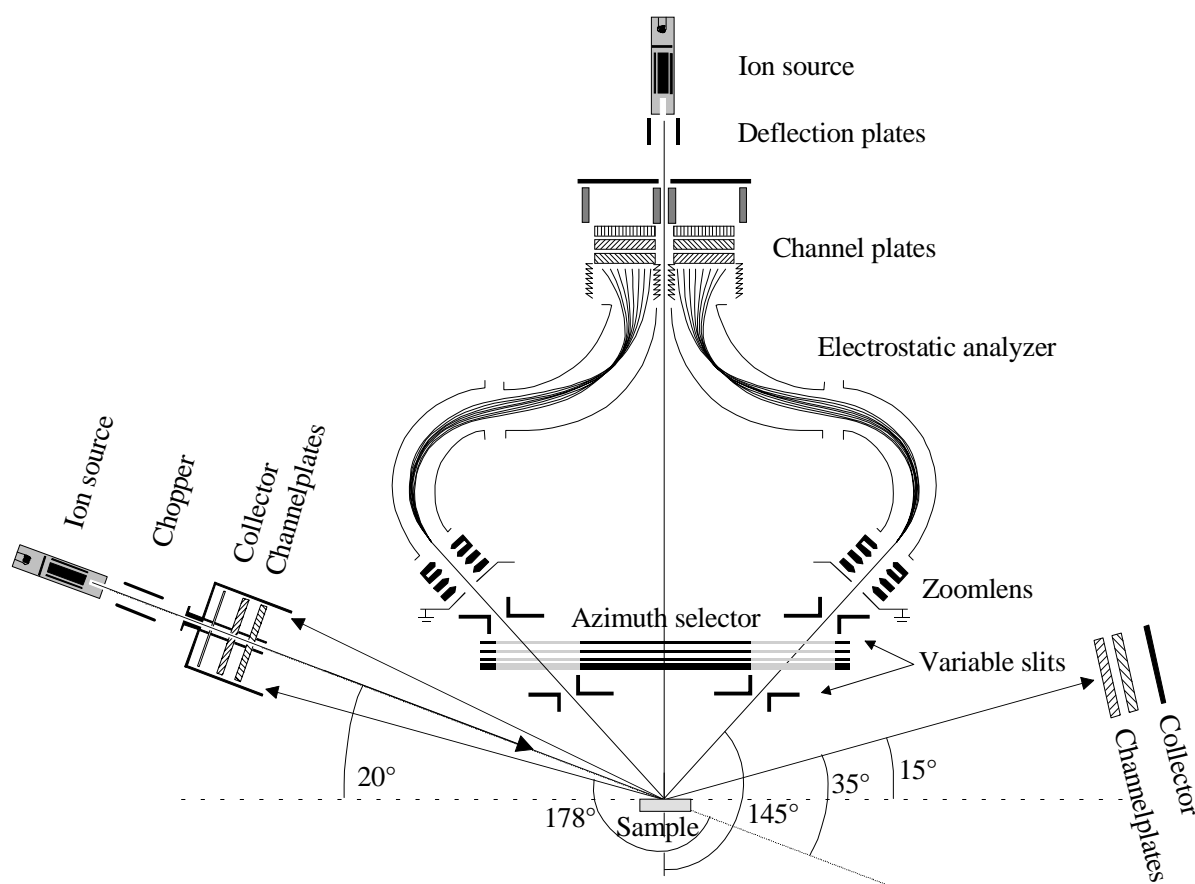
Figure 2.7: *Schematic representation of the EARISS setup, including a 35 degrees forward scattering TOF (TOF-SARS), a near 180 degrees backscattering TOF (TOF-CAICISS detector) and an ESA-LEIS (the actual EARISS analyser and detector).*

The EARISS has been modified to enable the computer controlled measurements of energy spectra. By keeping the pass-energy of the analyser constant and driving the voltage of the last lens element (acceleration/deceleration element), the ions can be energy selected. A fixed pass-energy of 3 keV has been used, which corresponds to an energy image of 300 eV on the detector. Automated calibration measurements were performed on a regular basis to determine the energy dispersion and the range of the detector with constant response (see e.g. figure 3.16 and 3.17 of [35]). The energy steps between LEIS measurements are based on the determined constant response range of the detector of approximately 100 eV. By combining the results of several measurements, taken at different acceleration voltages, a complete energy spectrum is obtained.

2.2.5 LEIS setup: TOF-CAICISS

A schematic picture of the 178 degrees backscattering TOF (TOF-CAICISS), as added to the EARISS setup during the research described in this thesis, is shown in figure 2.8 (see also chapter 2.2.2). Before presenting a more detailed description of the TOF controller, the basic components in figure 2.8 will be discussed. The primary ion beam is shaped by lens 1 so the ions can pass diaphragm 1, which is used for differential pumping of the beam-line. The ions will be

deflected from the centre of the beam line as long as a potential difference is maintained over the chopper deflection plates or if the mass does not correspond to the selected energy-mass ratio of the mass-filter. Only when the ions are not deflected they can pass diaphragm 2 and the central hole of the detector. The ion beam is aimed and focussed on the sample using beam deflection plates 1 and 2 in combination with lens 2. A small part of the scattered particles will return from the sample in the direction of the detector. Ions will only reach the detector if the potential over lens 2 is switched off during their return, whereas neutrals are not deflected by lens 2. The particles that reach the detector with enough kinetic energy cause secondary electrons. The
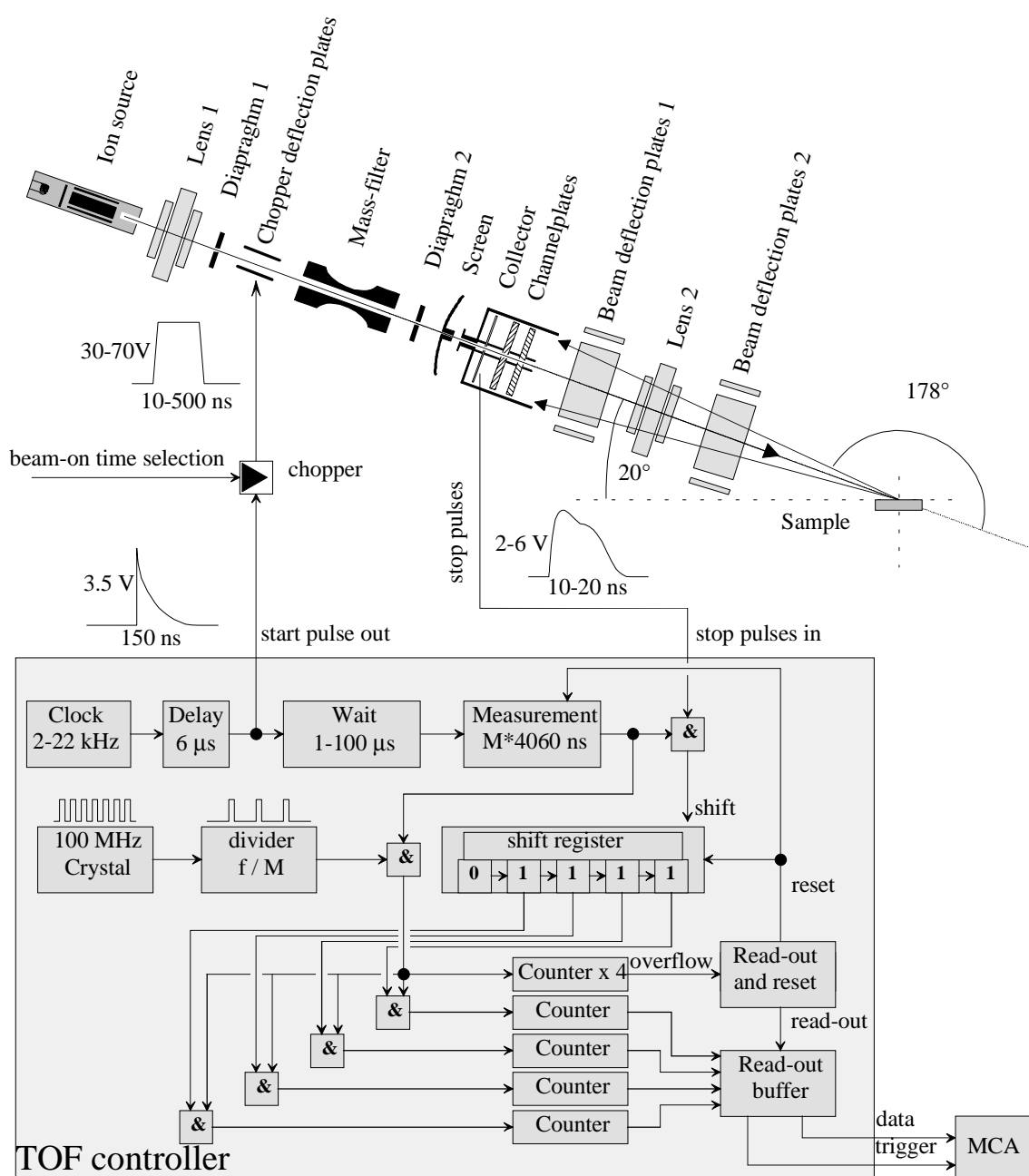
Figure 2.8: *Schematic representation of the backscattering TOF (TOF-CAICISS) and the corresponding multi-TOF electronics. Typical pulse shapes are shown for the TOF-start pulse, the chopping signal and the detection events.*

number of secondary electrons is increased by the channel plates. The secondary electrons that leave the last channel plate are pulled to the collector by a potential difference between the back of the last channel plate and the collector. The resulting signal is shaped and used as a stop signal for the TOF electronics. Finally, the measured flight-time is stored by incrementing the corresponding channel of a Multi Channel Analyser (MCA). A TOF measurement consists of resetting the MCA channels to zero, performing continuously measurement cycles as shown schematically in figure 2.9 and finally collecting the MCA data by computer.
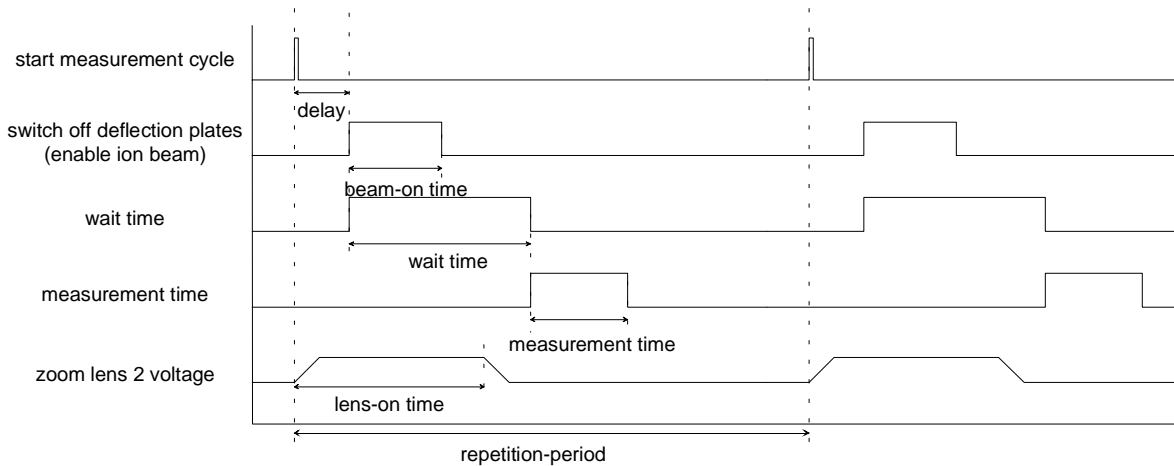
Figure 2.9: *Timing sequence of the repeating Time-Of-Flight measurement loop.*

Below a single measurement loop and the corresponding controller properties will be described in more detail. Detailed information about the electronics of the control unit and the TOF detector is available in the (university internal) spec-sheets by R. Rumphorst. The TOF control unit has two timing control signals, a 100 Mhz crystal which is used for the flight time determination and a variable clock which sets the repetition rate of the TOF measurement cycle. A divider after the crystal sets the clock period of the controller to M*10 ns (see figure 2.8). The repetition rate (or chopping frequency) can be selected between 2 kHz and 22 kHz. The chopper plates are pulled to ground with a delay time of 6 µs with respect to the start of the measurement cycle. During this delay time lens 2 can be switched from ground potential to high voltage. The reason to keep lens 2 on ground potential during the rest of the time is that otherwise returning ions from the previous measurement cycle can not reach the detector. Experiments have shown that the yield from neutrals and neutrals plus ions can be discriminated by switching the voltage on lens 2 on and off. However, since the returning particles in the step-edge measurements are mostly neutrals, this feature has not been used (lens 2 continuously on) during the experiments shown in this thesis. The measurement time window can be shifted with respect to the end of the delay-time by a selectable wait-time between 1 and 100 µs. The flight time is determined by counting the number of clock periods of M*10 ns between the end of the wait time and the stop pulse(s). The counters, that have been initialized to zero, are incremented each clock pulse as long as they are enabled by the high signal on the corresponding output of the shift register. A stop signal from the TOF detector causes one counter to be disabled by shifting zeros through the register. This way it is possible to use four stop signals for each start signal. The last counter is never disabled, causing an overflow after 4096 clock pulses. This overflow signal of the counter

is used to reset the measurement state and to trigger the data-buffering and communication with the external MCA. The sum of the delay time, the wait time and the measuring time should be below the selected repetition rate. At the minimum measuring time of 40.6 μs projectiles can travel more than 2 metres, assuming the combination of the heaviest applied ion Ar$^+$ at the lowest detectable energy of 500 eV (lowest velocity). This is well above the total flight length of the projectiles, so the total time spectrum can be measured at the best time resolution (1*10 ns) without shifting the measurement window. However, the wait time is useful in removing an additional peak in the time-spectrum in front of the peak of the fastest returning particles. This peak is caused by ions that hit the detector side and generate secondary electrons on their way towards the sample. The shield in front of the detector is only partially successful in removing these electrons before they can reach the channel plates.

The first successful TOF-CAICISS measurement with the modified setup, using 4 keV Ne$^+$ on Au, is shown in figure 2.10. In total three peaks are visible, of which the first two are due to the passing of the beam on the way to the sample and the last one is due to the detection of the backscattered projectiles. Each peak is split due to the incomplete filtering of the ^{22}Ne$^+$ isotope by the mass filter. During later experiments the current through the mass filter was increased for
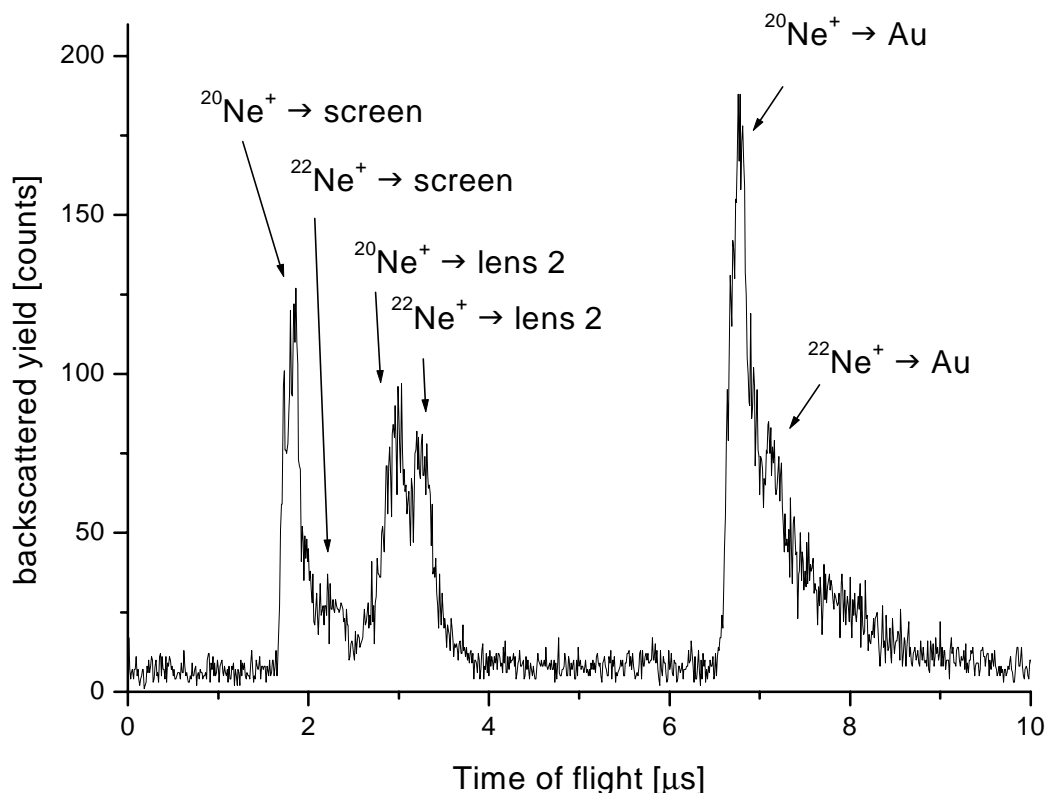
Figure 2.10: *First successful backscattering TOF measurement with the modified TOF setup, using 4 keV Ne$^+$ on Au. Visible in this figure are the stop-pulses due to the passing ion beam on the way to the sample and the stop pulses due to the backscattered Ne.*

better mass separation, resulting in the complete removal of $^{22}Ne^+$. The first peak is caused by secondary electrons that are the result of collisions between projectiles in the ion beam and the screen in front of the detector. The shape of this peak corresponds to the profile of the chopped ion beam. The area of this peak is directly related to the ion dose during the TOF measurement. The backscattering TOF measurements can take a long time and the output of the ion source will vary during the measurement. The additional peak is therefore sometimes useful when normalization of the measured spectra is required. The screen is at a positive voltage to prevent most electrons from reaching the detector. The second peak is caused by secondary electrons that are caused by collisions between the projectiles with the beam line due to the broadening of the beam near lens 2. The magnitude of the second peak depends on the actual trajectories of the ions (lens and deflector settings). The trajectories of the ions depend on their mass, therefore the ratio between the peaks due to $^{22}Ne^+$ and $^{20}Ne^+$ is not equal to the isotope content of the ion beam. The second peak is not attenuated by an "electron-trap" as in the case of the first peak. However, in later experiments the second peak has been prevented by optimizing the beam shape. The Au sample was only partly cleaned before the experiments which explains the large background of the spectrum.

The efficiency of the MCP's has been determined by measuring the backscattered yield minus the background for Ne^+ at several primary energies and detector voltages, using clean Au as the target sample. The measuring time has been varied to compensate for the low yield at small ion energies. The spectra are also corrected for the energy dependent differential scattering cross-section. In figure 2.11 the corrected Ne detection rate is shown as a function of the final projectile
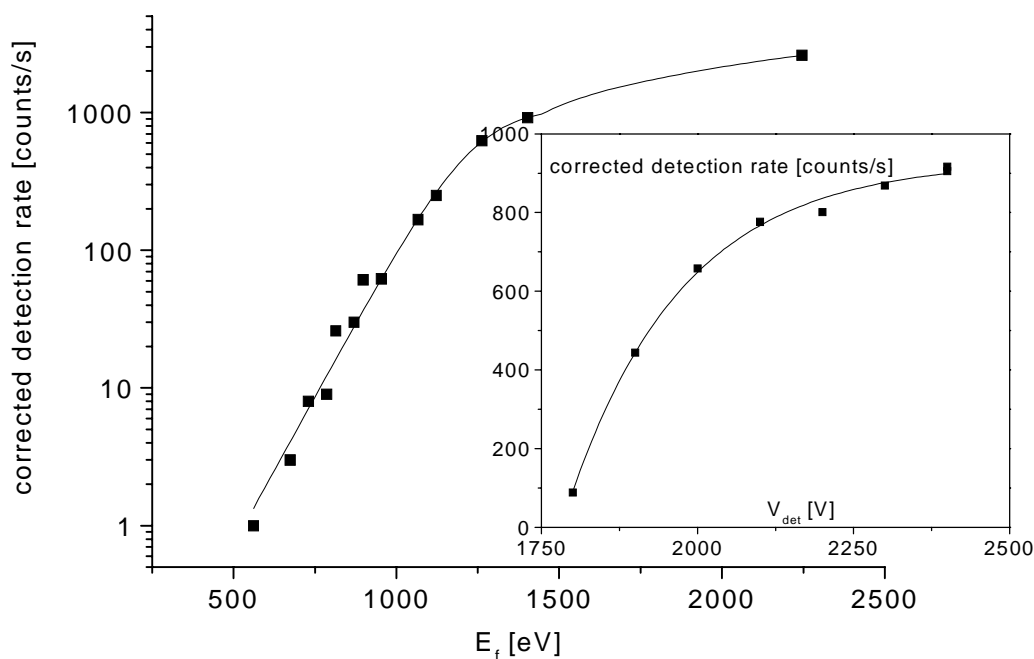
Figure 2.11: *The Ne detection rate as a function of final energy.*

energy E_f at a voltage over the MCP's of $V_{det} = 2300$ V. The inset shows the corrected detection rate as a function of the MCP's high voltage, using 2 keV Ne$^+$ as primary ion, corresponding to a final energy of: $E_f = 1.3$ keV. Saturation is achieved for voltages above $V_{det} = 2100$ V.

Figure 2.11 shows a large variation in detection efficiency over the lower final energy range. A trend line has been added to figure 2.11 based on the exponential behaviour at low final energies and the upper limit as set by the number of returning neutrals times the maximum efficiency of the MCP's. The steep slope at lower final energies suggests that composition measurements should preferably be performed with final energies above 2.0 keV to be insensitive to errors in the primary energy. Figure 2.12 shows the absolute error in the composition determination as a function of the nominal initial projectile energy, assuming a difference of only 10 eV between the primary ion energy during the measurement with respect to the primary ion energy during the calibration. The error has been calculated for Ne$^+$ on Pt-Rh (assuming a nominal composition of 60% Pt) and He$^+$ on Cu-Au (assuming a nominal composition of 50% Au). As shown in figure 2.12, the different shift in detection efficiency for heavy and light atoms can cause an error of one percent in the composition determination for each 10 eV difference
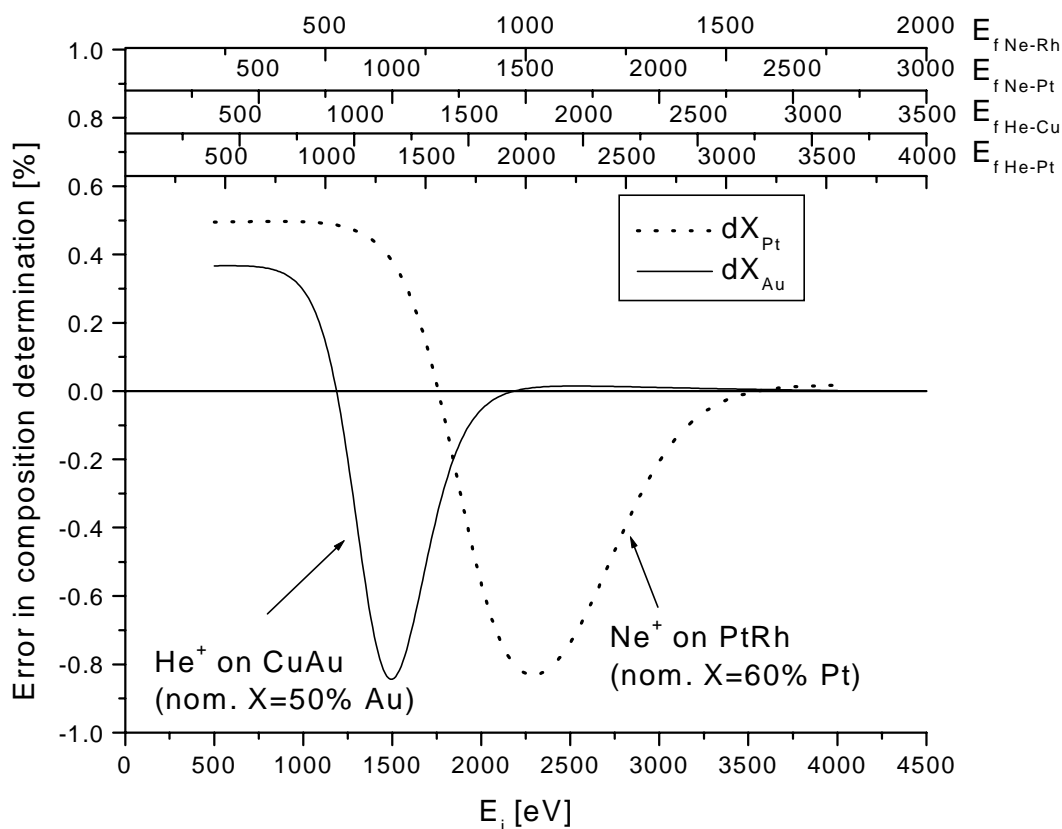
Figure 2.12: *The absolute error in composition determination as a function of the nominal ion energy, assuming an error of 10 eV in initial ion energy during the composition measurements with respect to the initial ion energy during the calibration.*

between the initial ion energy during measurements with respect to the initial ion energy during the calibration. This is only a moderate contribution to the maximum accuracy of the TOF, however, it can be easily prevented by choosing a primary ion energy of at least 4 keV.

2.2.6 Ion trajectory simulations using MATCH

The above described TOF-CAICISS has been added to the EARISS setup to enable step-edge composition measurements. It was expected that the shadow cone of the step-edge atoms (see figure 2.6) could be used to minimize the contributions of other sites to the scattered yield. Simple (and fast) 2D ion trajectory simulations were used to calculate the size of the shadowing cone and to determine the critical angle and the angles at which focussing events occur. However, to determine the optimal scattering geometry for step-edge composition experiments and to calculate the contribution of other sites to the scattered yield, it proved essential to perform 3D ion scattering simulations. The in-house code "SISS-92" [18] is less suited for large unit-cells and grazing angles of incidence. Therefore, we used a modified version of MATCH [19] to perform the ion trajectory simulations. These modifications have been applied to optimize the general purpose code of MATCH for the specific geometry corresponding to step-edge measurements. Below we present a general introduction to MATCH, the modifications that were made and the resulting impact for trajectory simulations at small angles of incidence.

In figure 2.13a the trajectory is calculated for a single ion starting from a random position above the sample with an angle of incidence and initial energy according to the properties of the ion source. For each collision the energy decrease and new direction of the ion are calculated. At the end of the trajectory calculation this ion leaves the sample in a direction that does not correspond to the viewing angle of the detector. In an ordinary ion trajectory simulation this ion would thus cause no detection event. However, in MATCH there are also reverse trajectories calculated for ions that start with a selected final energy and an angle that corresponds to the viewing angle of the detector (see figure 2.13b). Since the trajectories are reversed, the energy is increased instead of decreased for each collision. In the final step the collisions of the ingoing and outgoing trajectories are compared to check if they may be connected. If this is the case, the
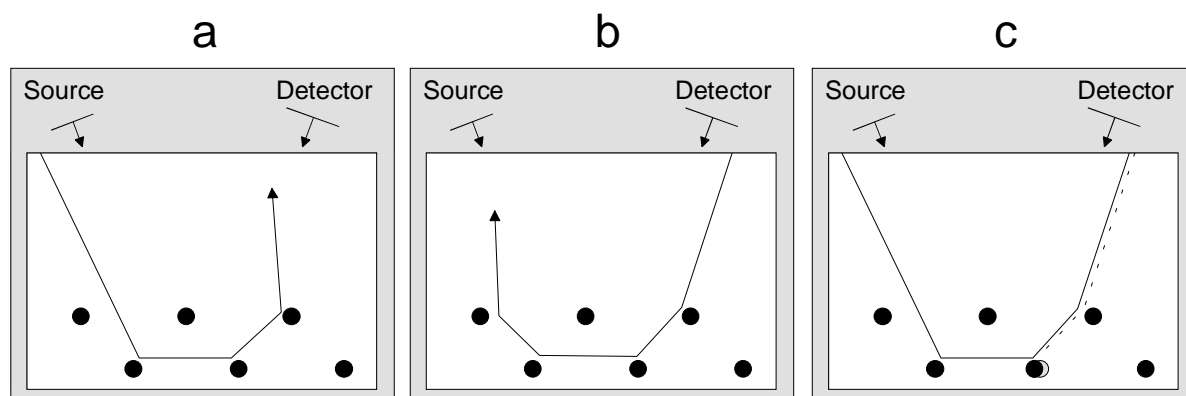

Figure 2.13: *Illustration of the matching method between the incoming and the outgoing trajectories in MATCH.*

atom at which the connecting collision occurs is shifted such that the trajectories near the collision become coincident as shown in figure 2.13c. The chance that the atom is shifted by the required distance is calculated from a Gaussian distribution, based on the thermal vibrations of the atoms. MATCH only connects the collisions, not the trajectories. The shifting of the complete outgoing trajectory as shown in figure 2.13c should therefore be regarded as an illustration only. The matching of incoming and outgoing trajectories is more efficient than full ion trajectory simulations. However, the trajectories may be connected at several collision points if the ingoing and outgoing trajectories are almost similar. One of the modifications to MATCH is the improved detection and prevention of such multiple counting events. At small angles of incidence there are only a few trajectories that can cause detection events. Therefore this modification is especially important for the scattering geometry that is used for step-edge composition measurements.

In the trajectory simulations it is assumed that the projectile has interaction with only one atom at a time and that the projectile travels over straight line segments between the collisions (binary collision approximation: BCA [20]). Double collision events, which occur for projectile trajectories halfway between two atoms, are treated by sequential evaluation of the collisions using the same initial energy and velocity. In the original implementation of MATCH, the collision partners are determined by calculating the closest atom to the current collision partner in the direction of the ion. A neighbour list, containing all the atoms that are within a pre-defined distance, is kept by all atoms to speed up the calculations (see figure 2.14a). The next-collision partner searching routine has been significantly improved by searching only through the list of
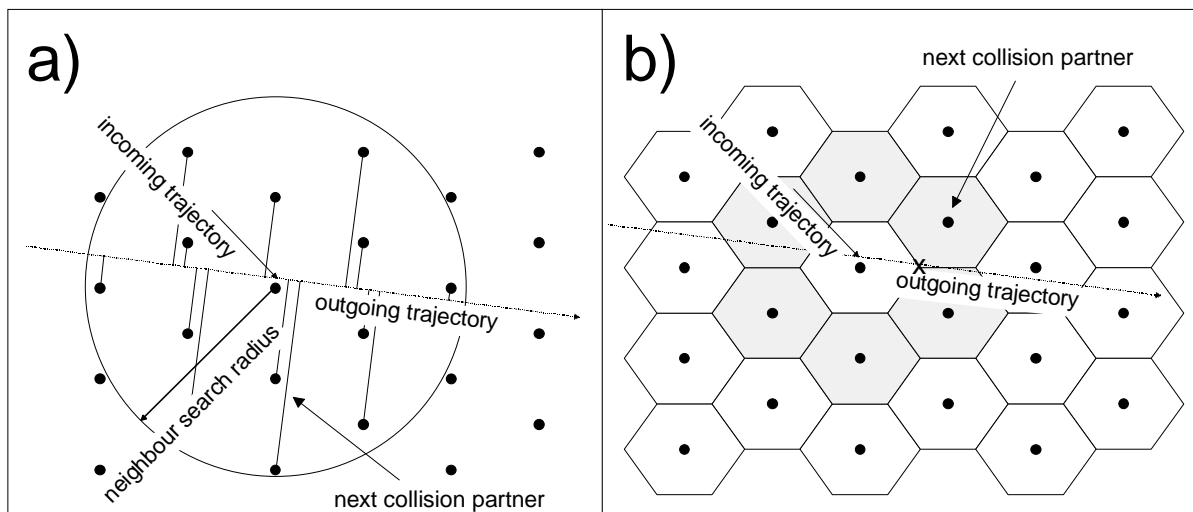
Figure 2.14: *a) Next collision partner searching through a list of neighbours based on a maximum radius around the current collision partner. The next collision partner is the atom that has the closest projection with respect to the current collision partner. b) Optimized next collision partner searching by using the list of nearest neighbours of the current atom, found by calculating the convex hulls of all atoms in the simulation slab. The convex hulls of the atoms are indicated by the hexagons. The grey hexagons are the nearest neighbours of the current collision partner, and therefore the only candidates for the next collision. The next collision partner is found by searching the shared vertex where the ion is leaving the convex around the current collision partner.*

nearest neighbours of the current collision partner. The nearest neighbours of an atom are determined by calculating the convex hulls of the atoms, as has been explained in detail in [18] and is shown schematically in figure 2.14b. The quick hull code [21] has been used to determine the convex hulls of the atoms in the simulation slab. As shown in figure 2.14 the next collision partner may be different for the two next-collision partner searching methods. This apparent contradiction is caused by the fact that the original method can return a collision partner that is too far away from the ion trajectory. The ion will therefore proceed without deflection and a next potential collision partner is searched. The first collision partner that is close enough to the trajectory to actually cause a deflection will be the same collision partner as found by the method shown in figure 2.14b. The latter method is thus more efficient as there are less candidates during the search for the next collision partner, whereas the found collision partner is the first one that can actually cause a deflection of the ion trajectory. At small angles of incidence the projectiles skim a large distance over the surface. As a result the number of collisions (and thus the number of neighbour searches) during the simulation of a single trajectory is much larger in the geometry used for step-edge composition measurements than for large angles of incidence. This is why the optimization of the neighbour search routine especially pays off for simulations in the geometry that is used for step-edge composition measurements.

Two methods have been used to simulate an infinite crystal during the ion trajectory simulations in the case of vicinal crystals. The first approach uses the original back wrapping method of MATCH, shown schematically in figure 2.15a. By constructing a unit cell of the vicinal crystal that is periodically in the horizontal direction, the back wrapping of the ions can be performed by a horizontal translation only. The advantages are the simple back wrapping method and the obvious relation between the simulation slab and the real surface of vicinal crystals. The disadvantage is that the generation of the unit cell takes more effort. In the second method, shown schematically in figure 2.15b, the terraces are kept parallel to the simulation slab.
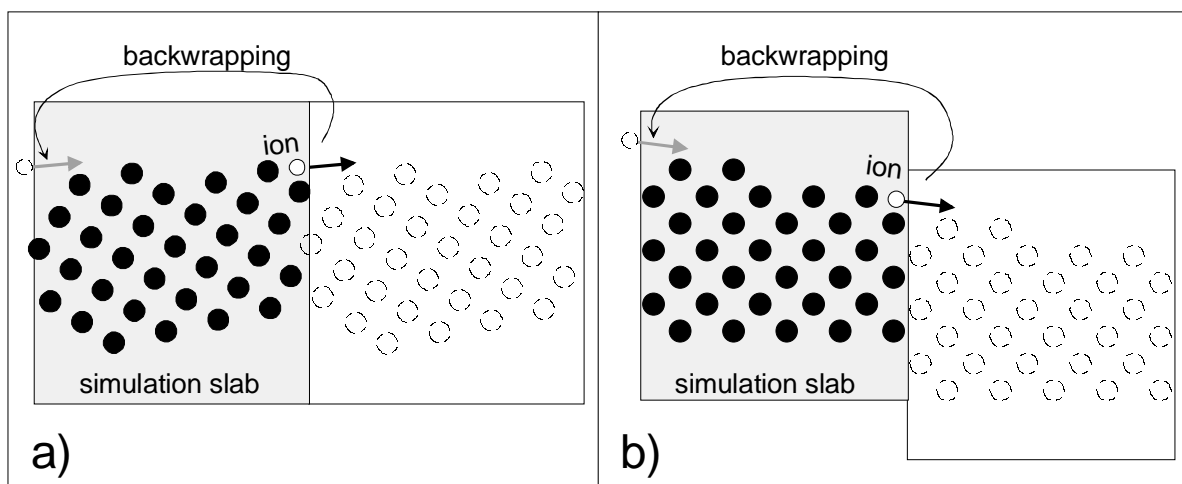
Figure 2.15: *Back wrapping method to simulate an infinite crystal with a finite simulation slab. a) In the case of a periodical simulation slab the back wrapping requires a horizonal translation of the ion only. b) In the case of a semi-periodical simulation slab the back wrapping requires a horizontal and vertical translation.*

The advantages of this method are the straight forward discrimination between the atomic layers and the simple generation of the simulation slab. However, in this case the back wrapping of the ions requires more effort. Another modification to MATCH deals with the composition of the simulation slab. In the original MATCH the atom type at a certain lattice site is fixed after the reading of the lattice definition. In the modified MATCH, the atom type is determined during the collision, based on the defined chance on finding a certain atom type at that lattice site. However, due to the current implementation, this modified version of MATCH can only be used for binary systems.

The scattering angle and the energy increase respectively decrease for each collision is calculated by the evaluation of the so-called scattering integral. In the centre of mass system (CMS) the scattering angle between a projectile with kinetic energy E_0 and mass m_1 (see figure 2.5) and a target atom m_2 can be calculated according to a repulsive potential $V(r)$, the screened Coulomb potential [15], between the projectile and the target atom [15, 18]:

$$\theta_{cms} = \pi - 2s \int_{r_m}^{\infty} \frac{dr}{r^2 g(r)} \quad, \tag{23}$$

with s the impact parameter according to figure 2.5. The distance of closest approach r_m is calculated from $g(r_m) = 0$ with:

$$g(r) = \sqrt{1 - \frac{V(r)}{E} - \frac{s^2}{r^2}} \quad, \quad E = \frac{AE_0}{1+A} \quad, \quad A = \frac{m_2}{m_1} \tag{24}$$

The scattering angle in the laboratory system is related to the scattering angle in the CMS according to:

$$\tan\theta = \frac{A\sin\theta_{cms}}{1+A\cos\theta_{cms}} \tag{25}$$

The intersections of the trajectory asymptotes with the ion trajectory (x1) respectively original target atom position (x2) are approximated by (see figure 2.5):

$$x1 \approx s \, \tan\frac{\theta}{2} \qquad x2 = \frac{s}{\tan\xi} - x1 \tag{26}$$

The evaluation of equation (23), the scattering integral, has to be performed numerically. Therefore a look-up table is generated before the simulations. The screening length for the

screened Coulomb potential of the used elements has been taken from literature. The energy decrease due to a collision for the ingoing trajectories, respectively energy increase for outgoing trajectories, is calculated according to equation (21), using the scattering angle according to equation (23) and equation (25) as input. Also the latter calculation is performed prior to the simulations and stored in a look-up table so speed up the simulations.

2.3 X-Ray Standing Waves

X-Ray Standing Waves (XSW) is a technique that can be used to accurately determine the position of atoms with respect to a (well defined) lattice. As such it is usually applied to determine the site of ad-atoms on or in single crystals. The XSW technique is based on the standing X-Ray wave field that is the result from the interference between the incoming beam and the diffracted beam at the Bragg condition. By scanning the Bragg condition, the phase of the standing wave field is shifted perpendicular to the substrate lattice planes that cause the diffraction. The Bragg condition can be scanned by varying the wavelength of the incident X-Ray (primary energy) or by varying the angle of the crystal with respect to the beam. The ad-atoms will be excited when they coincide with the anti-nodes of the standing wave field. The position of the ad-atoms can be determined with respect to the substrate lattice planes (see figure 2.16)
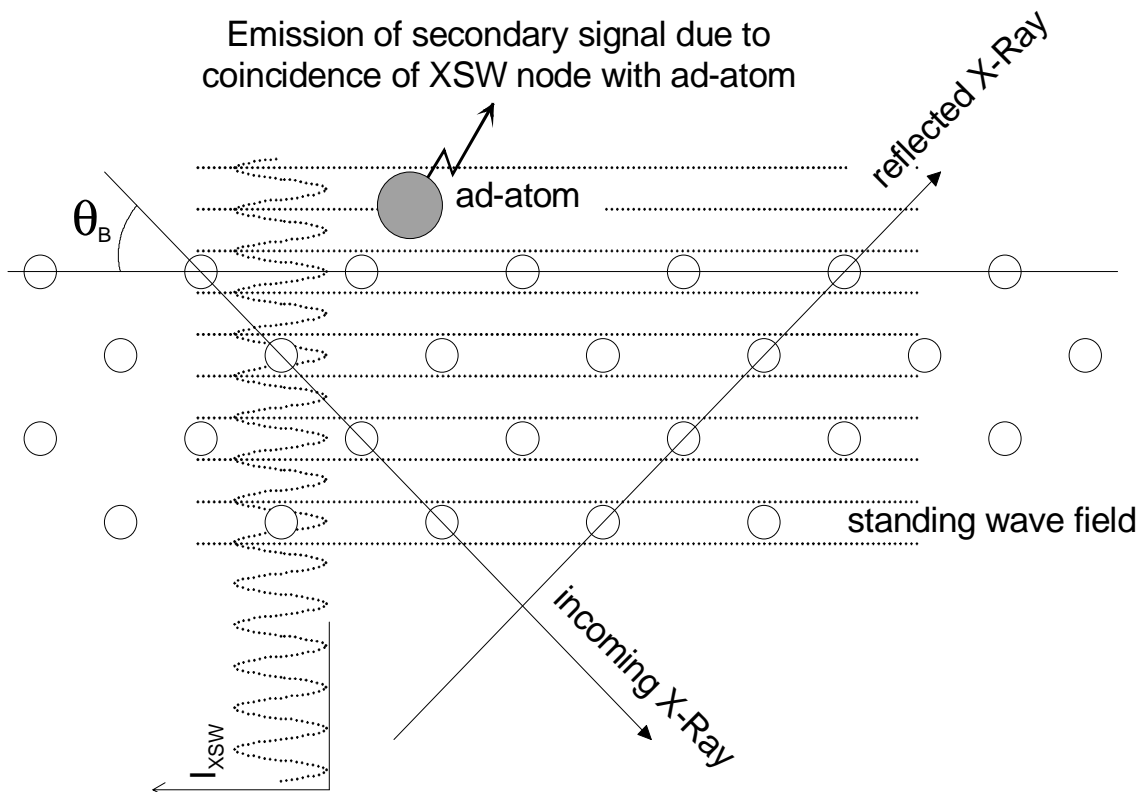
Figure 2.16: *Schematic representation of the generation of a standing wave field due to the interference of the incoming X-Ray and the reflected X-Ray. The coincidence of a XSW anti-node with an ad-atom will cause a secondary signal (electrons/fluorescence) which can be detected .*

by recording a secondary signal (e.g. fluorescence or secondary electrons) as a function of the wave field phase. The position of the ad-atoms can be triangulated by combining the results of the measurements in at least three independent directions.

At a fixed primary energy of the incident X-Ray, the Bragg condition is usually satisfied over only a very small angular range ($<<1°$). The XSW technique can therefore only be applied to substrates with an almost perfect lattice. This is one of the reasons that XSW was initially only applied to semiconductor single crystal substrates. However, by using a (near) normal incident beam, the Bragg peak increases sufficient to enable the application of XSW on metal single crystals with mosaicity up to 1°. This is demonstrated in figure 2.17 which shows the so-called rocking curve of Fe(110) prior to XSW measurements in the <220> direction, at two selected primary energies of the incident X-Ray beam. The yield presented in figure 2.17 is the number of detected secondary electrons during the tilting of the Fe(110) sample with respect to the beam, which is a measure for the diffraction efficiency (and as such for the correlation with the Bragg condition). At a primary energy of $E_i = 6105$ eV the Bragg condition is satisfied at an angle of
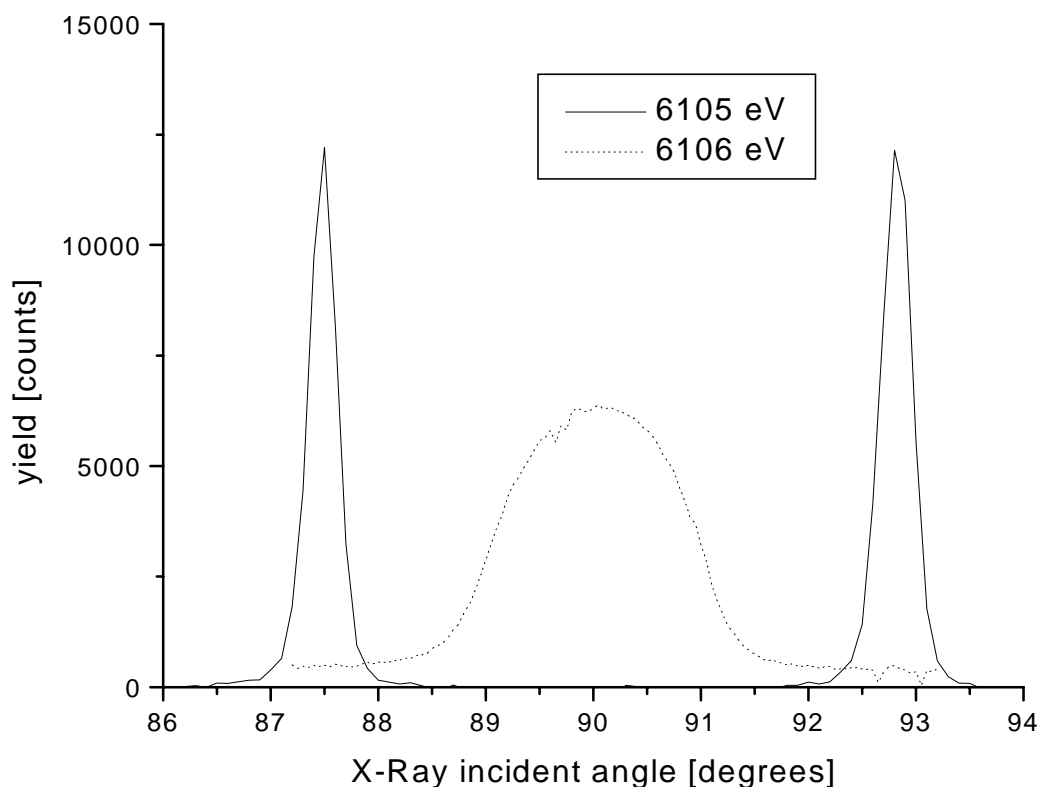
Figure 2.17: *The measured reflectivity as a function of the angle between the X-Ray beam and the lattice planes for two primary energies, corresponding to different angles where the Bragg condition is satisfied. The figure shows that the Bragg condition for a primary energy of $E_p = 6106$ eV, corresponding to $\theta_B = 90°$, is satisfied over a larger angle than for a primary energy of $Ep = 6105$ eV.*

$\theta_B = 87.5°$ between the lattice planes and the incident beam. In this scattering geometry the Bragg condition is satisfied over half a degree. For a primary energy of $E_i = 6106$ eV the Bragg condition is satisfied at $\theta_B = 90.0°$, in which case the Bragg condition is satisfied over almost two degrees. This is significantly larger than the mosaicity of the used Fe(110) crystal of $\pm 0.06°$. See [22, 23] for a detailed discussion of the XSW technique.

References:

1. J.W. Gibbs, The collected works of J.W. Gibbs, Vol. 1, Langman, Green and Co., New York USA (1973)

2. D. Mac Lean, Grain boundaries in metals, Oxford Univ. Press London (1957)

3. F.L. Williams, D. Nason, Surf. Sci. 45 (1974) 377

4. F.J. Kuijers, B.M. Tieman, V. Ponec, Surf. Sci. 75 (1978) 657

5. L.E. Reichl, A modern course in statistical physics, University of Texas Press USA (1980), ISBN 0-7131-35174

6. J. Du Plessis, Surface segregation, Solid State Phenomena vol. 11, Sci-Tech Publications, ISBN: 3-908044-06-5, Vaduz Lichtenstein 1990

7. F.L. Williams, D. Nason, Surf. Sci. 45 (1974) 377

8. T.J. Raeker, D.E. Sanders, A.E. DePristo, Surf. Sci. 248 (1991) 134

9. T.S. King, R.G. Donnely, Surf. Sci. 141 (1984) 417

10. A.M. Schoeb, T.J. Raeker, L. Yang, X. Wu, T.S. King, A.E. DePristo, Surf. Sci. 278 (1992) L125

11. D. Marquardt, An algorithm for least-squares estimation of nonlinear parameters, SIAM J. Appl. Math. 11 (1963) 431-441

12. H. Niehus, W. Heiland, E. Taglauer, Surf. Sci. Reports 17 (1993) 213

13. R.H. Bergmans, M. Van de Grift, A.W. Denier van der Gon, R.G. van Welzenis, H.H. Brongersma, S.M. Francis, M. Bowker, Nucl. Instr. And Meth. B 85 (1994) 435

14. R. Cortenraad, S.N. Ermolov, B. Moest, A.W. Denier van der Gon, V.G. Glebovsky, H.H. Brongersma, accepted for publication in Nucl. Instr. and Meth. B.

15. M.C. Langelaar, Growth and atomic structure of iron-silver layers (1998) ISBN: 90-367-0853-2

16. M. Aono, M. Katayama, E. Nomura, T. Chassé, D. Choi, M. Kato, Nuclear Instruments and Meth. in Phys. Research B37/38 (1989) 264

17. R. Bergmans, Energy and angle resolved ion scattering and recoiling spectroscopy on bimetallic systems (1996) ISBN 90-386-0057-7

18. C.A. Severijns, Computer simulation of Low-Energy Ion Scattering, PhD thesis (1992), Eindhoven

19. M.H. Langelaar, M. Breeman, A.V. Mijiritskii, D.O. Boerma, Nucl. Instrum. Meth. Phys. Res. B (1997) 587

20. J.P. Biersack, L.G. Haggman, Nucl. Instr. Meth. 174 (1980) 257

21. http://www.geom.umn.edu/locate/qhull

22. J. Zegenhagen, Surf. Sci. Rep. 18 (1993) 199

23. D.P. Woodruff, D.L. Seymour, S.F. McConville, C.E. Riley, M.D. Crapper, N.P. Prince, Surf. Sci. 195 (1988) 237

The adsorption site of K on Fe(110) studied with XSW

3

3.1 Abstract

We have used X-Ray standing waves (XSW) at near normal incidence to determine the K-Fe bond length and the adsorption site of K at the saturation coverage at room temperature on the Fe(110) surface. Three different scattering geometries were used to enable the determination of the adsorption site by triangulation. From the results we conclude that the potassium atoms adsorb in a distorted hexagonal overlayer. The Fe-K distance, as determined from the measurements in the (220) Bragg reflection, is 3.4 ± 0.2 Å. The long bridge site seems to be the preferred adsorption site for the potassium atoms in the distorted hexagonal overlayer. This geometry not only fits all the XSW data, but also explains all spots in the LEED pattern without the need to introduce multiple scattering. Comparison of the measured and simulated XSW data, based on the distorted hexagonal overlayer, enables a more accurate determination of the Fe-K bond length to 3.36 ± 0.14 Å. This corresponds to a potassium hard sphere radius of $r_K = 2.12 \pm 0.14$ Å. This radius is among the largest reported for potassium on a metal, which can be attributed to the high coordination and the large coverage.

3.2 Introduction

The technological interest of alkali on metals for e.g. electrodes [1] and heterogeneous catalysts [2, 3] have made it a rewarding subject of studies in the past. Furthermore, alkalies on metals have been taken as a model system for adsorption since the 1930's because of the pre-assumed simplicity [4]. This point of view was challenged by the 1983 discovery of atop adsorption of Cs on Cu(111) [5], as opposed to the generally expected high coordinated adsorption site [6], as well as theoretical work by Ishida and coworkers [7, 8]. These results did lead to a series of renewed investigations. Many of the experiments showed that "abnormal" site adsorption is the rule rather than the exception for alkalies on metals [9, 10], including potassium [11, 12]. See the reviews by Diehl and McGrath [6, 13] for a summary of many of these structural studies.

The aim of the experiments presented in this paper was to determine the K-Fe bond length and the potassium adsorption site on Fe(110). See table 10 of [13] for the adsorption site and the effective potassium radius in the case of potassium adsorption on various other metal substrates. Potassium on iron is widely used as a promoted catalyst in ammonia synthesis [14, 15] and the hydrogenation of CO [16, 17, 18]. Here the potassium will, in most cases, behave ionic. Despite the practical importance of K/Fe, there are only a few papers on the clean K/Fe(110) system [19, 20]. One of the reasons is the extreme reactivity towards residual oxygen, especially near the potassium saturation coverage, when the sticking coefficient for oxygen approaches unity [21]. At room temperature, a close packed hexagonal overlayer has been reported near saturation coverage on the unreconstructed Fe(110) surface based on Low Energy Electron Diffraction (LEED) measurements [20]. This structure has been compared and assumed similar to the one as introduced for the Cs/W(100) system [22] (see figure 3.1). The K saturation coverage corresponds to 0.31 monolayer (ML) [20], where a ML is defined as the density of Fe atoms at the surface ($1.72*10^{15}/cm^2$). For a perfect hexagonal overlayer at this coverage, the K-K distance is 4.68 Å (figure 3.1). Locking of the K atoms in the Fe rows might be expected since the K-K row distance is twice the Fe-Fe row distance in the $[\bar{1}10]$ direction (figure 3.1). However, the LEED patterns do not give information concerning the lateral position of the potassium atoms relative to the iron substrate. Therefore we used X-Ray Standing Waves (XSW) to determine the adsorption site of K on Fe(110) and Spot Profile Analysis of Low Energy Electron Diffraction (SPA-LEED) to study the morphology. See e.g. ref [23, 24] for a detailed description of the SPA-LEED technique and [25, 26] for details on the XSW technique.

It has been shown that the position of adsorbates can be determined accurately with XSW by recording a secondary signal (ions/electrons/fluorescence) which is induced by a standing X-Ray wave field [27]. The demands on crystal quality, imposed by the small width of the Bragg reflections, made XSW at first especially useful in determining the adsorbate bond lengths on semiconductor crystals [28]. However, due to the increasing quality of both metal single crystals and the XSW setups, XSW is now routinely used on metal substrates, too [29]. In most XSW

experiments on metal crystals, the Bragg angle is chosen near 90 degrees to increase the intrinsic width of the Bragg reflection, thereby decreasing the sensitivity towards crystal imperfections. With this technique, which is also known as Normal Incidence X-Ray Standing Waves (NIXSW), it has been shown by e.g. Woodruff et al. that the position of adsorbates can even be determined on crystals with a mosaicity of several tenths of a degree [30].
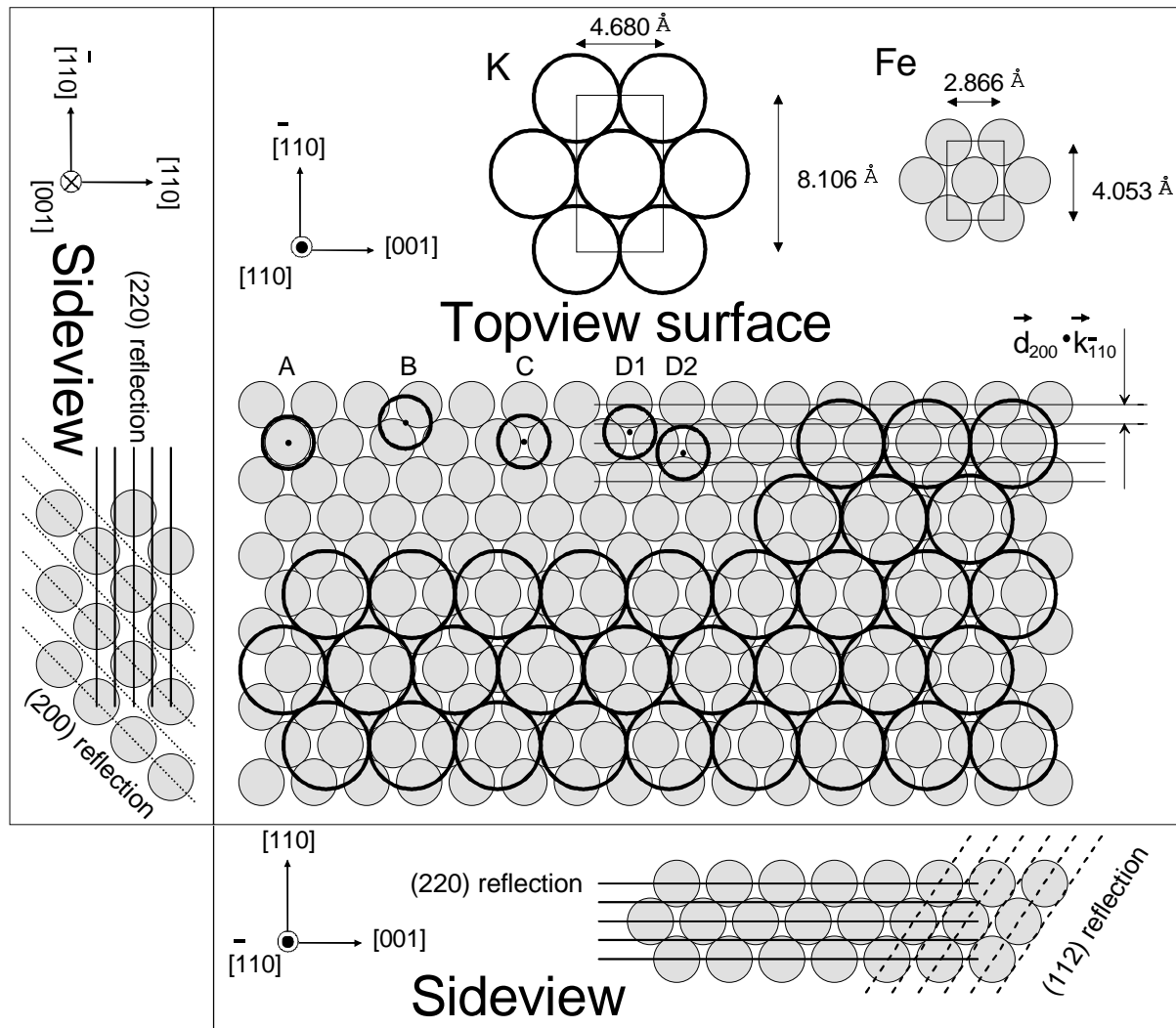
Figure 3.1: *Schematic representation of the hexagonal potassium overlayer on the Fe(110) substrate surface. The Bragg reflections that have been used are indicated in the side views. The possible adsorption sites that have been taken into account in this paper are: a) Atop site b) short bridge c) long bridge d1&d2) three fold hollow*

3.3 Experimental

The Fe(110) sample was cut within 0.1° off the (110) orientation and the final polishing step was carried out with a roughness below 0.05 μm [31]. The experiments have been performed in two different UHV systems. For the XSW measurements the BW1 undulator beam line of the Hamburg synchrotron radiation laboratory (HASYLAB) [32] was used (see figure 3.2), whereas

the other experiments were performed on the SPA-LEED instrument in Eindhoven [33]. The sample was cleaned by sputtering with 2 keV Ne^+ at elevated temperatures (900-1000 K). Ne^+ was chosen in favour of Ar^+ to avoid the overlap of the argon K_β and the potassium K_α fluorescence peaks in the XSW experiments. At the end of the cleaning cycle, the sample was kept five minutes at 850 K to reduce the segregation of contaminants during the surface reconstruction. The sample cleanness was checked with Auger Electron Spectroscopy (AES) in the SPA-LEED apparatus. The level of contamination was below the detection limit (<0.01 ML), even after storing the cleaned sample several hours in the main chamber ($4*10^{-11}$ mbar). The temperature of the sample was measured with a CHINO comet 1000 pyrometer with an absolute accuracy of $\pm50°C$ and a reproducibility within $\pm10°C$. The surface structure was checked with LEED in both systems, it showed sharp peaks belonging to a unreconstructed bcc(110) structure on a low background. On this clean and ordered surface, potassium was evaporated from a well degassed commercial K SAES source [34] while the sample was kept at room temperature (RT). During the evaporation in the SPA-LEED machine, the pressure did not exceed $2*10^{-10}$ mbar. The pressure during potassium evaporation in the XSW setup was below $1*10^{-10}$ mbar. The sticking coefficient for oxygen of the surface was found to increase strongly upon potassium adsorption, reaching near unity at saturation coverage in agreement with literature [21]. Therefore, the time available for measurements after preparation of the K covered surface was 30 minutes before notable contamination was observed. This limited the available time for obtaining XSW measurements, as discussed below.

3.3.1 XSW experiments

A schematic representation of the used XSW setup is shown in figure 3.2, a more detailed description of the XSW setup used for the experiments is given in reference [35]. In order to measure the (220), the (200) and the (112) Bragg reflection, the beam line was tuned to photon energies around 6.1 keV, 4.3 keV and 5.3 keV, respectively (see table 3.1). The intensity
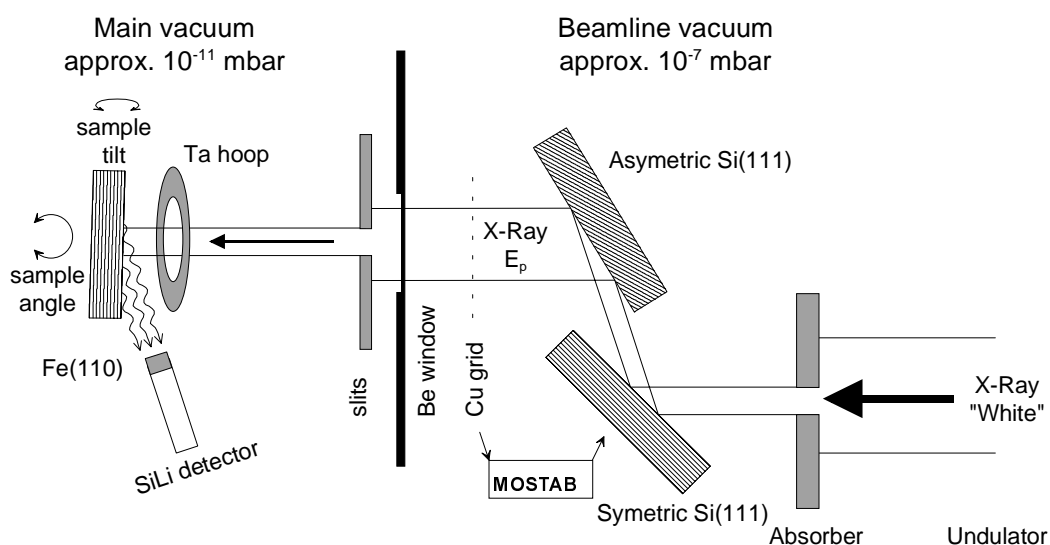

Figure 3.2: *The experimental setup at BW1 for the XSW experiments.*

stabilisation of the incoming beam is carried out by a feedback loop to the Si(111) monochromators (MOSTAB). The required reference signal was measured by a Cu grid, positioned far from the sample to avoid multiple reflections. The sample was placed in a computer controlled manipulator in an ultra high vacuum (UHV) system. This UHV system, with a base pressure in the 10^{-11} mbar region, is separated from the beam line vacuum by a Be window. The reflected signal was measured by the photo current on a Ta wire hoop, whereas the secondary fluorescence signal was measured by an UHV SiLi detector. The SiLi detector is a solid state device that is nitrogen cooled to reduce the thermal noise, in which the X-Rays interact with the silicium to produce electron-hole pairs. The resulting number of pairs is proportional to the energy. The charge is collected and converted to a voltage by a pre-amplifier. For the iron signal the L_α line was used (0.7 keV), whereas the K_α line (3.3 keV) was used for the potassium signal. After alignment the sample was turned $0.5°$ away from the perfect backscattering geometry in the $[\bar{1}10]$ direction to avoid reflections to the source (Cu grid), which would lead to MOSTAB instability. Under these conditions the rocking curve has a typical width of two degrees. Three different reflections have been used to enable the determination of the potassium adsorption site by triangulation: these are the (220), the (200) and the (112) Bragg reflection. The (220) direction exclusively yields information about the Fe-K distance perpendicular to the surface. With this information known, the (200) and (112) reflections can be used to extract information about the in-plane position of the potassium. The (112) respectively (200) reflection planes are indicated by dashed lines in the side view of figure 3.1, the (220) reflection plane is indicated by the solid lines.

Table 3.1: *Diffraction plane spacing (d), incident photon energy (E_p), angle between the surface of the sample and the detector (Θ_{SiLi}) and the Fe signal information depth (k) for the used Bragg reflections.*

reflection	d (Å)	Ep (eV)	Φ^{SiLi} (degrees)	k (μm)
(220)	1.01	6118	~ 3	~ 0.1
(200)	1.43	4327	~ 3	~ 0.1
(112)	1.17	5299	~ 35	~ 1.0

The SiLi detector was placed in a glancing angle with respect to the surface of the Fe(110) crystal for the (220) and the (200) reflection to improve the signal to background ratio for the potassium signal. In the case of the (112) reflection this was not possible and the sample had to be tilted 35 degrees towards the detector. After the cleaning and reconstruction of the surface, the alignment of the sample and optimization of the SiLi placement took between one and three hours. As shown by previous studies [36] and our measurements in the SPA-LEED, the pickup of contamination during this time can be neglected because of the low sticking coefficient of clean Fe(110). After potassium evaporation in 10 minutes, there were taken one to three XSW spectra of 15 minutes each. After the XSW measurements, the sample was transferred to a LEED system. Due to the higher base pressure of the LEED chamber ($1*10^{-9}$ mbar) and the required transfer time (15-30 minutes) in combination with the increased reactivity after potassium deposition, the observed hexagonal spots were faint in most cases. Occasionally a transformation

from a hexagon to a c(2x2) pattern took place during the LEED observations. In the final analysis we only used the experimental data where the hexagon was still visible after the experiments.

3.4 Results

3.4.1 SPA-LEED results

After cleaning and reconstruction of the Fe(110) crystal the morphology of the surface has been studied with SPA-LEED. The LEED pattern of the clean Fe(110) showed a sharp (1x1) on a low background. The LEED pattern of the clean Fe(110) is shown in figure 3.3a. In figure 3.3b the schematic representation is given with the (00) spot in the centre and the four first-order spots in a rectangle around it. The average terrace length and the step height of the Fe(110) crystal were determined from the energy dependence of the (00) spot profile [33]. From the results it was concluded that the Fe(110) crystal has single atomic height steps [37] and an average terrace width of 500 Å. During potassium deposition there were no stable superstructures
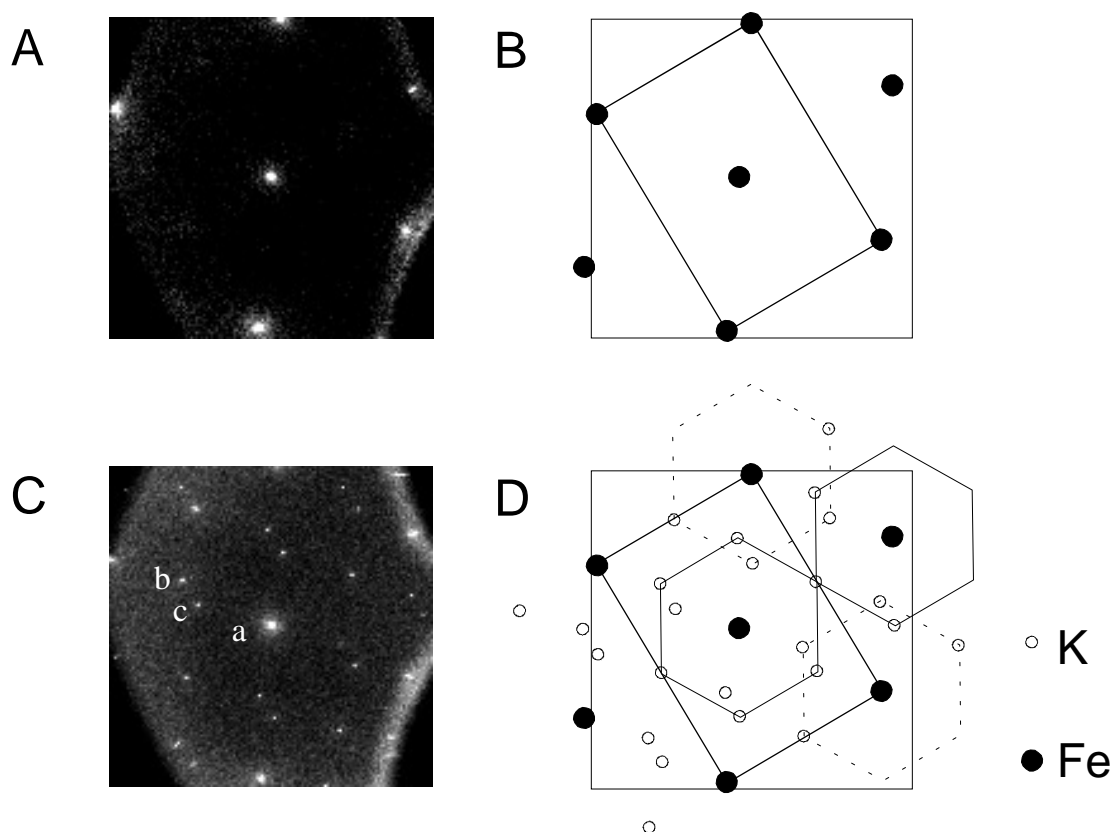
Figure 3.3: *The measured LEED patterns and their schematic representation. a) Measured LEED pattern of clean Fe(110) b) Schematic representation of the LEED pattern of clean Fe(110) c) Measured hexagonal LEED pattern of K/Fe(110) at saturation potassium coverage. The spots marked with "a" are caused by the iron substrate, the "b" marked spots originate from the hexagonal structure by single scattering and the spots that are marked with "c" can be caused by multiple scattering events d) Schematic representation of the hexagonal LEED pattern*

observed until the saturation coverage was reached, at this point the hexagonal LEED pattern emerged. The LEED profile of the hexagonal structure is shown in figure 3.3c and is in agreement with previous publications [20]. The schematic representation, as proposed by [20], is shown in figure 3.3d. The solid circles in figure 3.3d represent the part of the LEED pattern that is caused by the Fe(110) lattice. The open circles represent the pattern as caused by the hexagonal potassium overlayer (shown in figure 3.1). The open circles which are connected by the solid hexagons are single scattering spots, the spots which are connected by dashed hexagons are spots that could be caused by double scattering events. Based on the rapid decrease in intensity for multiple scattering events, higher order scattering is expected to yield low intensities [38]. Not taken into account I-V characteristics, one would thus expect a significantly lower intensity from the double scattering spot (marked with "c" in figure 3.3c) than from its equivalent single scattering spot (marked with "b" in figure 3.3c). This is clearly not the case for the measured LEED patterns. In the discussion section we will present a possible alternative explanation for the additional spots which does not introduce multiple scattering.

3.4.2 XSW results

In earlier XSW and SPA-LEED experiments on the same Fe(110) crystal [33], the mosaicity was found to be 2.1 mrad ($\pm 0.06°$). Due to the large intrinsic width of the rocking curve in the chosen geometry (2°), this mosaicity has little effect on the results of the XSW experiments. The measurements have been performed by varying the energy at a chosen Bragg angle, while recording the reflectivity (photo current on the Ta wire hoop) and the fluorescence signal (SiLi detector). Most measurements have been performed with an energy resolution of $\Delta E = 1.0$ eV yielding sufficient resolution and acceptable statistics within the available time of the experiment, which was limited due to impurity pickup from the vacuum as discussed above. In addition, some measurements were performed with an energy resolution of $\Delta E = 1.5$ eV in order to cross check for structural changes throughout the slower measurements at an energy resolution of $\Delta E = 1.0$ eV. The energy resolution was tuned by varying the collimator slit width between the source and the monochromator. Each XSW measurement consists of 32 fluorescence spectra which are taken at constant incident photon energy intervals. The secondary signals of the iron and the potassium were determined by fitting the fluorescence spectrum for every data-point (energy).

Due to the shallow detection angle in the (220) and the (200) Bragg reflection geometry, the iron fluorescence signal was very weak leading to a large statistical scatter of the data. Therefore the Fe fluorescence yield was evaluated for the (112) Bragg reflection data only. The integrated fluorescence intensity for potassium (triangles) as a function of incidence photon energy is shown in figure 3.4a-c. The reflectivity data (rocking curve) is given by the squares in the same figure. In figure 3.4c, the iron fluorescence yield (circles) is also shown. The energy resolution and energy offset are determined by fitting the rocking curve.
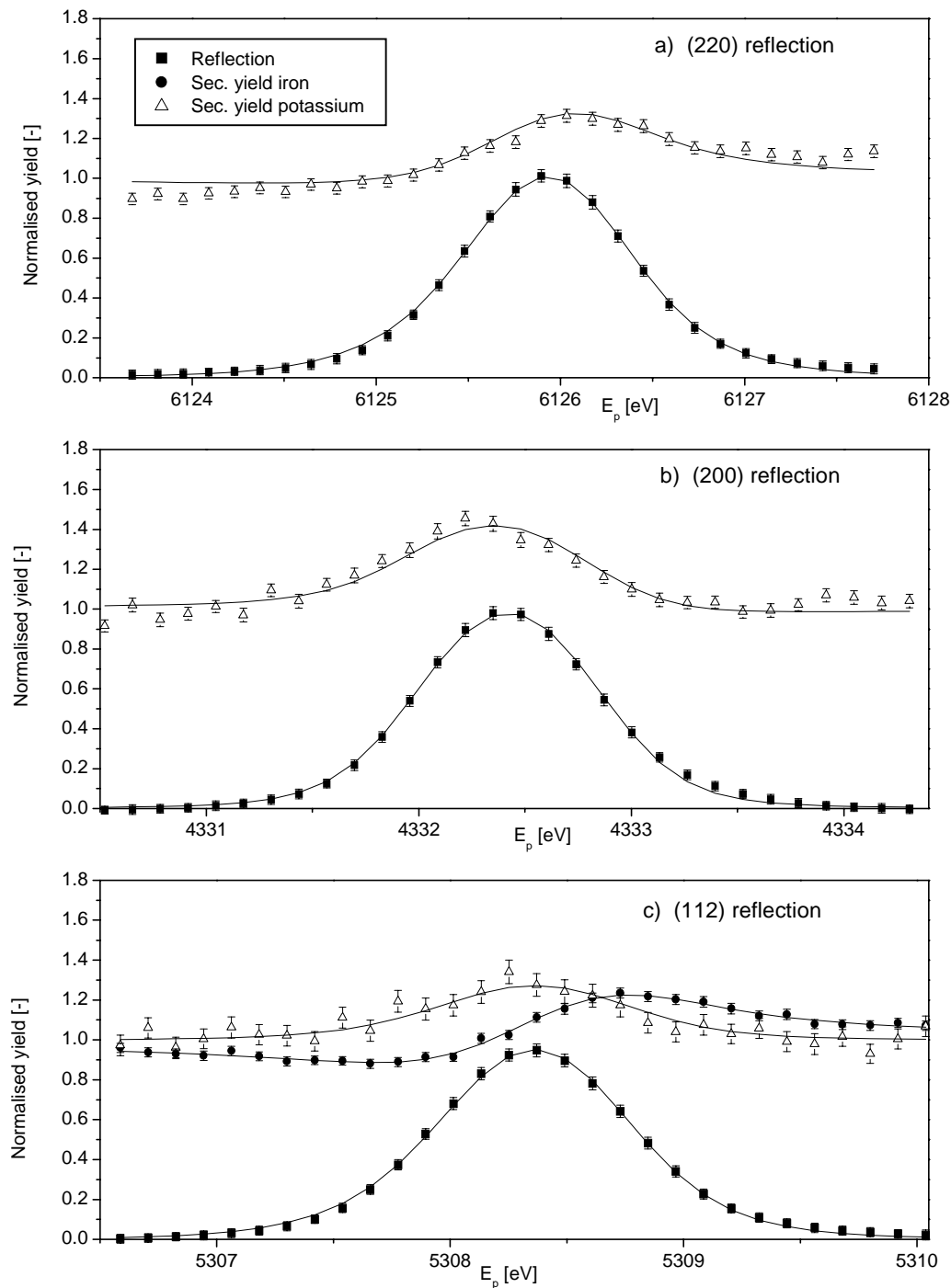
Figure 3.4: *The rocking curve (solid squares) and the K fluorescence yield (open triangles) as a function of the incident photon energy for the a) (220) Bragg reflection b) (200) Bragg reflection and c) (112) Bragg reflection. In c) the Fe fluorescence yield is also plotted (solid circles).*

The variation of the iron and potassium secondary fluorescence yield (Y) as a function of the energy (E) and the angle (θ) between the incident X-Ray wave vector and the lattice plane can be expressed in terms of the reflectivity (R_H), coherent fraction (f_c) and coherent position (φ_c) [27]:

$$Y \propto 1 + R_H(E,\theta) + 2\sqrt{R_H(E,\theta)} \, f_c \, \cos\left[v(E,\theta) - 2\pi\varphi_c\right] \quad, \tag{27}$$

here φ_c and f_c denote the phase and amplitude of the (hkl) component of the corresponding atomic distribution.

$$\varphi_c = \frac{1}{2\pi} arg\left\{ \sum_{i=1}^{N} e^{2\pi i \vec{H}_{hkl} \cdot \vec{r}_i} \right\} \tag{28}$$

$$f_c = \frac{1}{N}\left| \sum_{i=1}^{N} e^{2\pi i \vec{H}_{hkl} \cdot \vec{r}_i} \right| \tag{29}$$

For the atoms of a bcc substrate, the sum in the equations (28) and (29) yield $f_c = 1.0$ and $\varphi_c = 1.0$ for all allowed Bragg reflections. As can be seen from table 3.2, we find agreement between the expected value of $\varphi_c = 1.0$ for the iron and the measured value of $\varphi_c = 0.97$ almost within the statistical error bars. The remaining difference can be explained by surface defects of the Fe substrate which may also be responsible for a reduced coherent fraction of the iron, exceeding the reduction of this value as expected from thermal vibrations.

The coherent fraction as a function of the temperature can be estimated by calculating the mean square displacement $<u^2>$ of the iron atoms (atomic mass m) from their bulk position due to thermal vibrations. For $T \gg \theta_D/6$, with $\theta_D=470$ K the Debye temperature [25, 39]:

$$<u^2> = \frac{145.54 \; T}{m \; \theta_D^2} \tag{30}$$

This yields a mean amplitude of 0.06 Å for the vibration of the iron atoms at room temperature, resulting in a decrease of the expected coherent fraction from $f_c = 1.0$ to $f_c = 0.95$ for a perfect Fe(110) crystal in the (112) Bragg reflection, which is significantly larger than the values obtained in this work which average at $f_c = 0.83 \pm 0.03$. Although the degree of crystal imperfection seems rather large, it is not exceptional [25, 30].

For adsorbates, a high coherent fraction ($f_c \approx 1$) indicates that virtually all atoms of a certain element are adsorbed in equivalent sites. A low coherent fraction ($f_c \approx 0$) is an indication for either random adsorption or adsorption in well defined but different and mutual cancelling

sites. Contributions of two atoms, located at $\vec{r}_1$ and $\vec{r}_2$, completely cancel out if the projections of the atom sites onto the scattering vector differ by half a diffraction plane spacing, i.e. $2\pi\ \vec{H}_{hkl}\cdot\left(\vec{r}_1-\vec{r}_2\right) = \pi\ (2n-1)$. Hence, a zero coherent fraction is found if cancelling sites are equally occupied. The XSW signal has a periodicity of one diffraction plane spacing. For single site adsorption, the distance (z) between the lattice planes and the adsorbate is equal to [25]:

$$z = (\varphi_c + m) * d_{hkl}\ , \tag{31}$$

here m is an integer and d_{hkl} is the diffraction plane spacing of the (hkl) reflection, according to table 3.1. Throughout this paper the coherent position is presented as an value between 0 and 1.0. The coherent fraction and the coherent position of the potassium and the iron for the different Bragg reflections under investigation, as determined by fitting the secondary yield shown in figure 3.4a-c, are summarized in table 3.2. The presented values are the averaged results over the number of data sets as given in the same table. The number between parentheses shows the number of data sets of these that have been obtained at an energy resolution of $\Delta E=1.5$ eV. The quoted accuracy in table 3.2 is based on the differences between the subsequent measurements. The accuracy between parenthesis is the average value of the accuracy per measurement, as based on the goodness of fit of the fluorescence data.

Table 3.2: *Coherent fraction (f_c) and coherent position (φ_c) of potassium and iron for the (220), (200) and (112) Bragg reflection. The number between parenthesis in the number of data sets column represents the number of measurements that have been performed at an energy resolution of $\Delta E=1.5$ eV instead of $\Delta E=1.0$ eV. The number between parenthesis in the f_c and φ_c columns represents the average accuracy per measurement.*

reflection	element	# data sets	f_c (-)	φ_c (-)
(220)	K	4 (2)	0.58 ± 0.27 (0.08)	0.12 ± 0.02 (0.01)
(200)	K	6 (3)	0.18 ± 0.08 (0.04)	0.48 ± 0.04 (0.04)
(112)	K	6 (4)	0.09 ± 0.05 (0.05)	0.60 ± 0.40 (0.14)
(112)	Fe	6 (4)	0.83 ± 0.05 (0.05)	0.97 ± 0.01 (0.01)

3.5 Discussion

We will start the discussion with a determination of the Fe-K bond length and the corresponding potassium hard sphere radius at the Fe(110) surface. These numbers can be extracted from the results without employment of a specific adsorption model and will be used for a more detailed interpretation of the data later on.

From the XSW results, we can determine the vertical distance of the potassium with respect to the position of the surface Fe lattice plane in the absence of surface relaxations. From other systems it is known that the alkali induced surface relaxation is smaller than 10% ([3, 13, 40, 41]). We will include this value as an additional uncertainty of 0.1 Å into the evaluation. If we further do not consider any site specific adsorption model, an additional uncertainty of the

bond length arrises from the surface corrugation and the lateral registration of the potassium atoms with respect to the iron surface. Equation (31) is used to calculate the vertical distance z of the potassium atoms to the uppermost Fe layer from the coherent position φ_c in the (220) direction: $z = (m + 0.12)*d_{220}$, with m integer. The iron radius is 1.24 Å. Using a hard sphere model and assuming a potassium radius in the range from 1.53 Å to 2.13 Å (table 10 of [13]), the only possible value for m is m=3. The Fe-K bond length is thus 3.35 ± 0.22 Å, taken into account the sources of error mentioned above. This corresponds to a potassium hard sphere radius in the range of 1.89 Å to 2.33 Å.

In the following, LEED and XSW measurements will be combined to find the potassium adsorption sites on Fe(110) and to determine the Fe-K bond length more accurately. Single site adsorption in "simple" sites like the atop or the short/long bridge sites would lead to a rectangular LEED pattern and can thus be ruled out because of the observed hexagonal LEED pattern. Based on the observed LEED pattern we will start by assuming a perfect hexagonal potassium overlayer. Given the average domain size of 500x500 $Å^2$ of the clean Fe(110), there are at least 10^8 domains/mm^2 present at the surface. Therefore it is inadequate to regard a single potassium slab. Instead a large number of slabs have to be taken into account when either calculating the corresponding LEED pattern or the XSW data. There are two ways in which a perfect hexagonal potassium overlayer can be adsorbed at the surface. Either there will be a random distribution of the perfect hexagonal slabs over the surface, indicating a small interaction between the potassium and the iron substrate, or the potassium will be locked at certain sites of the iron substrate (which would, at least for the LEED and XSW results, be the same as dealing with only a single slab of potassium hexagons on the Fe substrate). Locking might be expected because of the double periodicity of the potassium with respect to the iron substrate in the [$\bar{1}10$] direction. In figure 3.1 we show the sites that we have considered for the locking of the potassium on the iron: they include the atop (a), short bridge (b), long bridge (c) and the three fold hollow (d1&d2). As far as XSW measurements are concerned, locking in the short bridge site is similar to potassium adsorption in the iron [001] "trenches". The above mentioned sites are presented in order of coordination, with the three fold hollow the highest coordinated site for the potassium. According to the Langmuir-Gurney model, the three fold hollow site would be favoured in the case of non directional (ionic) bonds [6]. However, note that in the case of perfect potassium hexagons only a part (about 10%) of the atoms would actually be present in a locking site because of the incommensurate relationship between the perfect potassium hexagons and the iron substrate in the [001] direction. For a configuration of a potassium overlayer with N atoms, with the ith atom positioned at $\vec{r}_i$, the coherent fraction f_c and coherent position φ_c for the (hkl) reflection can be calculated, using equation (28) and (29) [25]. The scattering vector, $\vec{H}_{hkl}$, is directed normal to the diffraction planes and has a length of $|\vec{H}_{hkl}| = 1/d_{hkl}$ with the diffraction plane distance d_{hkl} according to table 3.1.

For the following discussion, we first consider domains with a perfect hexagonal superstructure that are locked at specific sites. An incommensurate relationship exists between the K and the Fe in the [001] direction. Therefore, a coherent fraction close to zero is expected for the measurement using the (112) Bragg reflection. The (200) in-plane information is
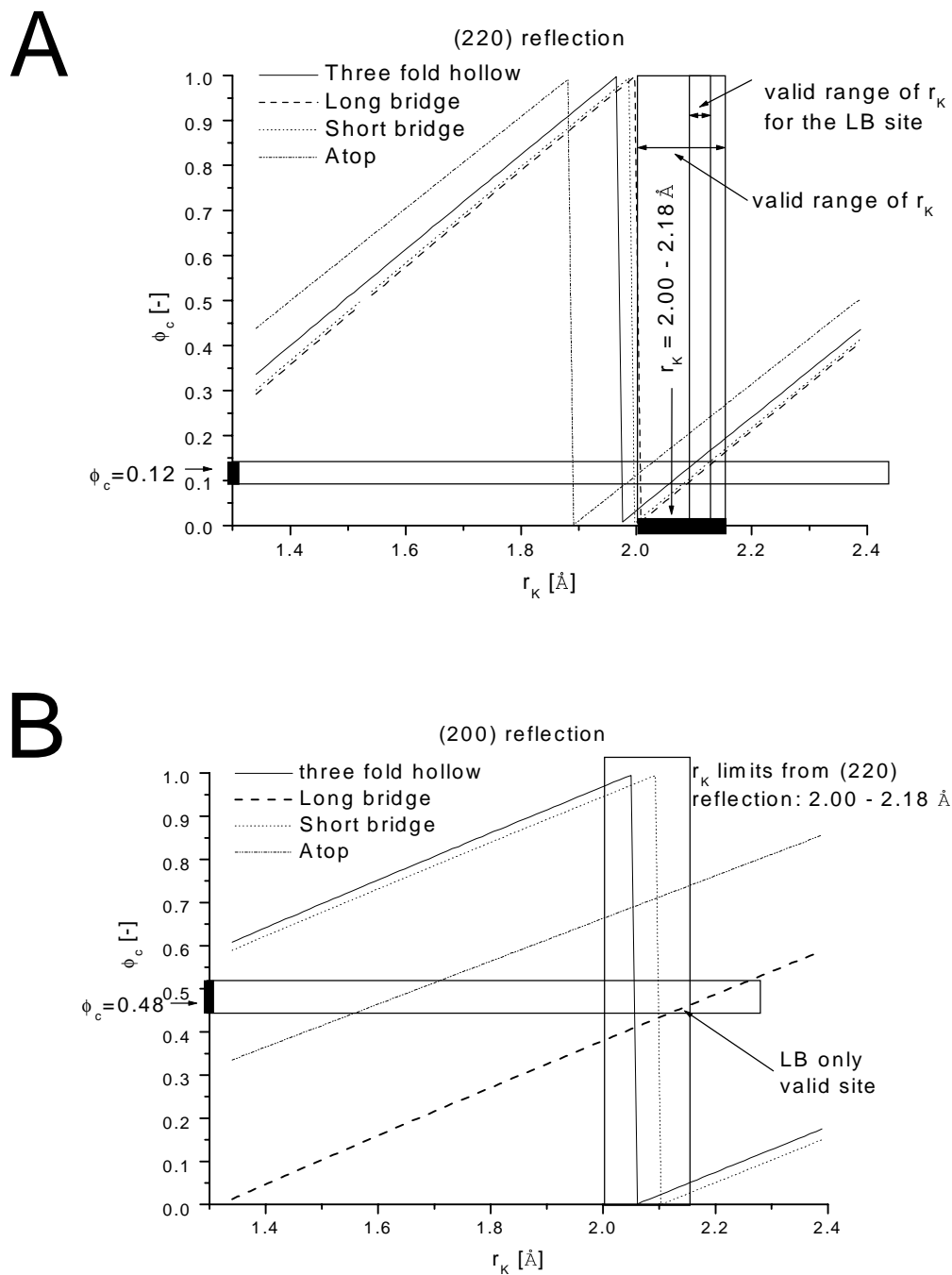
Figure 3.5: *The coherent position versus the hard sphere potassium radius for the four preferential adsorption sites considered in the a) (220) and b) (200) Bragg reflection. The allowed radii, as based on the measured coherent position of the (220) and (200) reflection, are indicated by the solid rectangles.*

perpendicular to the (112) in-plane information. If domains of hexagonal structure are locked at atop sites, then all atoms within such a domain will be found on the top of lines running in the (001) direction, passing through the atop sites. Due to the size ratio of K and Fe, the corrugation of the K overlayer is small. Employing a hard sphere model, the K atoms all have about the same distance to the surface (220) plane. For a Fe-K bond length of 3.35 Å, as determined above, this distance varies by ±0.16 Å only. Therefore high coherent fractions near unity are expected in the (220) and (200) Bragg reflection (e.g., according to equation (29), f_c = 0.84 in the (220) direction). The same holds for locking of domains of hexagonal structure at the short bridge and the long ridge position respectively. With respect to the (220) diffraction planes there are two different positions for the three-fold hollow site. The projections of these sites (d1&d2) on the (200) direction are half a diffraction plane spacing apart, resulting in a phase shift of 0.5π for domains locked at d1 with respect to those locked at d2. Based on symmetry we can rule out preferential adsorption at either the d1 or d2 sites. Hence for the cases of locking at the atop, short bridge and long bridge site, one expect a coherent fraction close to unity. For locking at the two different three-fold hollow sites a zero coherent fraction must be expected in the (200) Bragg reflection. The XSW results, however, yielded a coherent fraction of f_c = 0.18 ± 0.08 for the potassium in the (200) reflection. We therefore conclude that a locked perfect hexagonal overlayer is not the correct model for K adsorption on Fe(110). Also it is obvious that a random distribution of perfect hexagons will yield a coherent fraction of zero for both the (112) and the (200) reflection. The XSW results of the (200) reflection can thus not be explained by random adsorption of perfect potassium hexagons either.

Therefore we now consider the K atoms to occupy positions in a deformed hexagonal overlayer to explain the XSW and LEED results. In a simulation a large number (400 or more) domains of perfect hexagonal structure are randomly dispersed over the surface. This number has been chosen such that the coherent fraction for a random dispersion would yield a coherent fraction of less than 0.01 for the (112) and the (200) reflection. The simulation has been performed for the four symmetry sites considered above. In each simulation, the potassium atoms were allowed to move towards the preferred adsorption site. The maximum displacement for the potassium atoms is based on the average K-K distance (4.68 Å) as determined from the LEED measurements and the potassium in-plane radius. In the simulations the maximum displacement has been varied between d_{max} = 0.10 Å and d_{max} = 0.25 Å with steric hindering (K-K interaction) being the origin of the upper limit. The distance normal to the surface ("height") is calculated assuming a hard sphere radius for the potassium and the iron. In the simulations the surface iron atoms are fixed at the corresponding truncated bulk positions. Finally, the coherent fraction and position for this configuration are calculated according to equation (28) and (29). In figure 3.5a and figure 3.5b the calculated coherent position is plotted for the (220) and the (200) reflection versus the potassium hard sphere radius. Figure 3.5a again shows that the Fe-K bond length can be estimated from the (220) Bragg reflection results, even without further knowledge of the preferential adsorption site. This is due to the fact that the potassium radius is large compared to the in-plane Fe-Fe distance. Given the iron radius of 1.24 Å, the measured coherent position is in agreement with the model of a distorted hexagonal overlayer locked to any of the considered adsorption sites if the K hard sphere radius is 2.1 ± 0.2 Å (including the additional uncertainty

of ± 0.1 Å due to the possible surface relaxation of the iron substrate). This is in agreement with the value obtained in our initial discussion without the use of any site specific adsorption model.

The results of the (220) Bragg reflection define the limits on the potassium hard sphere radius. Between these limits the calculated coherent position and fraction, as drawn in figure 3.5b have to be equal to the measured coherent position and fraction as presented in table 3.2. The measured coherent position of the potassium in the (200) Bragg reflection is $\varphi_c = 0.48$. The limits for the potassium radius are drawn in figure 3.5b. It is clear that the long bridge site is the only candidate which has a coherent position of $\varphi_c = 0.48$ for the (200) Bragg reflection within these constraints. This in turn enables a more accurate determination of the K-Fe bond length and the calculation of the expected coherent position and fraction for all three XSW reflections. The corresponding potassium hard sphere radius is $r_K = 2.12 \pm 0.14$ Å. Here the accuracy is limited by the introduced uncertainty based on possible substrate relaxation.

The calculated coherent fractions and positions, in case of a deformed hexagonal potassium overlayer on Fe(110) with the long bridge site as preferential adsorption site, are compared to the measured coherent fractions and positions in table 3.3. The calculated coherent positions for the three reflections are in good agreement with the measured values. The ratio of the calculated and measured coherent fraction also shows good agreement for the (220) and the (200) reflection. From this ratio it is estimated that 70% of the surface is well ordered. This is near the expected maximum of 80% as the measured coherent fraction of the iron substrate itself is $f_c = 0.83 \pm 0.05$ in the (112) reflection. The smaller measured coherent fraction with respect to the calculated coherent fraction of the thee reflections might also be the result of initial contamination since oxygen adsorption will result in a larger potassium radius and also a different structure. A possible reason for the long bridge site as the preferential site, instead of the three fold hollow, are the contributions of the two next nearest neighbours to the coordination of the adsorbed potassium. In the case of adsorption in the three fold hollow site the potassium would bond to the three nearest iron atoms. However, in case of adsorption in the long bridge site the

Table 3.3: *Comparison between the coherent position and coherent fraction for the potassium as measured in the (220), (200) and (112) Bragg reflection and as calculated with the long bridge as preferential adsorption site, $d_{max} = 0.2$ Å and $r_K = 2.12$ Å.*

Reflection		measurements (-)	calculation (-)
(220)	coherent fraction	0.58 ± 0.27	0.82
(220)	coherent position	0.12 ± 0.02	0.12
(200)	coherent fraction	0.18 ± 0.08	0.28
(200)	coherent position	0.48 ± 0.04	0.47
(112)	coherent fraction	0.09 ± 0.05	0.19
(112)	coherent position	0.6 ± 0.4	0.49
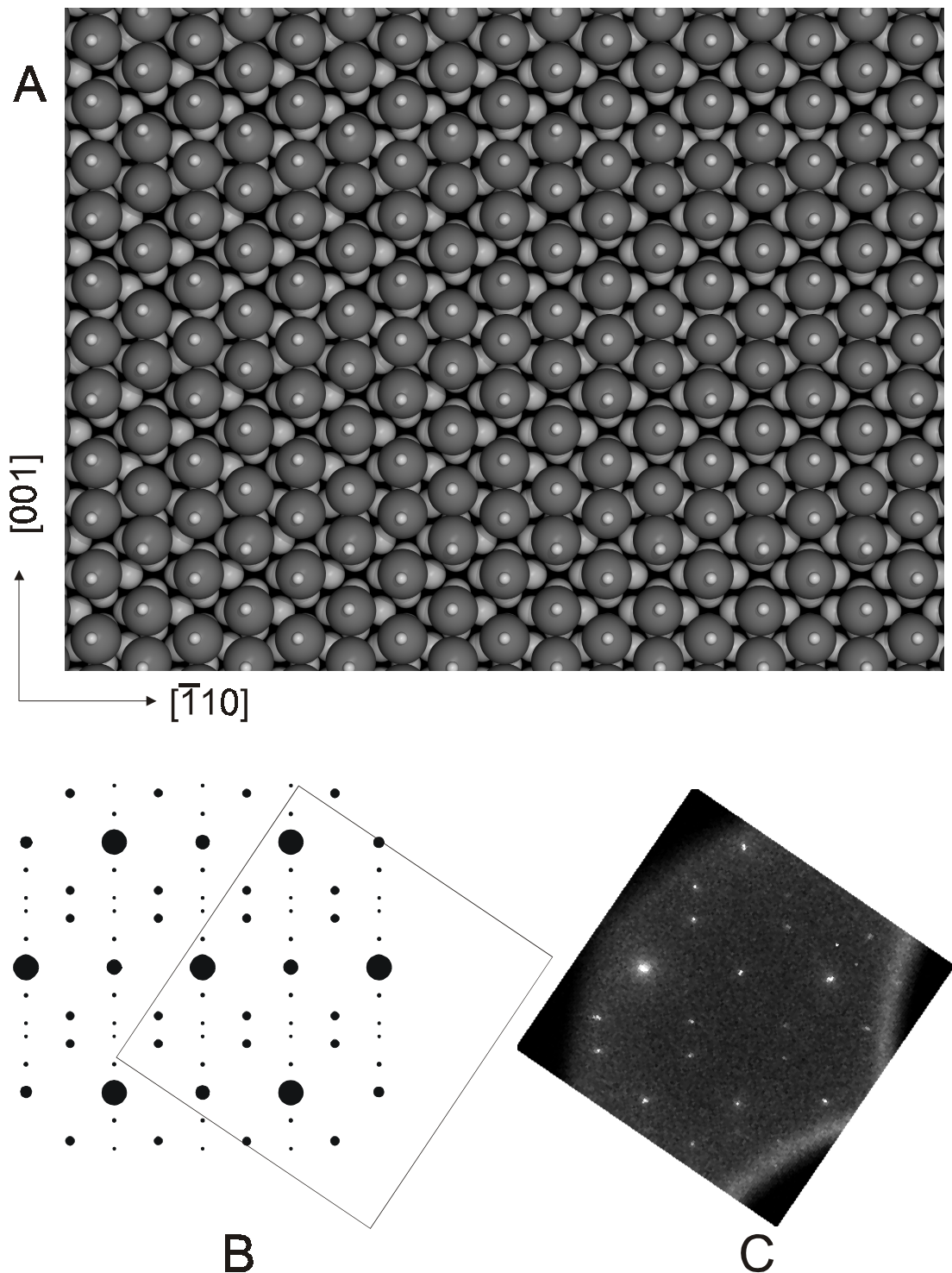
Figure 3.6: *a) The real space model of the deformed hexagons with the long bridge site as preferential adsorption site and a maximum allowed movement of the potassium atoms of $d_{max} = 0.2$ Å. The original K sites (perfect hexagons) are indicated by the white dots, the iron substrate by the light spheres and the potassium atoms by the dark spheres. b) The calculated LEED pattern that corresponds to the above real space model. c) The measured LEED pattern, which has been rotated with respect to figure 3.3c to enable an easy comparison with b).*

next nearest iron atoms are only slight further away than the closest iron atoms (3.65 Å versus 3.36 Å, a difference of only 9%) which could effectively lead to a higher effective coordination than for the three fold hollow.

With the real space configuration of the potassium given (see figure 3.6a), it is possible to calculate the LEED pattern in the kinetic approximation. We have performed this calculation for 100 randomly dispersed slabs of 1200 atoms and a 1500x1500 "LEED" grid. For each point on the grid the "intensity" was calculated from the phase-differences, after which the intensity was summed per spot. Although this approach is valuable in selecting the main diffraction spots, the calculated spot intensity must be expected to differ from the measured one due to the limitations of the kinematic approximation, e.g. not taking into account multiple scattering effects. The most important result of this calculation is that the position of the calculated LEED spots is identical to the position of the measured LEED spots, including those which have been attributed to multiple scattering [20]. In the kinetic approximation there is no intensity difference between the superstructure spots (marked as "b" and "c" in figure 3.3b). The calculated LEED pattern is shown in figure 3.6b, here the intensity within a certain area is indicated by the size of the spot. The measured LEED pattern is shown for reference in figure 3.6c. Figure 3.6c has been rotated with respect to the corresponding LEED pattern of figure 3.3c to enable easy comparison with the calculated LEED pattern.

3.6 Conclusions

For potassium on Fe(110) a Fe-K bond length of 3.35 ± 0.22 Å was found from the XSW results. This value corresponds to a potassium hard sphere radius of 2.11 ± 0.22 Å. The determination of this radius, at least with the above mentioned accuracy, does not involve knowledge on the in-plane position of the potassium.

Based on the XSW and LEED results we propose a model for the potassium adsorption in a deformed hexagonal structure with the long bridge site as the preferred adsorption site. Calculations based on the kinematic approximation have shown that such a model can explain the measured LEED pattern including the intensity ratios of the various superstructure spots as opposed to the suggested multiple scattering explanation [20]. Furthermore, simulations based on this simple approach result in good quantitative agreement with XSW data obtained in the (220), the (200) and the (122) Bragg reflection. For a further improvement in the interpretation of the data, a detailed knowledge of the surface and interaction potential for atomic displacements in this system is required.

Alkalis in general favour the highest coordinated site for adsorption, which is the three fold hollow site in the case of Fe(110). However, the long bridge may be favoured over the three fold hollow site because the combination of two nearest iron atoms and two next nearest iron atoms (K-Fe bond length difference for nearest and next nearest iron atoms is only 9 %) could effectively cause a higher coordinated adsorption site than the three fold hollow with only three nearest iron atoms (K-Fe bond length difference for nearest and next nearest iron atoms is 57 %).

Assuming the real space model is correct, and the Fe atoms at the surface are located at unrelaxed bulk positions, it is possible to calculate the Fe-K bond length with more precision to 3.36 ± 0.14 Å. With a iron radius of $r_{Fe} = 1.24$ Å, the corresponding hard sphere radius of the potassium is 2.12 ± 0.14 Å. The main contribution on the accuracy in the presented number (± 0.10 Å) is based on the (maximum) reported relaxations of metal substrates after alkali adsorption. The radius of adsorbed potassium on metal substrates tends to increase with increasing coverage and increasing coordination (figure 33 and table 10 of [13]). The coverage and coordination of potassium after saturation adsorption on Fe(110) are both large compared to the reported coverage and coordination of potassium on various other metal substrates. This may explain why the found potassium radius of 2.12 ± 0.14 Å is among the largest reported.

References:

1. R.O. Jenkins, Vaccum 19 (1984) 353

2. L. J. Whitman, C.E. Bartosh, W. Ho, J. Chem. Phys. 85 (1986) 3688

3. D. R. Strongin, G.A. Somorjai, Journal of Catalysis 118 (1989) 99

4. H.P. Bonzel, A.M Bradshaw, G. Ertl, Physics and chemistry of alkali metal adsorption, (1989) Elsevier Science publishers B.V., The Netherlands, ISBN 0-444-88338

5. S.Å. Lindgren, L. Walldén, J. Rundgren, P. Westrin, J. Neve, Phys. Rev. B 28 (1983) 6707

6. R.D. Diehl, R. McGrath, J. Phys. Condensed Matter 9 (1997) 951

7. H. Ishida, K. Terakura, Phys. Rev. B 36 (1987) 4510

8. H.Ishida, K. Terakura, Phys. Rev. B 38 (1988) 5752

9. A. Schmalz, S. Aminpirooz, L. Becker, J. Neugebauer, M. Scheffler, Phys. Rev. Letters 67 (1991) 2163

10. G.S. Leatherman, R.D. Diehl, P. Kaukasoina, M. Lindroos, Phys. Rev. B 53 (1996) 10254

11. D.L. Adler, I.R. Collins, X. Liang, S.J. Murray, G.S. Leatherman, K.D. Tsuei, E.E. Chaban, S. Chandavarkar, R. McGrath, R.D. Diehl, P.H. Citrin, Phys. Rev. B 48 (1993) 17445

12. C. Stampfl, J. Burchhardt, M. Nielsen, D.L. Adams, M. Scheffler, H. Over, W. Moritz, Surf. Sci. 287/288 (1993) 418

13. R.D. Diehl, R. McGrath, Surface Science Reports 23 (1996) 43

14. G. Ertl, S.B. Lee, M. Weiss, Surf. Sci. 114 (1982) 527

15. W. Arabczyk, U. Narkiewicz, K. Kalucki, Vacuum 45 (1994) 267

16. L. Zhu, S. Bao, C.Y. Xu, Y.B. Xu, Surf. Sci. 260 (1992) 267

17. J. Paul, Surf. Sci. 224 (1989) 348

18. S.D. Cameron, D.J. Dwyer, Surf. Sci. 198 (1988) 315

19. S.B. Lee, M. Weiss, G. Ertl, Surf. Sci. 108 (1981) 357

20. G. Brodén, H.P. Bonzel, Surf. Sci. 84 (1979) 106

21. W. Arabczyk, U. Narkiewicz, K. Kalucki, E. Freidenburg, Appl. Surf. Sci. 72 (1993) 45

22. A.G. Fedorus, A.G. Naumovets, Surf. Sci. 21 (1970) 426

23. U. Scheithauer, G. Meyer, M. Henzler, Surf. Sci. 178 (1986) 441

24. M. Henzler, Surf. Sci. 152/153 (1985) 963

25. J. Zegenhagen, G. Materlik, W. Uelhoff, Journal of X-Ray Sci. and Tech. 2 (1990) 214

26. D.P. Woodruff, D.L. Seymour, S.F. McConville, C.E. Riley, M.D. Crapper, N.P. Prince, Surf. Sci. 195 (1988) 237

27. B. W. Batterman, H. Cole, Reviews of modern physics 36 (1964) 681

28. T. Ohta, H. Sekiyama, Y. Kitajima, H. Kuroda, T. Takahashi, S. Kikuta, Jap. Journal of Applied Physics 24 (1985) L475

29.   H. Hashizume, T. Nakahata, Jap. Journal of Applied Physics 27 (1988) L1568

30. D.P. Woodruff, D.L. Seymour, C.F. McConville, C.E. Riley, M.D. Crapper, N.P. Prince, Phys. Rev. Letters 58 (1987) 1460

31. R. Koper, Surface Preparation Laboratory, Penningweg 69F, 1507 DE Zaandam, The Netherlands

32. R. Frahm, J. Weigelt, G. Meyer, G. Materlick, Rev. Sci. Instr. 66 (1995) 1677

33. Structure and morphology of thin metallic overlayers, W. Ceelen, Eindhoven (1997), ISBN 90-386-0577-3

34. SAES Getters S.p.A., Via Gallarate 215, 20151 Milano, Italy

35. W.C.A.N. Ceelen, A.W. Denier van der Gon, J. Falta, A. Hille, G. Materlik, Surf. Sci. 391 (1997) 59

36. G. Pirug, G. Brodén, H.P. Bonzel, Surf. Sci. 94 (1980) 323

37. M. Henzler, Surf. Sci. 22 (1970) 12

38. M.A. Van Hove, W.H. Weinberg, C.M. Han, Low Energy Electron Diffraction (1986) Springer-Verlag Berlin, ISBN 3-540-16262-3

39. X-Ray standing wave analysis for bromine chemisorbed on silicon, M. J. Bedzyk, New York, 1982

40. Surface crystallographic information service, J.M. McLaren, J.B. Pendry, P.J. Rous, D.K. Saldin, G.A. Somorjai, M. A. van Hove, D.D. Vvedensky, D. Reidel publishing company, Dordrecht (1987), ISBN 90-277-2503-9

41. U. Starke, M.A. van Hove, G.A. Somorjai, Progress in Surf. Sci. 46 (1994) 305

Temperature dependent step-edge composition of $Pt_{25}Rh_{75}(410)$

4

4.1 Abstract

We demonstrate that low energy ion scattering can be used to study the step-edge composition on vicinal single crystal surfaces. Employing the shadowing and focussing effects inherent to ion scattering, it is possible to perform site-specific composition measurements on single crystal surfaces over a wide temperature range. By combining these measurements with ion trajectory simulations we have extracted quantitative information concerning the step-edge composition. This technique has been applied to the $Pt_{25}Rh_{75}(410)$ surface at room temperature and in the temperature range between 400°C and 700°C. The experiments reveal a much stronger Pt enrichment of the step-edges than at the terrace sites. The difference between the step edge composition and the terrace site composition is significantly larger than predicted by simple segregation models based on bond-breaking. There is good agreement between the calculated surface and step-edge composition if a coordination dependent bond energy is applied.

4.2 Introduction and method

Vicinal surfaces of metal single crystals can display a distinctly different behaviour compared to their "flat" counterparts. Among the properties influenced by steps and other surface defects are adsorption [1, 2, 3], reactivity [4], catalytic activity [5] and the work function of the surface [6]. For stepped surfaces of alloys an additional complication arises due to the fact that the step-edge composition of an alloy will in general differ from both the average surface composition and the bulk composition as a result of the lower coordination of the step-edge atoms. In order to understand the differences in properties between flat and stepped alloy surfaces, it is therefore necessary to know the composition of the surface and the step-edges. A comparative study of the bulk composition, the average surface and the step-edge composition also gives more insight into the fundamentals of segregation itself.

Until now, few experimental studies on the step-edge composition of bimetallic alloys have been reported. This is because most surface science techniques are not suitable for site-selective quantitative composition measurements. Scanning Tunnelling Microscopy (STM) is one of the few techniques which is able to get site-selective quantitative information. STM has been used to show that the step-edge of a $Pt_{50}Rh_{50}(100)$ surface consists almost exclusively of Pt [7]. However, besides the fact that an additional surface science technique is required to interpret the results, it also cannot be used at the high temperatures which are often needed to reach equilibrium. STM results are also hard to interpret if there are more than two species involved. Low energy ion scattering (LEIS) is capable of providing quantitative information on the composition and structure of surfaces [8, 9].

In previous segregation studies on alloys, LEIS was mostly used to determine the composition of the outermost layer, averaged over all sites present. Experiments where LEIS was used to measure the surface composition of PtRh samples have been presented by e.g. Varga et al. on $Pt_{25}Rh_{75}(100)$ and $Pt_{25}Rh_{75}(111)$ [10] and by Beck et al. on $Pt_{10}Rh_{90}(100)$ [11]. By exploiting the shadowing and focussing effects inherent in LEIS, the ion intensity may be focussed at specific sites in the surface, thereby restricting the backscattered signal to particles that have collided with atoms residing at this specific site exclusively. In principle, such methods have been used before with Time Of Flight (TOF) LEIS to extract layer by layer composition profiles [12]. In this paper we take this idea one step further by using focussing effects to distinguish step edge sites from terrace sites, which enables us to measure the temperature-dependent composition of step edges for the first time. The experiments were performed on a vicinal $Pt_{25}Rh_{75}(410)$ surface which was found to have double atomic height steps. A schematic picture of this surface is given in figure 4.1. We will use the term *step-edge* for the atoms that have six missing nearest neighbours (solid black atoms in figure 4.1). A *terrace-atom* is defined by three to five missing nearest neighbours (hatched atoms in figure 4.1). The latter definition has been chosen to include all surface atoms as either step-edge or terrace atoms, although most of the terrace atoms have four missing neighbours. The *surface-composition* therefore represents the average composition of all step-edge and terrace-atoms together.

Side view

Top view

● step-edge atom   ○ deeper layer atom

⊜ terrace site atom
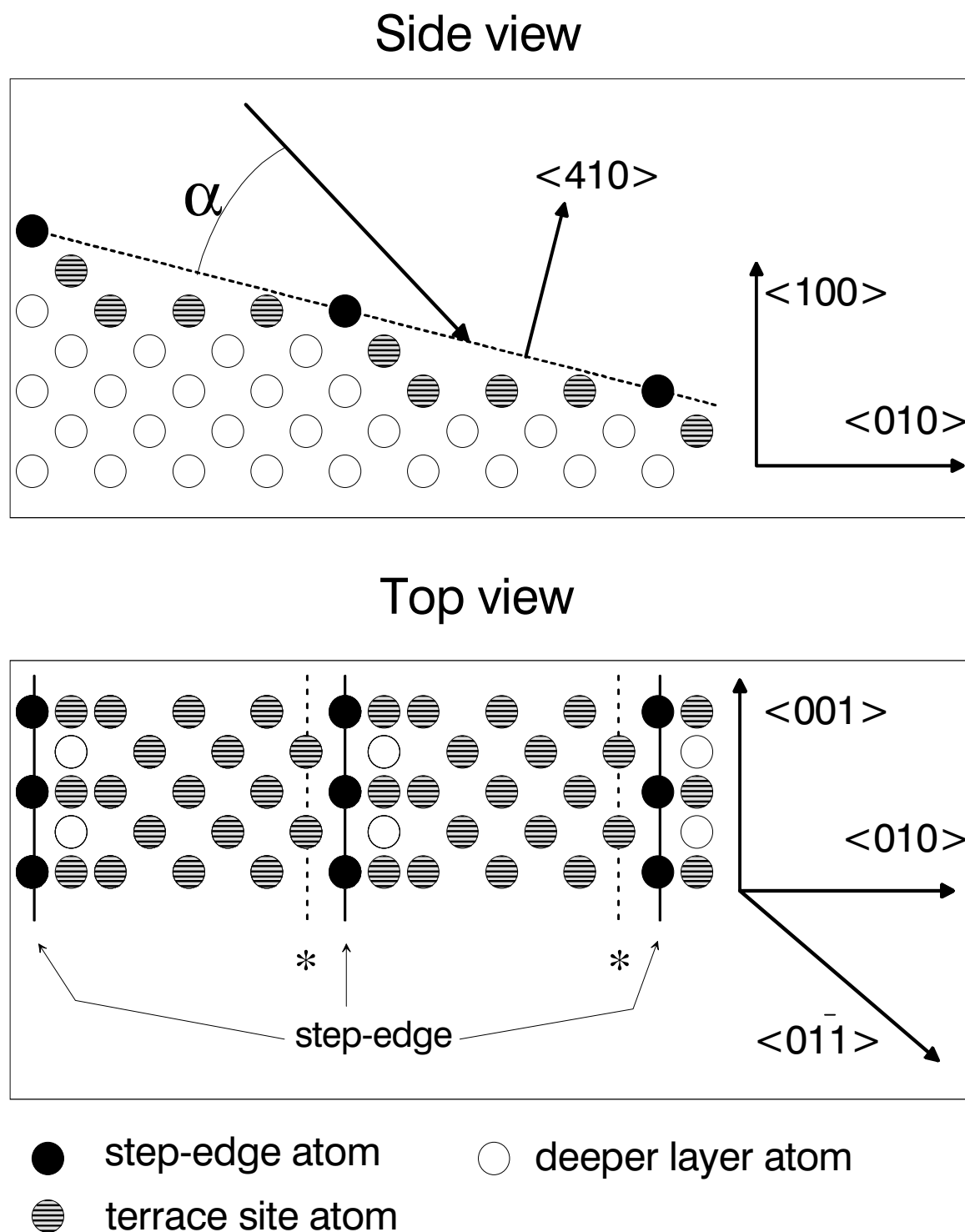
Figure 4.1: *Side and top view of the Pt$_{25}$Rh$_{75}$(410) crystal. The asterisks indicate atoms which display similar focussing behaviour as the step-edge atoms (see text).*

PtRh was selected because it is an interesting alloy for catalysis. Many automotive 3-way catalyst formulations are based on Pt and Rh and it has been found that alloy formation takes place during operation of the catalyst. In addition, the PtRh alloy is not chemically ordered and the low-index surfaces show incomplete segregation of Pt [13, 14]. This allows a stronger

segregation at the stepped surfaces, as has already been indicated by scanning tunnelling microscopy measurements performed at room temperature [7]. The (410) surface was selected because of its interesting catalytic properties [18, 19]. In particular, the (410) surface of pure Pt has been reported to exhibit an unusually high dissociation activity with respect to NO and CO [15, 16]. It was suggested that on the Pt(410) surface the NO dissociation reaction is symmetry allowed according to the Woodward-Hoffmann rules [15, 17]. The behaviour of the PtRh(410) surface with respect to adsorption and dissociation will be dependent on the step edge composition [18]. A clear comparison between various surfaces of Pt, Rh and PtRh, showing this dependence is presented in ref [19]. Therefore it is especially interesting to link the observed step-edge composition to the catalytic activity of the surface.

4.2.1 Method

In figure 4.2 we illustrate the principle of site-selective composition measurements of step-edges in the case of vicinal single crystal surfaces. In this figure we show two dimensional ion trajectory simulations on a (410) surface with double atomic height steps, at four different angles of incidence. Here we will focus on the use of TOF on this specific surface, in the conclusion section we will discuss the use of TOF for step-edge measurements on other surfaces. In figure 4.2a an extremely grazing angle of incidence is chosen. This causes the terrace atoms to be inside the shadow-cone of the step-edge atoms. This is a general occurring phenomena with glancing incident ion-beams, where a large number of small-angle deflections causes the surface to act like a mirror to the incoming ion beam. In the chosen (near 180 degree) backscattering geometry of our experiments this will results in a very low yield.

At the edge of the shadow-cone there is a region of increased ion density which can be focussed on the step-edge atoms by increasing the angle of incidence (figure 4.2b). Ions which backscatter in this geometry into the detector will originate from collisions with step edge atoms, resulting in a spectrum which effectively represents the mass spectrum of the step edge sites. Due to the focussing, the scattered yield is larger than for an unfocused beam. This ensures that a good signal may still be obtained, even when only a small fraction of atoms occupies the step-edge sites. In a graph of the backscattered yield as a function of the angle of incidence, this focussing event may be recognized as the first peak or shoulder in the observed intensity. Considering the size of the shadow cone and the distance between the step-edge atoms, it is expected that the atoms which are indicated by an asterisk in figure 4.1 will also contribute to the backscattered signal. The exact amount of this contribution was determined by ion scattering simulations, as will be discussed in section 4.

Upon increasing the angle of incidence further, the focussing on step-edge atoms disappears and ions may also scatter from atoms at terrace-sites. The next maximum in yield will thus occur when the step-edge atoms focus the ions on the subsequent atoms in the terrace (not shown in figure 4.2). The required angle of incidence is nearly equal to the angle of incidence which would lead to neighbour on neighbour focussing in the case of a low index PtRh crystal.
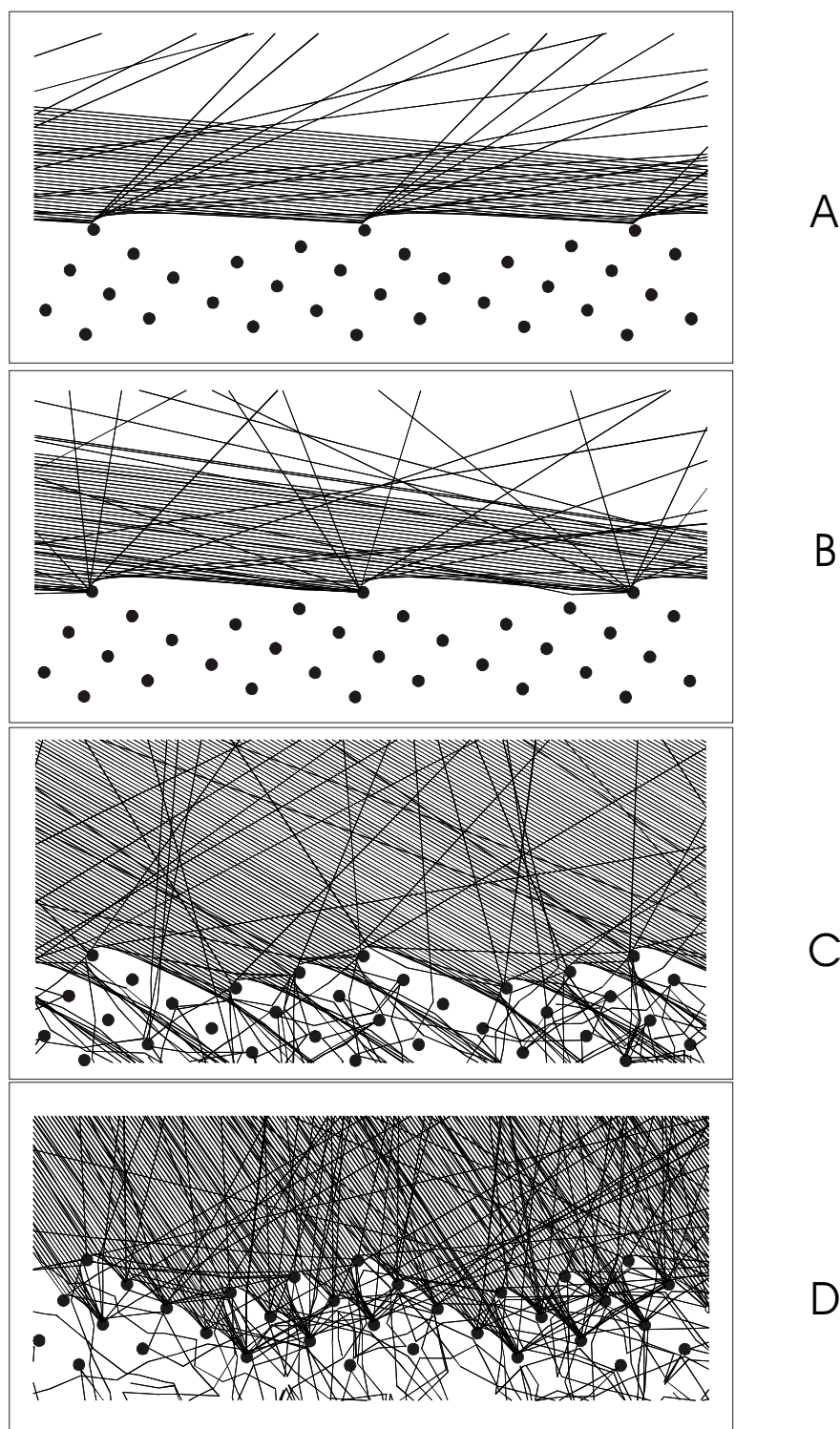
Figure 4.2: *Ion trajectory simulations at different angles of incidence illustrating the shadowing and focussing effects. (a)* α*=5°. No backscattering possible. (b)*α*=8°. Focussing on the step-edge atoms, all other atoms in the shadow cone. (c)* α*=30°. Probing the surface composition since all deeper layer atoms are in the shadow cone of the surface atoms. (d)* α*=50°. Unfocused yield from the surface atoms and focussing on the deeper layers. Main signal resulting from the second layer.*

The average surface composition of a (410) crystal can be measured at an angle of incidence of about 30 degrees (45 degrees minus the miscut angle with respect to the [100]), as shown in figure 4.1. Note that even in this geometry still not all terrace atoms are visible to the ion beam, as would have been the case in the step-up direction. However, the measured average surface composition in this geometry will be closer to the average surface composition as measured with an electrostatic analyser at normal incidence due to neutralization effects, which will be used for calibration purposes. Thus, from the dependence of the Pt and Rh backscattered signal on the angle of incidence, we may directly derive the composition of the step-edge sites and the terrace sites.

Increasing the angle of incidence even further, as shown in figure 4.2d, results to focussing of the ion-beam on the deeper layers. The yield in this situation is caused by a combination of unfocused scattering from the first layer and focussed scattering from the second and third atomic layer. The composition of the second layer can be roughly estimated if we assume that the third layer's composition will be close to the bulk composition and the second layer will be the major contributor to the signal. The latter assumption is based on the fact that blocking effects will become increasingly important for ions that return from deeper layers due to the lower average energy of the returning particles (larger blocking cone) and the larger number of blocking atoms.

For a quantitative interpretation, a calibration of the relative detection sensitivity for scattered Ne^+ ions from Pt and Rh is necessary. The difference in sensitivity is caused by the difference in cross-section for scattering from Pt and Rh and by the energy dependent detection efficiency of the channel plates in the TOF analyser. We have calibrated the sensitivity of the TOF by comparing the results with those obtained using an electrostatic analyser. This indirect calibration was chosen because the absolute signal in a TOF experiment is strongly dependent on the scattering geometry. This is not the case for the electrostatic analyser, which may thus be calibrated in a straightforward manner using Pt and Rh single crystal reference samples. In addition, the experiments with the electrostatic analyser directly yield the temperature dependent composition of the outermost layer.

4.3 Experimental

The present experiments were performed using a newly constructed (near) 180 degrees backscattering TOF setup. The primary ion beam is aimed at the sample through a hole in the centre of the detector which will accept particles with a total scattering angle between 177.0 and 179.5 degrees. One of the main advantages of near-180 degrees backscattering is that any site can be probed which is directly "visible" to the ion-beam [20]. The backscattering TOF detector is attached to the EARISS setup [21]. The EARISS (energy and angle resolved ion scattering spectrometer) consists of a 145 degrees backscattering LEIS setup with a special 2 dimensional electrostatic analyser/detector. Also attached are a 35 degrees TOF scattering and recoiling spectrometer (TOF-SARS) and a standard low energy electron diffraction (LEED) instrument. The setup is equipped with a separate ion-gun for sputter-cleaning.

The sample is placed in a manipulator which has six degrees of freedom for positioning the sample with respect to the ion beam and the detector. The sample can be heated both by radiation and by electron beam bombardment using a filament positioned behind the sample. The temperature of the sample is measured with a CHINO comet 1000 pyrometer with an absolute accuracy of ±50°C and a reproducibility within ±10°C. The lower limit of the temperature range is 400°C and therefore no measurements have been done between room temperature (RT) and 400°C.

The crystal was mounted on a Ti sample holder and covered at the edges by a Ti foil to screen the sides of the sample from the ion-beam at grazing angles of incidence. Initially the sample was cleaned by cycles of 2 keV Ar$^+$ sputtering at RT and flashing to 1050°C. After each cycle the surface quality was inspected with LEED and TOF-SARS in different azimuthal directions. The cleaning procedure was continued until the LEED showed sharp spots corresponding to an unreconstructed fcc(410) surface and a low diffuse background, indicating a well-ordered surface, and until the impurity related peaks in the TOF-SARS spectra were below the detection limit. Based on the large differential scattering cross-section for recoiling to an angle of 35 degrees of light elements like oxygen and carbon (12 Å^2/sr for carbon and 7 Å^2/sr for oxygen as compared to 0.7 Å^2/sr for scattering of Pt and Rh), the level of contaminants is estimated to be less than 0.01 ML.

The LEED pattern of the clean surface corresponds to a unreconstructed (410) surface, and from the energy dependence of the (0,0) spot width it was concluded that Pt$_{25}$Rh$_{75}$(410) has double-atomic height steps (see e.g. ref. [22] for interpretation of LEED measurements of stepped surfaces). In general, double height steps can be expected when the step-distance becomes very small. In the case of the pure Pt(410) surface, faceting occurs instead of the formation of double height steps, which was not observed for our PtRh(410) surface.

Prior to each measurement, the sample was cleaned. After flashing, the sample was held at the desired temperature to reach equilibrium. The time during which the sample was allowed to reach equilibrium ranged between 15 seconds for temperatures above 950°C to 45 minutes at room temperature. The backscattering TOF spectra were taken in the so-called step-down geometry with the projection of the primary ion-beam onto the surface along the [010] direction. The EARISS experiments are performed with the ion beam perpendicular to the surface, see e.g. ref [24] for details. The main axis of the crystal have been determined from the azimuthal dependent backscattered yield (see figure 4.3).The symmetry axis is clearly visible in figure 4.3, the step-edge is located perpendicular to it. The step-up direction corresponds to 270 degrees azimuth in figure 4.3. The small differences between the simulation and the measurement are mainly due to tilt of the sample with respect to the manipulator.
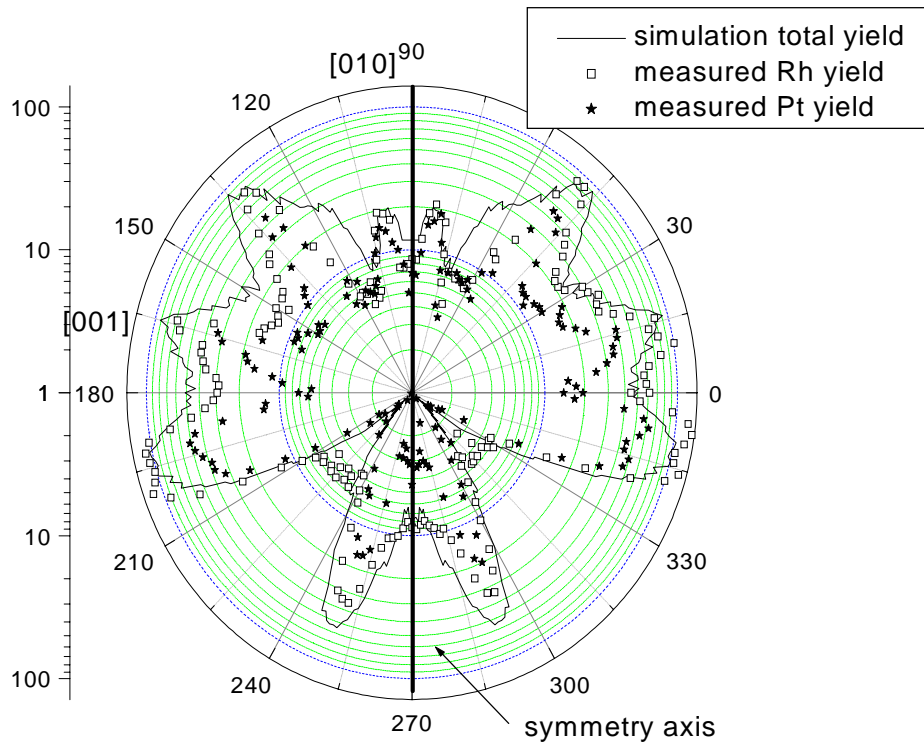
Figure 4.3: *Comparison of the measured and the simulated backscattered yield to determine the main axis of the Pt$_{25}$Rh$_{75}$(410) crystal.*

4.4 Segregation measurements

4.4.1 TOF experiments

The backscattering TOF spectra were taken with 4 keV Ne$^+$ which ensures a good mass-separation between Pt and Rh in combination with a high detector efficiency and a broad shadow-cone. The step-down geometry, which has been used during these measurements, is favourable in the case of Pt$_{25}$Rh$_{75}$(410). In the more general case of crystals with mono-atomic height steps or longer terraces, the step-up geometry would be favourable. The backscattered yield in the single-collision peak from Pt and Rh has been recorded as a function of angle of incidence at three different temperatures. Figure 4.4 shows the Pt (solid line) and Rh signals (dashed line) as a function of the angle of incidence at 400°C. The shoulder in the Pt and Rh signals at an angle of incidence of $\alpha = 8°$ (see also figure 4.2b) is caused by step-on-step focussing, and is consistent with the results from ion trajectory simulations using MATCH [23] which are shown in figure 4.5 and discussed in more detail below. The simulations have been performed for incident angles between 3° and 60°. The width of the detector has been accounted for in the simulations. The maximum at $\alpha = 18°$ is caused by focussing of the ions on the terrace atoms. Between $\alpha = 20°$ and

$\alpha = 40°$ there is an unfocused mode (see also figure 4.2c). Between these angles the average surface composition is probed since the atoms at the surface receive the same ion-flux. The next focussing occurs at an angle of incidence of $\alpha = 50°$ on atoms in the second and deeper layers(see also figure 4.2d). The squares in figure 4.4 represent the Pt over Rh signal ratio as observed experimentally. From this ratio (axis indicated on the right hand side of figure 4.4) we may directly obtain an indication of the composition of the various sites with respect to each other.
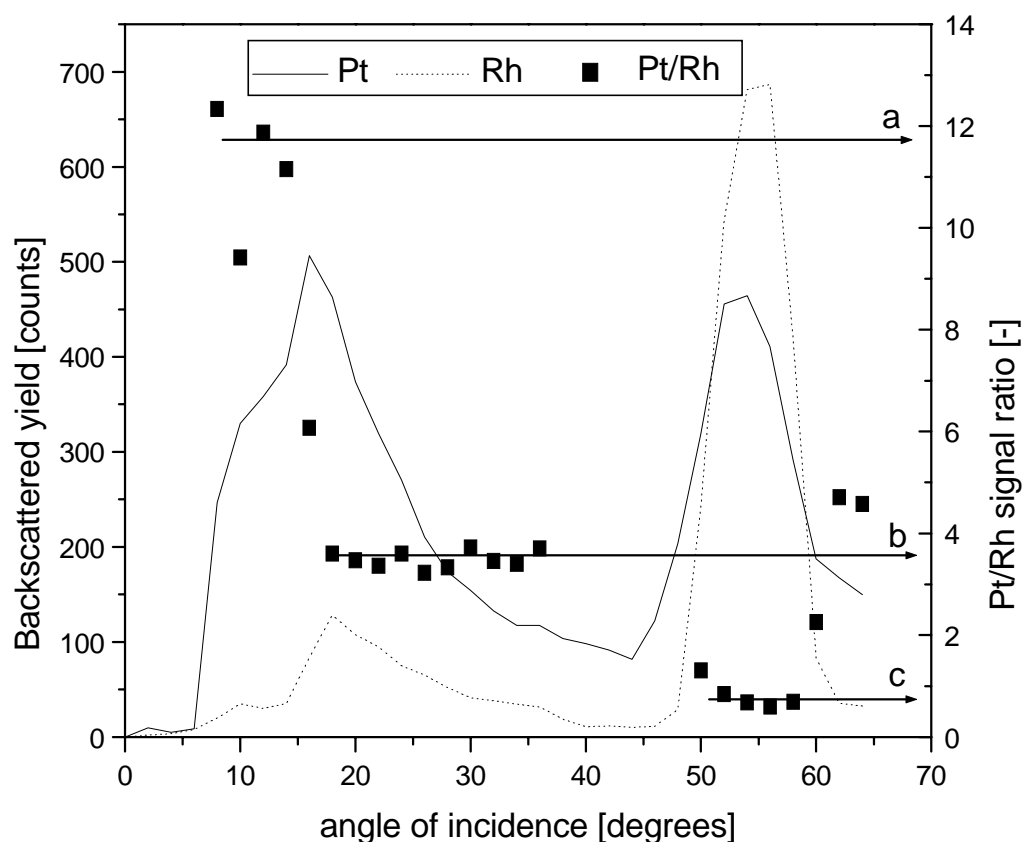
Figure 4.4: *The scattered yield from Pt and Rh, and the Pt over Rh signal ratio as a function of angle of incidence from backscattering TOF measurements at 400°C. The arrows indicate the Pt over Rh ratio for (a) the step-edge composition, (b) the average surface composition and (c) the composition of the second atomic layer.*

At grazing angles of incidence, where the step-edge composition is measured, the Pt over Rh ratio is much larger than between $\alpha=20°$ and $\alpha=40°$ where the surface composition is probed. This shows that the Pt concentration at the step-edges is significantly larger than on the terrace. The observed Pt/Rh ratio is much lower at $\alpha = 50°$ and so we can immediately conclude that the second layer is strongly depleted in Pt with respect to the surface. To obtain quantitative values for the composition at various sites, we calibrated the sensitivity for Pt with respect to Rh by

comparison of the average surface composition measurements with experiments using the EARISS analyser, see next section.
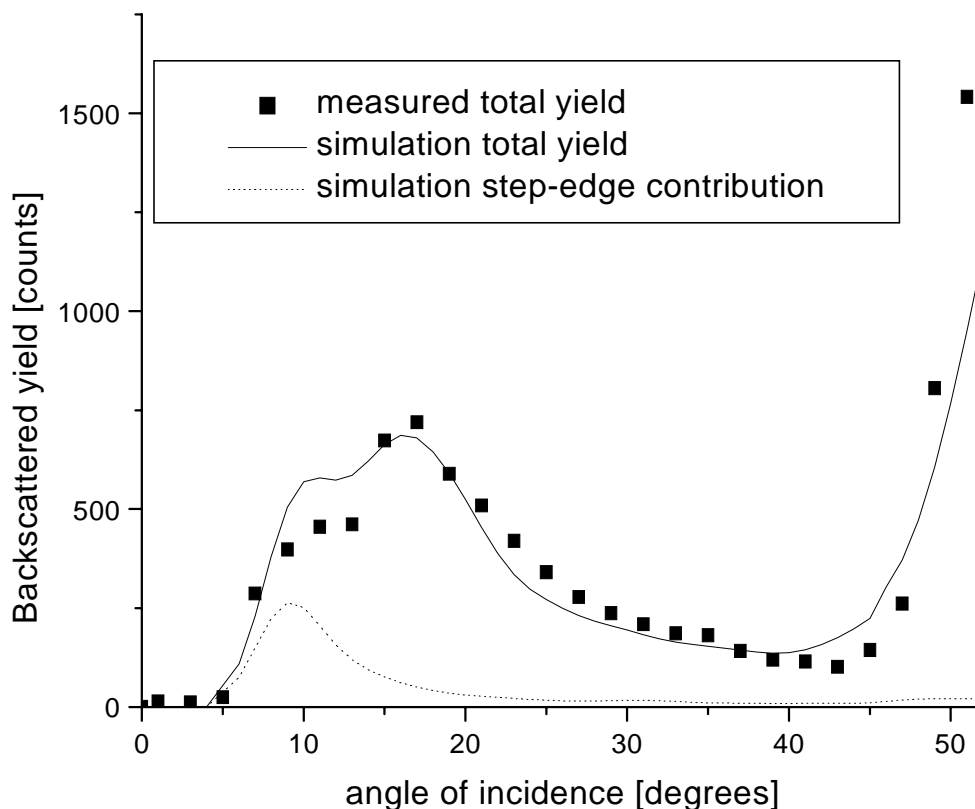
Figure 4.5: *A MATCH simulation of the total backscattered yield as a function of the angle of incidence using 4 keV Ne$^+$ on Pt$_{25}$Rh$_{75}$(410). The total yield is indicated by the solid line. The dashed line indicates which part is returning from the step-edge atoms.*

4.4.2 EARISS experiments

The surface composition has been measured as a function of the temperature with the EARISS using 3 keV Ne$^+$ ions. The ion dose was limited to less than 10^{12} ions/cm^2 per spectrum to minimize the radiation damage. The sensitivity factors for Pt and Rh for the EARISS were obtained by using clean and well-ordered Pt(111) and Rh(100) single crystals as reference samples. The ability of the EARISS to measure the azimuthal dependence of the scattered signal has been used to determine the contribution of the second atomic layer to the total yield. Discrimination between particles returning from the first and second atomic layer is possible since the first layer will yield an azimuthal independent contribution whereas the second layer yields an azimuth dependent signal [24]. From the measurement shown in figure 4.6, and method

described above, the contribution of the second layer was found to be only 4% of the total scattered yield. Because of this minor influence, the second layer contribution has been neglected for the interpretation of the EARISS measurements. The accuracy of an EARISS measurement is ±4% of which ±2% is due to the calibration accuracy.
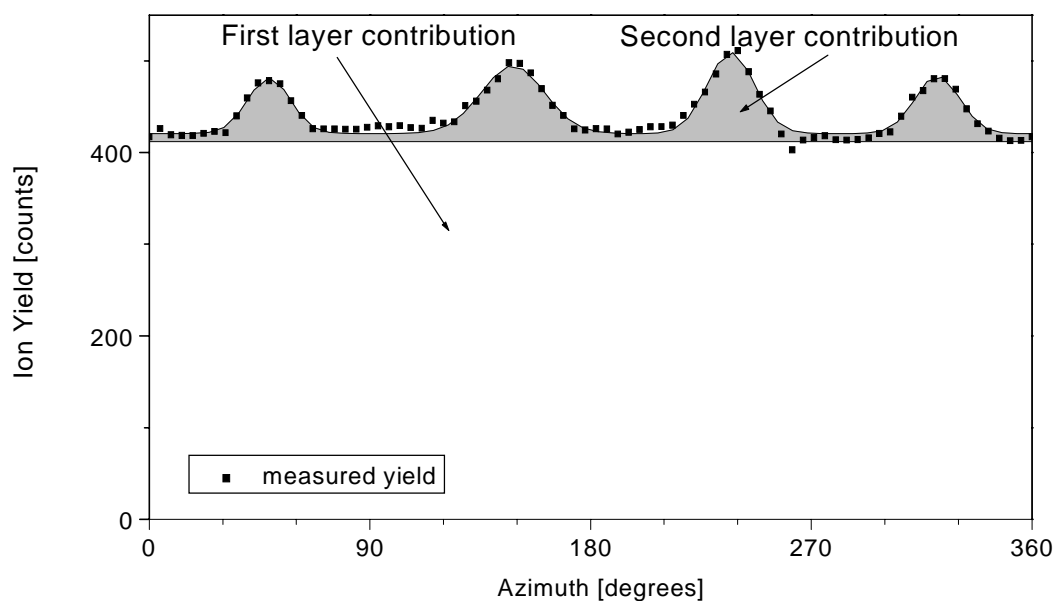
Figure 4.6: *EARISS measurement with 3 keV Ne$^+$ on Rh(100) showing the azimuthal dependent yield from which the second layer contribution can be determined. The second layer contribution is indicated by the grayed area.*

After sputtering at room temperature, the Pt$_{25}$Rh$_{75}$(410) surface composition is nearly equal to the bulk composition (27% Pt). In figure 4.7 the Pt surface concentration is plotted as a function of temperature. For these experiments the sample was kept at the chosen temperature during the measurement (after flashing and equilibration). The Pt enrichment decreases with increasing temperature, indicating that Pt has a lower surface energy than Rh over the chosen temperature range. The concentration measured at room temperature clearly does not correspond to an equilibrium situation, since a far larger Pt concentration would have been expected given the results between 400°C and 1000°C. Instead, the surface-state is "frozen" during cooling down to room temperature from 1050°C after the flash. This further illustrates the need to perform these kind of measurements at the equilibrium temperature and not to rely on quenching after equilibration. The measured Pt segregation to the surface is in agreement with the generally observed Pt enrichment of PtRh alloys [25, 26] and not with the Rh enrichment as observed on Pt$_{90}$Rh$_{10}$ by atom probe field ion microscopy [27]. As stated before [10], the observed Rh segregation in the latter experiment may be due to oxygen contamination on the surface which is known to reverse the segregation behaviour on PtRh [31]. Compared to the results from

Platzgummer et al. on a $Pt_{25}Rh_{75}(100)$ [10] we found a smaller Pt segregation to the surface (80% Pt versus 55% at 400°C, smaller differences al higher temperatures). This difference cannot be contributed to segregation inhibiting elements like carbon since the surface has been routinely checked and found to be contaminant-free with TOF-SARS after sputter-flash cycles, whereas the temperature during the measurements was kept at or below the flashing temperature. The difference in composition for the high temperature measurements can be explained by the accuracy of the composition and temperature measurements. The difference in composition at lower temperatures (400°C and below) is probably caused by kinetics. If the surface of the $Pt_{25}Rh_{75}(410)$ "freezes" at a temperature above of it's (100) counterpart, the final Pt concentration
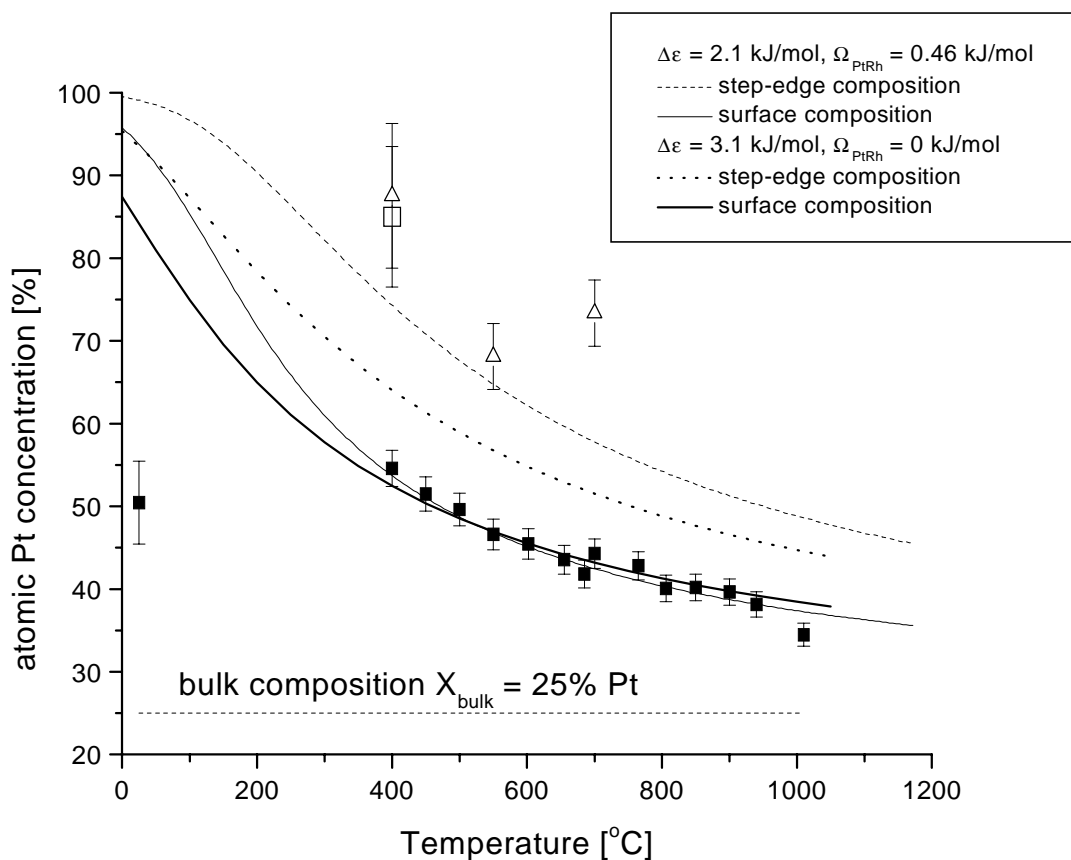
Figure 4.7: *The average surface composition (squares) as determined from the EARISS measurements and the step-edge composition as determined with TOF as a function of temperature in the step-down geometry (triangles) and the ion beam in the $[01\bar{1}]$ direction (open square). The solid curves shows the result of the fit of the average surface composition according to the broken bond model. The dotted/dashed curve represents the calculated composition of the step-edge sites according to the ideal/regular solution broken bond model as described in the text. The error bars on the first points show the accuracy including the calibration accuracy, the subsequent error bars show the accuracy without calibration accuracy.*

at the surface will be smaller. The results are within experimental accuracy if a difference of 100°C in this freezing temperature is assumed. Furthermore it is also possible that the bulk composition of the two samples is somewhat different. Due to the large segregation, this has a pronounced effect on the differences in the surface composition. For each percent difference of Pt in the bulk, the surface composition differs by 2.5%. Similar behaviour would be observed in the case of Pt depletion in the surface region due to the endured sputtering of our sample at elevated temperature. These above described effects might also explain the difference in the measured surface composition after sputtering between our experiments (27% Pt) and the surface composition after sputtering as found by Varga et al. [10] (35% Pt). Other causes can be the chosen sputter energy (2000 eV in our experiments versus 500 eV) and/or angle of incidence (20° versus 45°), as is the case for e.g. CuPd alloys where the surface composition after sputtering deviates stronger from the bulk values at lower sputter energies [28]. The results from Beck et al. [29], who measured 11% Pt after sputtering a Pt$_{10}$Rh$_{90}$(111) crystal, also seem to indicate insignificant preferential sputtering at higher primary energies. The experimentally found small deviation from the bulk-composition after sputtering is also in agreement with tabulated values for the Pt and Rh sputter-efficiency's of 1.4 versus 1.3 for 500 eV Ar$^+$ [30] and 1.56 versus 1.46 for 600 eV Ar$^+$ [31].

4.4.3 Step edge composition

The combination of the surface measurements with the EARISS and the backscattering TOF between an angle of incidence of 20° and 30° allows a calibration of the TOF results, since both techniques determine the composition at the same sites (figure 4.2 c). The accuracy of the EARISS measurements (±4%) is thus included in the calibration of the TOF, resulting in an accuracy of about ±10% in the determination of the step-edge composition. By comparing the TOF and EARISS results, the relative sensitivity factors for Pt and Rh have been calculated and used to quantify the results of the step-edge measurements. The 2.2 times higher sensitivity for Pt with respect to Rh is close to the expected value of 2.5 based on the larger scattering cross-section (1.7) and the larger detector-sensitivity caused by the higher final energy (1.5). The step-edge measurements were typically performed with an ion-beam current of 0.1 pA and a measurement time of 300 s, resulting in a maximum dose of 5*10^{11} ions/cm^2. No influence of radiation damage on the measurements is thus expected, even if every ion would selectively cause damage to a step-edge site.

From figure 4.2 it was already concluded that at small angles of incidence not only the step-edge atoms will contribute to the backscattered yield, but also the atoms in between (indicated by the arrow and asterisk in figure 4.1). Ion trajectory simulations with the computer code MATCH [23, 37] were performed to determine the ratio between the terrace and the step-edge yield. MATCH calculates three dimensional trajectories for ions that start with the primary energy at the ion source, for which the energy decreases with subsequent collisions, and for ions that start with the desired final energy at the detector for which the energy increases after each collision. The ion-atom interaction is treated in the binary collision approximation (BCA: subsequent collisions are treated as two body events) with a screened Coulomb potential

(Ziegler/Biersack/Wittmark). The program ties the sets of saved trajectories together if they meet requirements regarding their crossing distance, impact-parameter, collision partner and energy. The chance of a calculated collision to occur is determined from the chance of finding an atom at the required collision site, based on it's thermal vibrations. Although the amplitude of the thermal vibrations at the surface will be probably larger than in the bulk, we have chosen a fixed amplitude of 0.1 Å for all atoms. The main effect of increasing the amplitude of the terrace/step atoms will be a change in ratio between the yield from the different sites. The composition information as extracted from these sites will not change, however. The main advantage over full three dimensional trajectory calculations is the larger efficiency, and thus shorter simulation time. The crystal surface for the simulations is build up from a slab with periodical boundary conditions in the lateral direction. The number of atoms in a slab cannot be chosen arbitrarily large due to computing limitations. Therefore there can be only a limited number of unit-cells present in a slab. The repeating unit cell of a stepped surface will be large which causes discrete values for the step-edge composition in the simulations. The chance that a certain type of atom is present at the step-edge can be chosen at will though.

For the $Pt_{25}Rh_{75}(410)$ surface we used a slab of 440 atoms, with 22 atoms in each unit cell. This means that the Pt concentration at the step-edge can be varied by a multiple of 5 % in our simulations. Averaging measurements to get arbitrary step-edge concentrations is feasible, but not necessary. It was assumed that the Pt concentration at the step-edge could influence the screening of the terrace-atoms, since the shadowcone of Pt atoms is larger than that of Rh atoms. To quantify this effect, simulations have been done with different Pt step-edge concentrations. At each chosen step-edge composition, the terrace composition was varied and the resulting backscattered yield was fitted according to:

$$X_{Pt,measured} = S(X_{Pt,step}) * X_{Pt,step} + (1 - S(X_{Pt,step})) * X_{Pt,terrace}$$

Here S represents the fraction of the backscattered signal which originates from the step-edges. From the results it was found that S = 0.60, independent from the Pt concentration at the step-edge. This value indicates that the atoms between the step-edge atoms are lightly shielded by the step-edge atoms (no shielding would give S = 0.5) which is also the reason that the Pt concentration has no major influence. The shielding factor of S = 0.6 has been used to correct the step-edge concentration as measured with the backscattering TOF. The validity of this approach was independently checked by measurements with the ion beam along the $[01\bar{1}]$ direction (see figure 4.1) which positions all terrace-atoms in the shadow-cones of the step-edge atoms. In this case all signal originates from the steps without need for correction. We have performed this measurement at one temperature and the resulting concentration is in good agreement with the corrected results from the measurements along the [010] direction. The step-edge concentration as a function of temperature has been plotted in figure 4.7, the measurements in the step-down geometry are depicted as open triangles and the measurement along the $[01\bar{1}]$ direction is indicated by an open square.

Clearly, the step-edge is much stronger enriched in Pt than the terrace. A similar behaviour has already been observed at the step-edges of a $Pt_{50}Rh_{50}(100)$ crystal with STM at room temperature [7].

4.5 Discussion

4.5.1 Step-edge composition measurements with TOF

In the present experiment a step-on-step focussing was used because of the large vicinal angle of the sample. The backscattering TOF measurements would therefore suffer from variations in the step-distance originating from e.g. step-roughening or a miscut angle with respect to the (410) plane. However, the shoulder/maximum in the Pt and Rh signals at an angle of incidence of 8° in figure 4.4 would not occur in that case. The maximum in the measurements for the step-edge focussing is less pronounced than for the simulations as can be seen in figure 4.5. This is probably due to the screening from the sample by the Ta cover at the sides or by the manipulator. Especially at small angles of incidence α the influence of any side-screening effect will be large since the obscured area is equal to the screening area divided by sin(α). This effect is not important for the quantitative interpretation of the measurement since only the absolute signal is affected . The measurements still clearly show three peaks which can be assigned to the corresponding peaks from the simulations, so the determination is of the step-edge composition is still valid.

If any irregularity in step spacing occurs, the experimental value for the step-edge composition will be closer to the average surface composition since the ion-beam will also be focussed on the terrace sites instead of on the step-edge. The experimentally found stronger Pt segregation to the step-edges, as compared to the surface composition thus represents a lower limit.

4.5.2 Pt$_{25}$Rh$_{75}$(410) step-edge and surface composition

Our temperature dependent measurements on Pt$_{25}$Rh$_{75}$(410) show a Pt enrichment which is in agreement with previous results on (111) and (100) surfaces of PtRh alloys as have been studied by several groups with various techniques including AES, ISS, atom probe FIM and STM. Calculations of Schoeb et al. [39] and Legrand and Treglia [32] show that the experimentally found Pt surface enrichment in those experiments can be understood on the basis of the difference in surface energy. Since we are particularly interested in segregation to different coordination sites, we will fit the measurements by calculating the composition of the terrace and the step-edges on the basis of bond energies. If only entropy-changes due to mixing are considered, then the relation between the bulk-composition X_b and the composition X_φ of a phase φ at a temperature T is given by:

$$\frac{X_\varphi}{1-X_\varphi} = \frac{X_b}{1-X_b} \exp^{\frac{\Delta G_{seg}}{RT}} \qquad\qquad \textbf{(32)}$$

The segregation energy, $\Delta G_{seg} = \mu_{Pt}^{0B} - \mu_{Pt}^{0\varphi} - \mu_{Rh}^{0B} + \mu_{Rh}^{0\varphi}$, is the difference in the standard chemical potential μ and can be seen as the energy gained or required to interchange an atom from one species from phase φ (bulk, surface, step) with an atom of the other species from the bulk. For flat surfaces, the segregation-energy is often expressed in terms of a difference in surface energy $\Delta\gamma$ times the specific surface area a [33, 34]. Equations like (32) have been formulated on the basis of thermodynamics only (see e.g. ref. [35]) under the assumption of two phases (bulk and surface), with random mixing of the species in each phase. However, it holds true for any phase in a binary alloy with an arbitrary number of phases, as long as the number of atoms in each phase is constant. In the broken bond model, the difference in the standard chemical potential can be found by counting the number of bonds between the phases. For an alloy with m phases, the difference in standard chemical potential for phase j equals:

$$\mu_{Pt}^{0j} - \mu_{Rh}^{0j} = \frac{\Delta\varepsilon}{2}\left(\sum_{i=1}^{m} Z_{ij}\right) + \Omega_{PtRh}\left(\sum_{i=1}^{m} Z_{ij}(1-2X_i)\right) \qquad \textbf{(33)}$$

The regular solution parameter, $\Omega_{PtRh} = \varepsilon_{PtRh} - \frac{1}{2}(\varepsilon_{PtPt} + \varepsilon_{RhRh})$, with ε_{PtRh} the Pt-Rh bond energy, indicates whether Pt and Rh tend to mix ($\Omega_{PtRh} < 0$) or will tend to form separate Pt and Rh clusters ($\Omega_{PtRh} > 0$). The difference in Pt-Pt and Rh-Rh bond energy is $\Delta\varepsilon = \varepsilon_{PtPt} - \varepsilon_{RhRh}$. Z_{ij} is the number of bonds per atom from phase j to phase i. Z_{ij} can thus be a fractional number and will be less or equal to the total number of bonds per atom, which is Z=12 for an fcc when only nearest neighbours are considered. The first term will account for any missing neighbours of phase j with respect to the bulk, whereas the second term accounts for any energy-changes due to mixing in an non-ideal solution. In this paper we will use three phases: bulk (b), terrace (t) and steps (s). As an example, counting the number of bonds for the steps is carried out in detail (see figure 4.1) below.

Each unit-cell consists of 1 step-edge atom, 7 terrace atoms and N bulk atoms. The total number of bonds from the step-edge to the terrace is 3 as is the number of bonds to the bulk. So for one step-edge atom the number of bonds is: $Z_{ss}=0$, $Z_{st}=3$, $Z_{sb}=3$. In the same way the number of bonds for the terrace-atoms and the bulk can be counted. The results are given in table 4.1.

Table 4.1: *Number of bonds between the phases (step-edges, surface, bulk) for a large number of atoms in the bulk (N→∞)*

phase i	# atoms/cell	# bonds to phase j			# bonds to phase j per atom (Zij)		
		step	surface	bulk	step	surface	bulk
step	1	0	3	3	0	3	3
surface	7	3	22	31	3/7	22/7	31/7
bulk	N	3	31	12N-34	0	0	12

The composition at the step-edge and terrace can now be calculated from equation (32) by recursive approximation. The difference in bond-energies $\Delta\varepsilon$ and the regular solution parameter Ω_{PtRh} are taken as the free parameters in the fit of the measured surface composition.

The measured surface composition as a function of temperature, at a certain combination of $\Delta\varepsilon$ and Ω_{PtRh}, is calculated from $X_{surface,measured} = \frac{1}{7}(X_{step} + 6 * X_{terrace})$ since there is one step-edge atom per eight atoms at the surface. Of these eight atoms, two terrace atoms will only be partly visible to the electrostatic analyser due to blocking. The 50% blocking of returning ions is estimated since neutralization of the returning ions by the step-edge atoms is involved rather than physical blocking.

The fit of the surface composition is given in figure 4.7 as the thin solid curve. There is excellent agreement between the measured and calculated surface composition for $\Delta\varepsilon = 2.1$ kJ/mol and $\Omega_{PtRh} = 0.42$ kJ/mol. The surface composition for an ideal solution ($\Omega_{PtRh} = 0$) has also been plotted in figure 4.7 as the thick solid line, in this case the best fit is found for $\Delta\varepsilon = 3.1$ kJ/mol. The latter value equals a difference in surface energy of $\Delta\gamma = \Delta G_{seg}/a = 0.14$ J/m^2. This compares reasonably well to the difference in surface energies at 0K, $\Delta\gamma_{PtRh}^{0} = 0.2$ J/m^2 [36] considering the accuracy and the temperature dependence of the surface free energy.

For many alloys it is possible to estimate the bond-energies from the heat of sublimation, which can be considered as the breaking of all bonds. However, this is not the case for Pt$_{25}$Rh$_{75}$(410) since Rh has a larger heat of sublimation which would result in a negative value for $\Delta\varepsilon$ [37]. It was already mentioned by others [27] that, based solely on the sublimation energy of Pt and Rh, Rh segregation would be expected instead of the generally observed Pt segregation. The calculated Pt concentration at the step-edges has been plotted in figure 4.7 as the dotted (ideal solution) and dashed (regular solution) curves. We find that the Pt segregation to the step-edges is much larger than expected based on the ideal solution model. The step-edge composition as calculated according to the regular solution predicts the step-edge composition much better, but the positive value of Ω_{PtRh} would tend to favor a phase separation of the Pt$_{25}$Rh$_{75}$(410) surface. The composition of the second layer would therefore be slightly Pt enriched. This is in contradiction with the currently observed second layer Rh enrichment in our experiments as well as previous reports where a sandwich-like Pt-Rh-Pt enrichment was found that continues with a decreasing amplitude for successive atomic layers around the Pt bulk concentration [38]. For this behaviour a negative heat of mixing, or $\Omega_{PtRh} < 0$, is required. The sandwich structure might help to stabilize the double atomic height steps of Pt$_{25}$Rh$_{75}$(410) since the third (Pt enriched) layer will be the surface of the lower terrace which is also Pt enriched. One paper [10] shows Pt enrichment of the surface and Rh enrichment for all the deeper layers with a decreasing magnitude for Pt$_{25}$Rh$_{75}$(100) (no alternating layers). This behaviour is attributed to a local equilibrium, where the exchange of atoms only occurs in the first atomic layers, and these layers are thus depleted in the segregation element. As discussed above, the broken bond model is unable to reproduce this kind of behaviour since a equilibrium is assumed over all atomic layers. As a result, there will be either alternating layers ($\Omega_{PtRh} < 0$) or all surface layers will be enriched in the same element ($\Omega_{PtRh} > 0$) that has the lowest surface energy. Since the results of a non-equilibrium model depend strongly on the number of atomic layers that are in equilibrium, and we have only the experiments of [10] as an indication for this number, we choose not to present such a model here. Instead, we tried to improve the broken bond model

by using bond energies that depend on the coordination of the atom. The bond energies vary due to the relaxation of atoms at the surface and the steps. An atom with a larger number of broken bonds, or a lower coordination, will bond stronger to the remaining neighbours. This effect will thus be especially important for the step-edge atoms. This idea has been introduced by Schoeb et al. [39] as the surface modified pair potential (SMPP) model. Their calculations on PtRh clusters of 201 atoms showed Pt segregation to the steps. A bulk concentration of 25% Pt would yield 60% Pt at the step-edges at 700 °C, which is less pronounced than found by our experiments. However, with only 201 atoms in a cluster, the bulk concentration will vary significantly during segregation to the surface.

A coordination dependent bond energy can be implemented by adjusting equation (32) accordingly. As a first estimate, the bond energies of the bulk and surface atoms are kept equal and the bond energy of the step-edge atoms is allowed to vary. The best results are obtained when
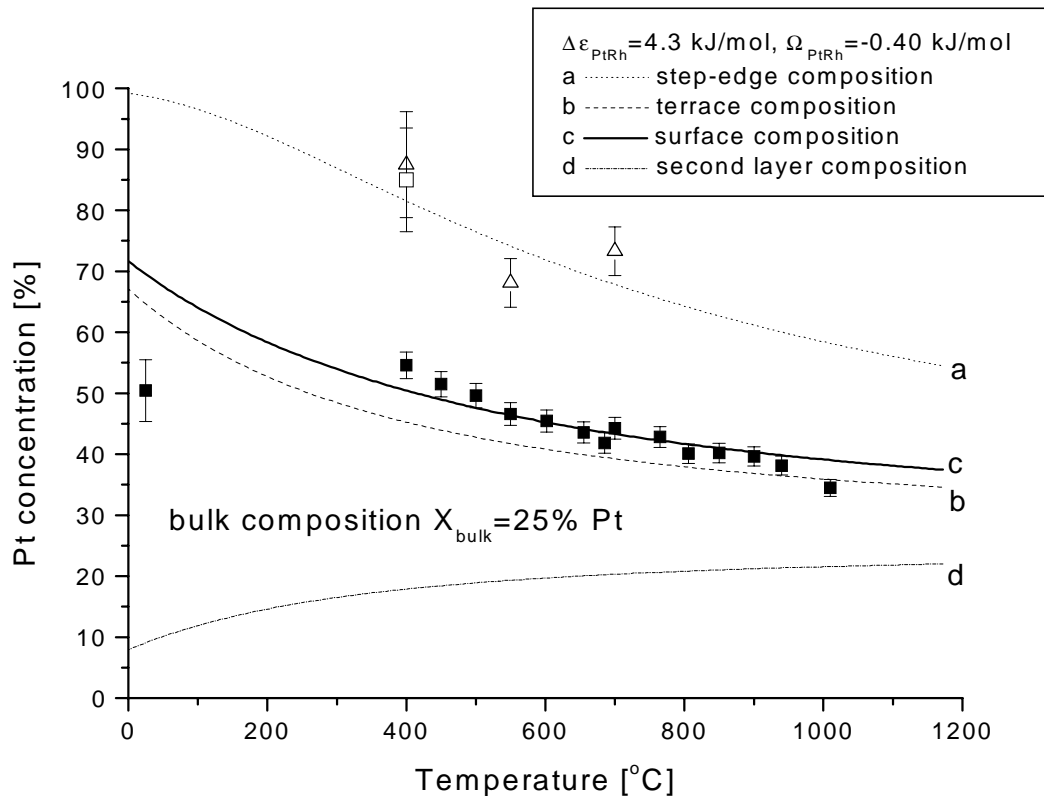
Figure 4.8: *The measured surface composition (squares) as a function of temperature for the EARISS measurements and the calculated step-edge (dotted, line a), terrace (dashed, line b), surface (solid, line c) and second layer composition (dash-dot, line d) according to the broken bond model using a different bond energy for the step-edge atoms with respect to the atoms at the surface and in the bulk. The error bars on the first points show the accuracy including the calibration accuracy, the subsequent error bars show the accuracy without calibration accuracy.*

the bond energy at the step-edges is 70% larger than for the bulk, $\Delta\varepsilon$ = 3.4 *kJ/mol* and Ω_{PtRh} = -0.40 *kJ/mol*. Figure 4.8 shows the composition of the step-edge, terrace and second layer as a function of temperature as calculated with the values above. The experimental and calculated values are now in good agreement, although the factor 1.7 difference in bond energy of the step-edge and the terrace atoms seems rather large.

4.6 Conclusions

For the first time TOF has been used to measure the step-edge composition of an alloy as a function of temperature. As expected, the segregation of Pt to the step-edges is stronger than the segregation to the terrace. The measured Pt$_{25}$Rh$_{75}$(410) surface composition can be explained very well within the ideal solution (Langmuir-McLean) broken bond model with a difference in bond energy of 3.1 kJ/mol (0.14 J/m$^{2)}$). However, in order to explain the measured Rh enrichment of the second layer and step-edge composition, a regular solution model has to be used with a coordination dependent bond energy. The best fit is obtained for a 70% larger bonding at the step-edges compared to the surface, a difference in bond energy of $\Delta\varepsilon$ = 3.4 *kJ/mol* and a regular solution parameter of Ω_{PtRh} = -0.40 *kJ/mol*. A factor of 1.7 between the difference in bond energy at the step-edges and the bulk seems rather large, although the prediction of the step-edge composition above 400 °C is in good agreement with the few obtained experimentally values. Corrected Effective Medium (CEM) calculations in literature [32] report a factor of 1.4 between the bond energies of step-edge and terrace atoms.

Although the technique for the current paper has been applied on a vicinal surface with a relative large number of step-edges, we think that it can be used for most flat crystal surfaces. In the general case the backscattering TOF will be used in a non-focused mode in which the terrace-sites are shadowed by a large number of small angle deviations of the primary particles. The ions will then skim over the terrace atoms until they hit a step-edge which causes them to return to the detector. The loss of signal due to the lower number of step-edges and the loss of the focussing effect can be partially made up for by choosing a larger primary energy, thereby increasing the detector efficiency. This is possible since the exact shape of the shadowcone will be less important if a non-focussed mode is used. An example where the technique is applied to crystals with an intermediate number of step-edges is shown in chapter 6 where step-edge composition measurements on Cu3Au(17,1,1) are presented.

References:

1. Z. Knor, Surf. Sci. 169 (1986) L317

2. J.E. Reutt-Robey, D.J. Doren, Y.J. Chabal, S.B. Christman, Phys. Rev. Letters 24 (1988) 2778

3. H. Hopster, H. Ibach, G. Comsa, J. Catal. 46 (1977) 37

4. G. Dufour, F. Rochet, F.C. Stedile, Ch. Poncey, M. De Crescenzi, R. Gunnella, M. Froment, Phys. Rev. B 56 (1997) 4266

5. H.A.C.M. Hendrickx, B.E. Nieuwenhuys, Surf. Sci. 175 (1986) 185

6. K. Besocke, H. Wagner, Phys. Rev. B 8 (1973) 4597

7. P.T. Wouda, B.E. Nieuwenhuys, M. Schmid, P. Varga, Surf. Sci. 359 (1996) 17

8. H. Niehus, W. Heiland, R.J. MacDonald, Surf. Sci. Reports 17 (1993) 213

9. H.H. Brongersma, P.M. Mul, Surf. Sci. 35 (1973) 393

10. E. Platzgummer, M. Sporn, R. Koller, S. Forsthuber, M. Schmid, W. Hover, P. Varga, Surf. Sci. 419 (1999) 236

11. D.D. Beck, G.L. DiMaggio, G.B. Fisher, Surf. Sci. 297 (1993) 293

12. Y.G. Chen, D.J. O'Connor, K. Wandelt, R.J. MacDonald, Surf. Sci. 328 (1995) 21

13. F.C.M.J.M. van Delft, A.D. van Langeveld, B.E. Nieuwenhuys, Surf. Sci. 189/190 (1987) 1129

14. D.D. Beck, C.L. DiMaggio, G.B. Fisher, Surf. Sci. 297 (1993) 293

15. W.F. Banholzer, Y.O. Park, K.M. Mak, R.I. Masel, Surf. Sci. 128 (1983) 176

16. W.F. Banholzer, R.E. Parise, R.I. Masel, Surf. Sci. (1985) 653

17. J.M. Gohndrone, Y.O. Park, R.I. Masel, Journal of Cat. 95 (1985) 244

18. F.C.M.J.M. van Delft, J. Siera, B.E. Nieuwenhuys, Surf. Sci. 208 (1989) 365

19. B.E. Nieuwenhuys, J. Siera, K.I. Tanaka, H. Hirano, ACS. Symp. Series 552: Environmental catalysis (ACS Washington d.c. 1994)

20. M. Aono, M. Katayama, E. Nomura, T. Chassé, D. Choi, M. Kato, Nucl. Instrum. Methods Phys. Res. B 37/38 (1989) 264

21. G. Hellings, M.O. Hevanger, S.W. Boelens, C.L.C.M. Knibbeler, H.H. Brongersma, Surf. Sci. 162 (1985) 913

22. M. Henzler, Surf. Sci. 22 (1970) 12

23. M.H. Langelaar, M. Breeman, A.V. Mijiritskii, D.O. Boerma, Nucl. Instrum. Methods Phys. Res. B (1997) 587

24. R.H. Bergmans, M. van de Grift, A.W. Denier van der Gon, H.H. Brongersma, Surf. Sci.

345 (1996) 303

25. J. Florencio, D.M. Ren, T.T. Tsong, Surf. Sci. 345 (1996) L29

26. J. Siera, F.C.M.J.M. van Delft, A.D. van Langeveld, B.E. Nieuwenhuys, Surf. Sci. 264 (1992) 435

27. W.Athenstaedt, M. Leisch, Applied Surf. Sci. 94/95 (1996) 403

28. M. Sundaraman, S.K. Sharma, L. Kumar, R. Krishnan, Nucl. Instrum. Methods Phys. Res. B 191 (1981) 289

29. D.D. Beck, G.L. DiMaggio, G.B. Fisher, Surf. Sci. 297 (1993) 293

30. G. Carter, J.S. Colligon, Ion bombardment of Solids, American Elsevier, New York (1960)

31. N. Laegreid, G.K. Wehner, J. of appl. Phys., 32 (1961) 365

32. B. Legrand, G. Treglia, Surf. Sci. 236 (1990) 398

33. F.J. Kuijers, B.M. Tieman, V. Ponec, Surf. Sci. 75 (1978) 657

34. F.L. Williams, D. Nason, Surf. Sci. 45 (1974) 377

35. Surface Segregation, J. Du Plessis, Sci-Tech Publications 1990,

36. F.R. de Boer, R. Boom, W.C.M. Mattens, Cohesion in metals, (Elsevier, Amsterdam 1988)

37. R. Hultgren, R. Orr, P. Anderson, K. Kelley, Selected values of thermodynamical properties of metals and alloys (Wiley, New York 1963)

38. D. Ren, T.T. Tsong, Surf. Sci. 184 (1987) L439

39. A.M. Schoeb, T.J. Raeker, L.Yang, X. Wu, T.S. King, A.E. Depristo, Surf. Sci. Letters 278 (1992) L125

The surface and step-edge composition of clean and oxidized $Pt_{50}Rh_{50}(511)$

5

5.1 Abstract

Low energy ion scattering has been used to perform site-specific composition measurements on $Pt_{50}Rh_{50}(511)$ between room temperature and 1000°C. The results show that the clean surface is strongly enriched in platinum. At all temperatures the Pt enrichment of the step edges is significantly larger than the Pt enrichment of the terraces, which can be attributed to the lower coordination of the step-edge atoms. A simple broken bond model is adequate to calculate the composition of the surface and the step edges at high temperatures. Between 650°C and 800°C a large decrease in Pt surface concentration occurs with increasing temperature. Two possible explanations are discussed here. The first is a bulk phase de-mixing at temperatures below 760°C, which would lead to enhanced segregation due to the local increase of the Pt concentration in the sub-surface region. The second possible explanation is a surface phase transition from a missing row reconstruction below 650°C to an unreconstructed surface above 800°C. Here the enhanced segregation at lower temperatures is due to the decreased orientation of the surface atoms in the reconstructed phase.

The influence of oxygen on the segregation is studied by measuring the surface and step-edge compositions after the adsorption and subsequent removal of oxygen. Following this preparation, the step-edge and surface Pt concentrations are equal to each other within the experimental accuracy. The results show weak Rh segregation on the oxygen treated surface, in contrast to the strong Pt segregation found on the clean surface. Since there is only limited segregation in the case of oxidized PtRh, the surface compositions of PtRh crystals with different orientation but the same bulk composition will be equal. Therefore the different activities of those crystals have to be attributed to the different surface structure.

5.2 Introduction

Alloy catalysts often display superior properties with respect to the pure constituents regarding selectivity and reactivity. Pt and Rh are the main active components in catalysts used in a range of processes. Bimetallic Pt-Rh catalysts are used as "three way" automotive exhaust gas catalysts. These catalysts simultaneously convert the harmful components NO_x, CO and hydrocarbons into N_2, CO_2 and H_2O [1- 3]. The catalytic properties of alloy catalysts are strongly influenced by their structure and composition. Surface composition measurements on real catalysts under working conditions are possible, but they allow limited control over the experiments. Combining results on real catalysts with measurements on model systems, like single crystals in UHV environments, provide a more detailed picture of the fundamental processes at the surface. In this respect extensive research has been performed on various flat single-crystal PtRh surfaces. From these studies it is known that the clean PtRh surface is Pt enriched, whereas the surface of oxidized PtRh shows Rh segregation. Previous papers on segregation to the low-index surfaces of PtRh alloys can e.g. be found in references [1-3, 5, 7-9, 17-24, 27, 35-39].

The atoms at the surface of dispersed catalysts, like the PtRh three way catalysts, generally have a lower coordination than the surface atoms of "flat" samples. Therefore it is also important to understand the segregation to low coordination sites. From simple segregation models it is expected that lower coordinated sites will show enhanced segregation compared to the higher coordinated sites [4]. Experimentally, few studies exist of segregation to low coordination sites because it requires site selective measurement methods. Scanning Tunnelling Microscope (STM) measurements by Wouda et al. [3] on $Pt_{50}Rh_{50}(100)$ showed that the step edges of $Pt_{50}Rh_{50}(100)$ are strongly enriched in Pt with respect to the surface. On the other hand, Hebenstreit et al. [5] found a composition of 73% Pt at the step edges of a $Pt_{25}Rh_{75}(111)$ crystal, which was only slightly larger than the terrace composition. Recently, we have demonstrated how ion scattering techniques can be employed for site selective, temperature-dependent composition measurements on vicinal single crystal surfaces [6]. In these experiments the step-edge composition was determined using Time Of Flight (TOF) measurements in a backscattering geometry (also known as CoAxial Impact Collision Ion Scattering Spectroscopy (CAICISS)) [6]. By carefully selecting small angles of incidence, causing the terrace atoms to shadow each other, backscattering is limited to hard collisions from step-edge sites only. The average composition of the outermost atomic layer was determined separately by Low-Energy Ion Scattering (LEIS), taking advantage of the high neutralization probability of the used noble gas ions in combination with an electrostatic analyser. Our study of the $Pt_{25}Rh_{75}(410)$ surface showed a significantly enhanced Pt segregation at the step edges compared to that at the terraces [7].

Here, we report on our studies of the segregation behaviour of the vicinal $Pt_{50}Rh_{50}(511)$ single crystal surface. This surface was selected for the following reasons: (1) The 50% bulk composition is significantly different from the bulk composition used in our previous study, but still low enough to allow incomplete Pt segregation to the surface at room temperature. (2) The structure of the step edge is different from that in the previous study on the (410) surface. This

should reveal whether the segregation depends strongly on the type of step edge. (3) The step-edge composition measurements on Pt$_{25}$Rh$_{75}$(410) were hampered by the combination of double atomic height steps, a relatively large distance between the step-edge atoms, and unshielded rows of atoms between the rows that contain the step-edge atoms. The Pt$_{50}$Rh$_{50}$(511) crystal has none of these disadvantages, thus allowing for a more straightforward and accurate determination of the step-edge composition.

Our previous study on the Pt$_{25}$Rh$_{75}$(410) was limited to the clean surface. However, PtRh alloy based catalysts are often operated in an oxidizing environment [8]. It is known that in the presence of oxygen, Pt segregation is inhibited and even reversed. Rh segregation was observed by, for example, Athenstaedt et al. [9] using TOF atom probe measurements on an oxygen contaminated Pt$_{90}$Rh$_{10}$ alloy between 300°C and 1100°C. In order to study the influence of an oxidizing environment we will compare the surface and step-edge composition of the oxygen treated surface with the surface and step-edge composition of the clean surface.

5.3 Experimental

5.3.1 Sample preparation and characterization

The Pt$_{50}$Rh$_{50}$(511) sample was mounted on a Mo sample holder and covered at the edges with a Ti foil to screen the sides of the sample from the ion beam at grazing angles of incidence. During the measurements on the clean Pt$_{50}$Rh$_{50}$(511) surface, the temperature of the sample was measured by a CHINO comet 1000 pyrometer with an absolute accuracy of ±50°C and a reproducibility of ±10°C. Below 400°C the sample temperature was calculated using the input power of the heating wire and interpolation between room temperature (RT) and temperatures above 400°C. From this calibration curve it is estimated that the absolute accuracy of ±50°C is also achieved between RT and 400°C. During the composition measurements on the oxygen covered Pt$_{50}$Rh$_{50}$(511) surface an impac IP 120 pyrometer has been used with a reproducibility of ±1°C and an absolute accuracy of ±5°C over the measuring range of 160°C-1250°C. The same emission coefficient has been used for the clean and the oxidized surface.

Prior to every measurement, the sample is cleaned by 2 keV Ar$^+$ sputtering at 700 °C and flashed several times to 1050°C which results in a clean and well ordered surface as evidenced by TOF-SARS and LEED experiments. The LEED pattern, including the distance of the satellite spots and the spot splitting, is consistent with a (511) surface. Spot profile analysis low energy electron diffraction (SPA-LEED) characterization (see e.g. [10]) was carried out in a different UHV instrument [11], using the same sample cleaning procedures. The width of the (0,0) LEED spot at room temperature (RT) corresponds to an average step spacing of 12.8 Å which is within 4% of the value expected for the (511) surface. Finally, also the angle of incidence dependent ion scattering yield in the step-up and the step-down geometry, as described later, is consistent with the vicinal angle of the (511) surface. Therefore, it is concluded that the clean surface is a well-ordered Pt$_{50}$Rh$_{50}$(511) with regularly spaced single atomic-height steps. A schematic view of the (511) surface is shown in figure 5.1 and will be discussed in more detail in section 2.2.
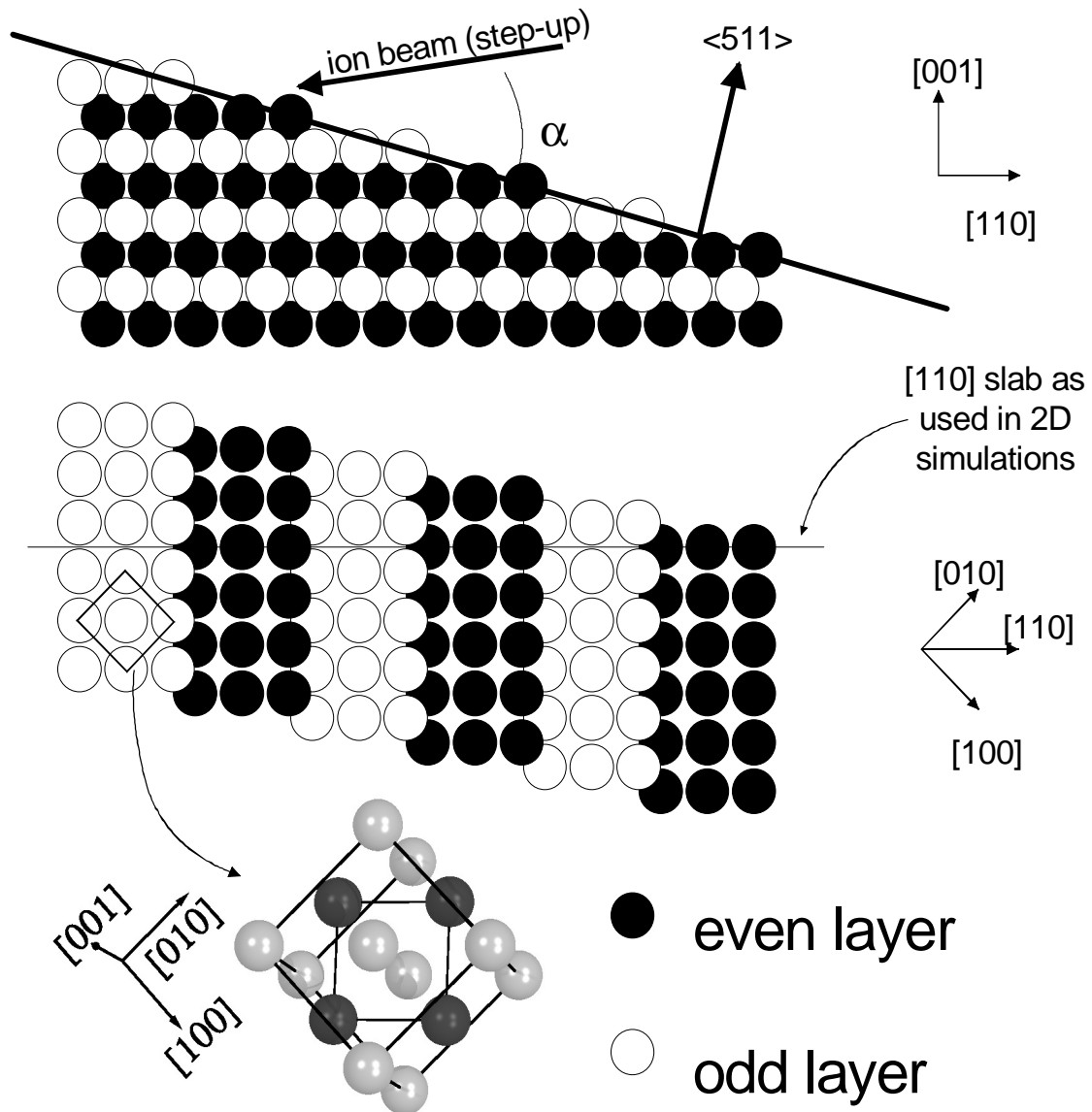
Figure 5.1: *Schematic representation of a $Pt_{50}Rh_{50}(511)$ crystal. Indicated in the side-view is the direction of the ion beam in the "step-up" configuration. The angle of incidence α is defined with respect to the sample surface. The top-view shows the [110] cross-section of the slabs as used in the 2D ion trajectory simulations.*

Before performing composition measurements on the clean surface, the sample is kept for 5 minutes at the desired temperatures above 900°C. During composition measurements below 600°C the sample is allowed to reach equilibrium for up to 4 hours. All LEIS measurements on the clean surface have been performed at the desired temperature (no "quenching"). To study the influence of oxygen on the segregation behaviour, the cleaned sample is exposed for 15 minutes to a pressure of $1*10^{-6}$ mbar of oxygen at 400°C. The sample is allowed to cool to below 160 °C (this takes about three minutes) before the oxygen is removed from the UHV system. The presence of oxygen on the surface would hamper the composition determination by ion scattering

because it shields the Pt and Rh atoms. Therefore the oxygen is removed prior to the composition measurements by exposing the sample for 10 minutes to $1*10^{-6}$ mbar hydrogen at RT. It is expected that the surface composition does not change during this removal of the oxygen due to the kinetics of the segregation [36]. We will return to this assumption in the discussion section.

5.3.2 Ion scattering: method, simulations and experimental details

All ion scattering measurements have been performed in an UHV setup which has been described in detail elsewhere [12]. The setup consists of a near 180 degrees backscattering TOF (CAICISS), a 35 degrees forward TOF Scattering And Recoiling Spectrometer (TOF-SARS), a 145 degrees backscattering LEIS setup with an electrostatic analyser and a 2D detector (Energy and Azimuthal Resolved Ion Scattering Spectrometer (EARISS) [11]) and a standard Low Energy Electron Diffraction (LEED) screen. A schematic representation of the Pt$_{50}$Rh$_{50}$(511) crystal is given in figure 5.1. The following definitions will be used: the terrace atoms are those atoms in figure 5.1 that have two or four missing neighbours, the step-edge atoms have five missing neighbours. The surface consists of all terrace and step-edge atoms together. By aligning the ion beam at small angles of incidence along the [110] direction it is expected that all the terrace atoms in a certain row are shielded from the ion beam by the step-edge atoms in the same row. TOF measurements on the step-edge composition can be performed in the "step-up" or "step-down" geometry. The step-up geometry is defined such that the ion beam is facing the step edges and the projection of the ion beam on the surface points in the [$\bar{1}\bar{1}$0] direction (figure 5.1). In the step-down geometry the crystal azimuth is rotated over 180 degrees with respect to the step-up geometry. The projection of the ion beam points in the [110] direction. Ion trajectory simulations show that the step-up geometry is better suited to study the step-edge composition of the (511) surface than the step-down geometry. Therefore we will only discuss the step-up geometry results in the remainder of the paper.

In figure 5.2 the principle of the step-edge composition measurements is shown by simple two-dimensional trajectory simulations for the step-up geometry. The figure shows the trajectories of 4 keV Ne$^+$ in a [110] "slice" of Pt$_{50}$Rh$_{50}$(511), which is also indicated in figure 5.1. The indicated slice only consists of "even" atoms as the "odd" atoms are located in a [110] slice that is shifted over half a lattice distance in the [$\bar{1}$10] direction (here "even" and "odd" may be interchanged as the slabs are indiscriminate). In figure 5.2a the angle of incidence is $\alpha = 5°$ which prevents hard collisions, resulting in a negligible yield in a CAICISS measurement. In figure 5.2b the trajectories are plotted for an angle of incidence of $\alpha = 10°$. In this geometry ions can have hard collisions with step-edge atoms, whereas the terrace and bulk atoms are shielded by the step-edge atoms. Therefore only the step edges are probed. Furthermore it can be seen that the deflected projectiles are focussed onto the step edges, which causes enhanced backscattering from the step edges. In figure 5.2c the angle of incidence is increased to $\alpha = 20°$. Even at this large angle of incidence all terrace and bulk atoms are shielded by the step-edge atoms according to the 2D simulation. However, the projectiles are no longer focussed onto the step edges resulting in a smaller backscattered yield than in the previous case.
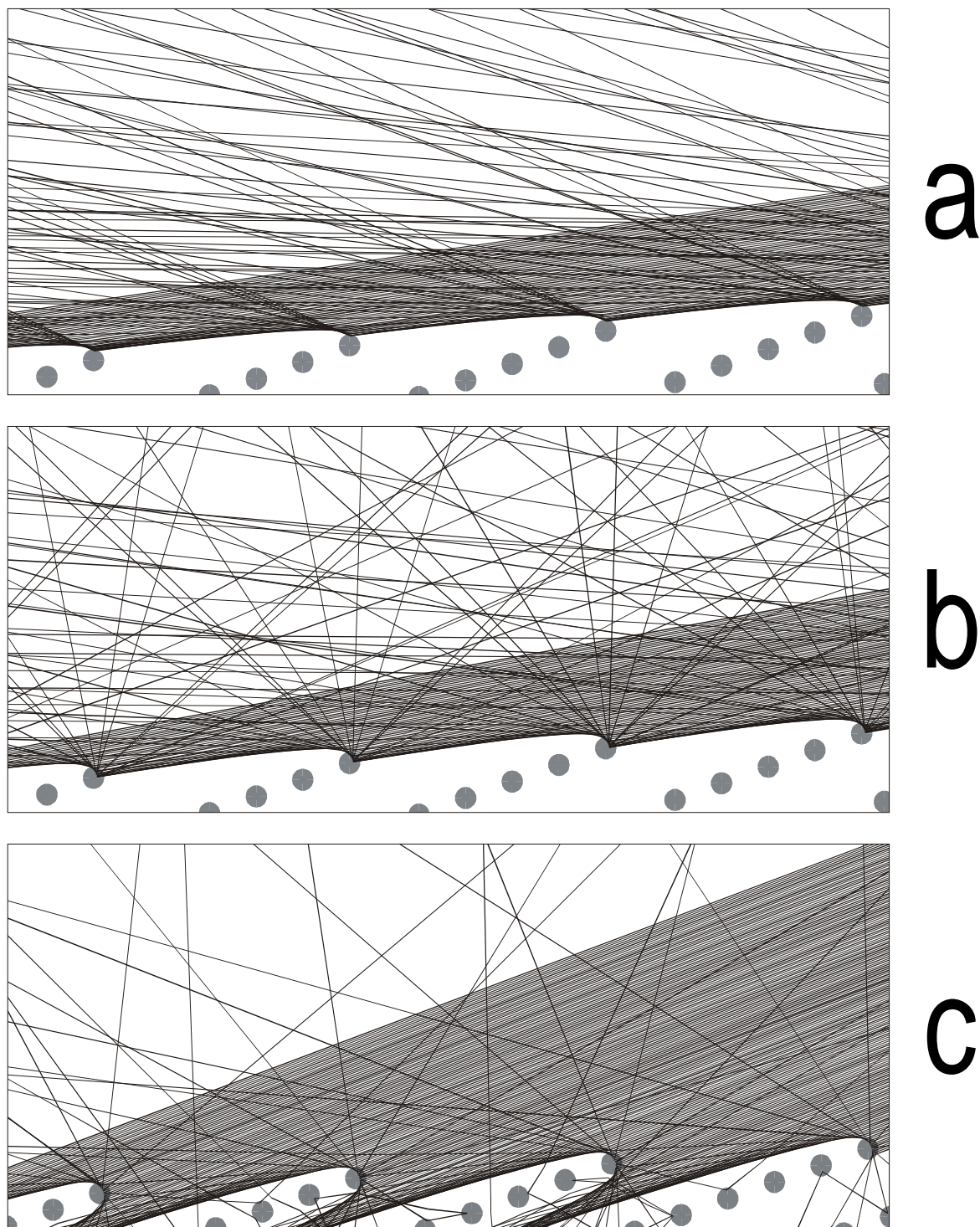
Figure 5.2: *2D ion trajectory simulations of 4 keV Ne$^+$ on the Pt$_{50}$Rh$_{50}$(511) crystal. a) Angle of incidence α=5°. Due to the small angle of incidence the ions skim over the surface without hard collisions, resulting in no backscattered yield. b) Angle of incidence α=10°. Almost all incoming ions have hard collisions at the step edges, resulting in a large backscattered yield. c) Angle of incidence α=20°. No hard collisions occur on other atoms but the step-edge atoms. Ions are lost in the bulk, resulting in a smaller backscattered yield than in the previous case.*

Although the two-dimensional simulation gives good insight into the method, it is necessary to carry out full three-dimensional trajectory simulations on the crystal in order to determine quantitatively which sites contribute to the backscattered yield. Therefore, ion trajectory simulations have been performed for 4 keV Ne$^+$ on Pt$_{50}$Rh$_{50}$(511) with MATCH [13]. In MATCH the scattering events are calculated using the binary collision approach [14] and the interaction between the projectile and the target is described by the Ziegler/Biersack/Littmark approximation [15] to the shielded Coulomb potential. The backscattered yield has been calculated for angles of incidence between 4 and 60 degrees in the step-up and step-down direction for single and double atomic stepped surfaces. The result for the single atomic stepped surface in the step-up geometry is shown in figure 5.3. In this step-up geometry the projectiles can return to the detector at angles of incidence larger than 5 degrees. Up to an angle of incidence of 15 degrees the step-edges contribute for at least 95% to the total yield, which shows that this geometry is ideally suited for the step-edge composition measurements. It was verified that for these angles of incidence the double atomic height steps would also yield exclusively information about the step-edge composition. Occasional double atomic height steps will thus not influence the results of the step-edge composition measurements. Around an angle of incidence of 10 degrees there is a maximum in the signal from the step edges, corresponding to the focussing of the projectiles on the step edges as visualized in figure 5.2b. For an angle of incidence between 30 and 60 degrees the surface layer and the second layer are probed simultaneously. The step-up geometry is thus not suited for an independent surface composition measurement.

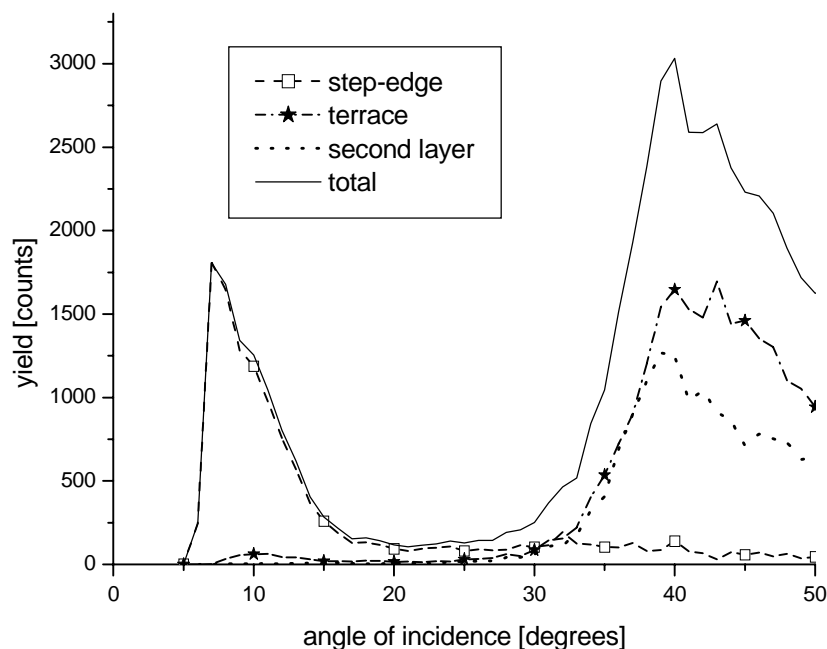**Figure 5.3:** *Results of 3D ion trajectory simulations of 4 keV Ne$^+$ on Pt$_{50}$Rh$_{50}$(511), for the step-up geometry. The back-scattered yield is shown versus angle of incidence. The step-edge contribution is indicated by the open squares.*

Based upon these trajectory simulations, the step-edge composition measurements have been performed with the backscattering TOF, using 4 keV Ne^+ at an angle of incidence of $\alpha=9°$ to $\alpha=13°$ with 1 degree steps in the step-up direction (see figure 5.1). The ion dose per measurement was less than $5*10^{11}$ ions/cm^2 to ensure that no significant radiation damage was caused to the step edges during the experiments ("static" LEIS[16]). Even if it is assumed that every projectile sputters atoms from the step edges with an efficiency of two atoms per ion, less than one percent of the step edges would be damaged during the experiment. The step-edge composition experiments have been performed between RT and 700°C. Measuring at temperatures above 700°C is not possible since it requires e-beam heating of the sample, which generates high count-rates in the TOF detector. The sensitivity of the TOF setup for Pt is a factor 2.2 larger than for Rh. Details about the calibration method are presented in our previous study on $Pt_{25}Rh_{75}(410)$ [6]. The TOF signals are determined by fitting the TOF spectra with Gaussian peaks for the Pt and Rh signal. Each peak yields a background signal which is modeled to increase linearly from the start of the peak to the end, and subsequently decays exponentially at larger flight times. The width of the peaks is kept constant, since these are related to the pulse shape of the incoming ion beam. The exponential decay is assumed equal for the tails of the Pt and the Rh peaks as they depend on the penetration depth of the ions, which is in turn related to the angle of incidence.

The surface composition (terrace and step-edge sites combined) has been measured with the EARISS [12, 32] using 3 keV Ne^+ or 2 keV He^+. The ion beam is aimed perpendicular with respect to the surface of the sample whereas detection occurs of ions that are scattered over 145 degrees. The ion dose was less than $1*10^{12}$ ions/cm^2 to ensure static LEIS measurements. The sensitivity of the EARISS for Pt is 1.46 (1.21) times larger than the sensitivity for Rh in the case of 3 keV Ne^+ (2 keV He^+) as determined using clean and well ordered Rh(100) and Pt(111) single crystals [6]. For Ne^+, the contribution of deeper layers to the backscattered yield will be small as most of the projectiles will have been neutralized due to multiple scattering. In earlier experiments on $Pt_{25}Rh_{75}(410)$ [6] the second layer contribution to the total yield has been determined to be less than 4%. The terraces of the (511) surface are identical to those of the (410) surface, therefore a minor contribution from the second layer is expected for the (511) surface too. The second layer contribution has been neglected for the surface composition measurements. A maximum error of 4% in the determined surface composition can occur in case of complete segregation of Pt to the surface and complete depletion Pt in the second layer. In the next section the actual error due to deeper layer contribution will be estimated based on the measured surface composition and the estimated second layer composition.

For the oxygen exposure experiments, the surface composition has also been measured using the EARISS with 2 keV He^+ and 3 keV Ne^+. The measurements with He^+ have been used to estimate the amount of oxygen at the surface during the different stages of the reduction process. The actual surface composition measurements have been performed with Ne^+ after the complete removal of oxygen.

5.4 Results

5.4.1 composition measurements on clean $Pt_{50}Rh_{50}(511)$

In figure 5.4 EARISS measurements are shown of the clean $Pt_{50}Rh_{50}(511)$ surface (prepared by heating and slowly cooling to RT) using 2 keV He^+ (top) and 3 keV Ne^+ (bottom). Clearly, the Pt signal (high energy peak) is much more intense than the Rh signal (low energy peak), which directly shows that the clean $Pt_{50}Rh_{50}(511)$ is strongly enriched in Pt (even after taking into account the relative sensitivity to Pt in these experiments). The He^+ and Ne^+ measurements show the same surface Pt concentration of X_{surf} = 85 % Pt. However, since the scattered background in the Ne^+ experiments is much lower than the background in the He^+ experiments, we use the Ne^+ data in the remainder of the paper for the surface composition quantification.
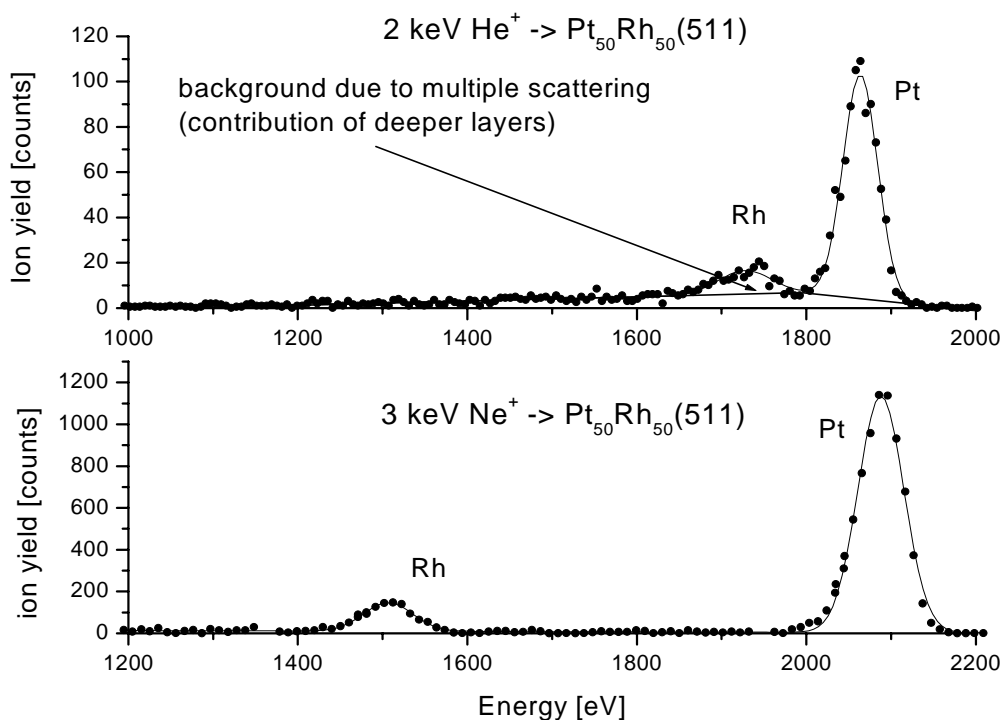
Figure 5.4: *Surface composition measurements on clean $Pt_{50}Rh_{50}(511)$: LEIS spectra of clean $Pt_{50}Rh_{50}(511)$ using 2 keV He^+ respectively 3 keV Ne^+.*

In figure 5.5, the TOF backscattered yields from Rh and Pt are presented as a function of the angle of incidence for the clean $Pt_{50}Rh_{50}(511)$ surface at RT. The angular dependency of the scattered yield is similar to the simulated angular dependency shown in figure 5.3. The peak around 10 degrees is caused by scattering from the step edges, whereas the peak around 40 degrees is caused by scattering from the surface and the second layer. The yield at every angle has been determined from TOF spectra such as the two examples shown in the insets of figure

5.5 (for angles of incidence $\alpha = 15°$ and $\alpha = 45°$). The spectrum obtained at 15 degrees clearly shows a large Pt/Rh ratio, which indicates that the step edge is strongly enriched in Pt. In the spectrum obtained at 45 degrees, the yields of Pt and Rh (originating from the surface and the second layer) are about equal. Using the surface composition of $X_{surf} = 85$ % Pt as measured with the EARISS, and the relative contributions of the surface and the second layer to the TOF signal as determined from the ion trajectory simulations, we estimate that the second layer composition is 35 ± 10 % Pt. The second layer is thus Pt depleted. The contributions to the above mentioned 10 % accuracy are the dependencies in the relative contributions of the surface and the second layer on different screening lengths in the ion trajectory simulations (± 4 %), the measurement accuracy (± 2 %) and the calibration accuracy (± 4 %).
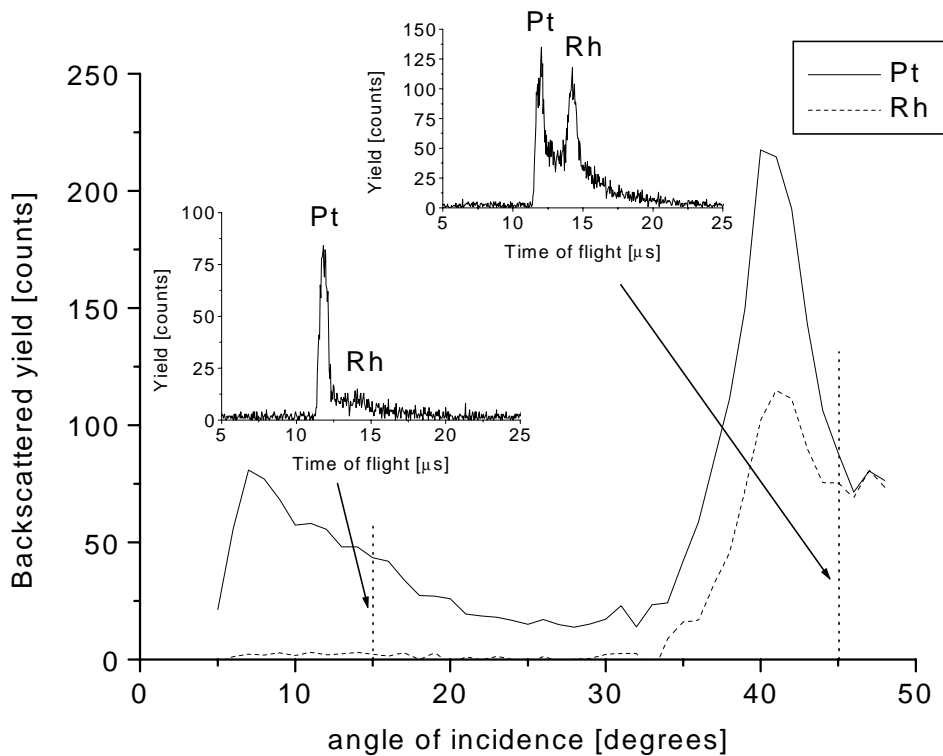
Figure 5.5: *Step-edge composition measurements on clean $Pt_{50}Rh_{50}(511)$: Pt and Rh yield, as determined from TOF spectra, as a function of the angle of incidence on clean $Pt_{50}Rh_{50}(511)$. The insets show TOF spectra at two selected angles of incidence.*

The temperature dependent surface composition and step-edge compositions are presented in figure 5.6. The measurements have been performed non-sequentially and spread over several days. The reproducibility of the surface composition for any given temperature is within ± 2%, which is also the accuracy of the sensitivity calibration for Pt and Rh. The maximum error in the surface composition determination due to the contribution of the second layer to the total backscattered yield is +1/-0 % Pt. This number is based on the measurements
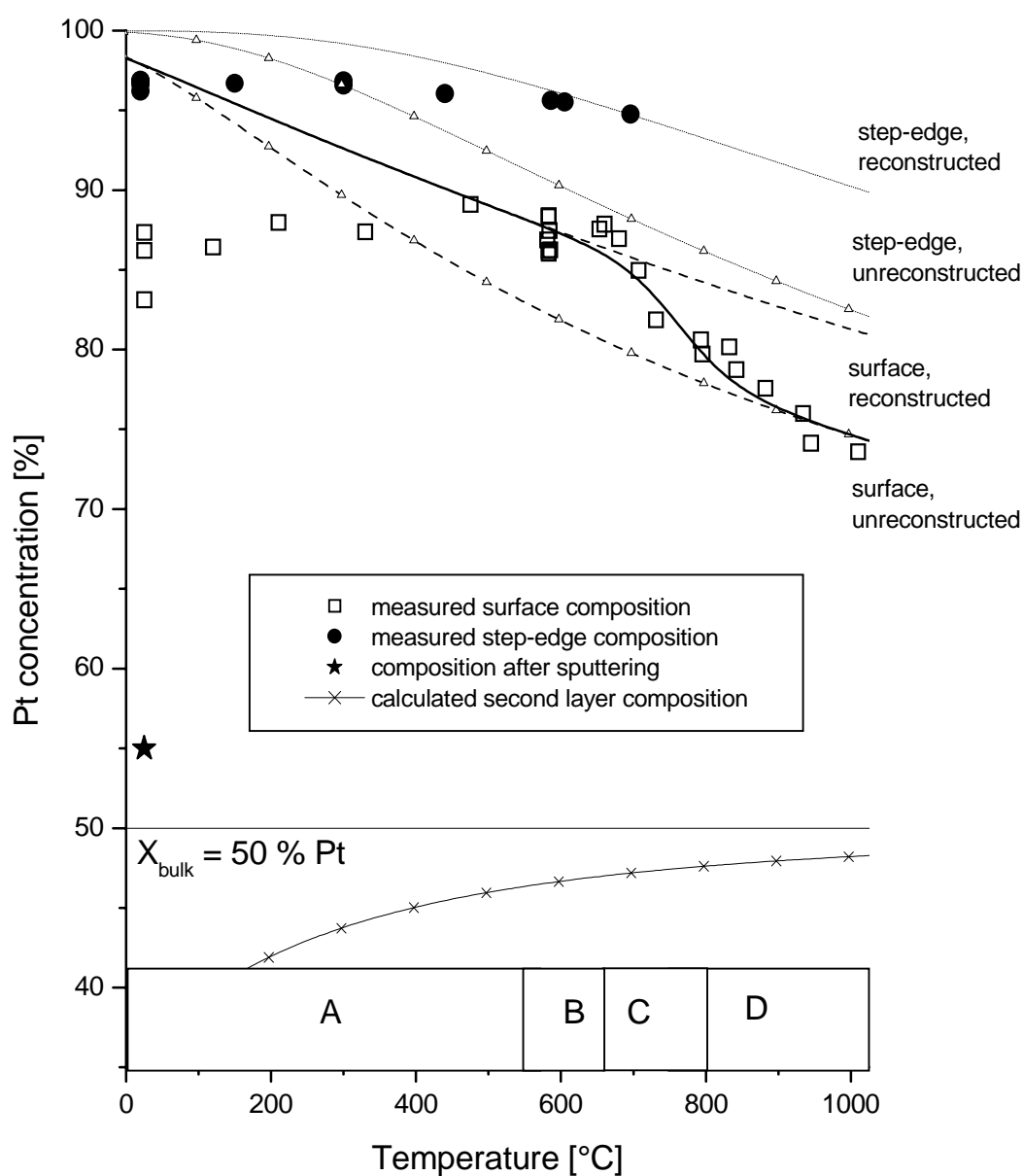
Figure 5.6: *The measured step-edge (solid circles) and the surface composition (open squares) of $Pt_{50}Rh_{50}(511)$ as a function of temperature. The composition after sputtering is indicated by a star. The four temperature regions A-D, as discussed in the text, are indicated. The calculated surface (dashed line) and step-edge (dotted line) compositions of the unreconstructed (valid in region D) surface are indicated by the lines with the triangles. The calculated surface (dashed line) and step-edge (dotted line) compositions of the reconstructed surface (valid in region B) are indicated by the lines without triangles. The calculated surface composition over the whole temperature range, using the transition from a reconstructed to an unreconstructed surface (region C), is indicated by the solid line. The calculated second layer composition is shown by the solid line with crosses.*

with the most pronounced segregation, showing a surface composition of 85 % Pt and a second layer composition of 35 % Pt. The contribution of the second layer to the total scattered yield is equal or less than 4 %. For the measurements with weaker Pt segregation, the error due to the second layer contribution will be smaller. The measured surface composition after sputtering at RT (without annealing) is $X_{surf} = 55 \pm 4$ % Pt (shown in figure 5.6 by the star-symbol). The slight Pt enrichment after sputtering at RT is in agreement with previous studies [7, 21]. After flashing the sample to 1050°C and cooling down to RT, the surface composition is $X_{surf} = 85$ +5/-4 % Pt.

The required time to reach equilibrium depends on the temperature. A series of experiments at 580°C showed an equilibration time constant of about one hour, whereas equilibrium at 1000°C is reached within seconds. The Pt enrichment of the surface decreases with increasing temperature at all temperatures where equilibrium is reached. The Pt step-edge composition starts to decrease with increasing temperature between 600°C and 700°C, indicating that at these temperatures the step edges reach thermodynamic equilibrium. Note that it is likely that the step edges have a larger mobility than the terrace atoms. Therefore the step-edge composition might be expected to be in local equilibrium with the terrace composition, even though the average surface composition may not yet be completely equilibrated below 600°C. Since the step edges consist almost completely of Pt between RT and 600°C, the composition must be close to the equilibrium value. We may find values below 100% Pt at lower temperatures because the terrace atoms cannot reach true equilibrium or due to the contribution of the terrace sites to the total backscattered yield in the used geometry (less than 5%, as discussed in 2.2). Given the surface composition of 85 % Pt and assuming full segregation of Pt to the step-edges, we expect to measure a maximum step-edge composition of $X_{step} = 99$ % Pt.

5.4.2 Composition measurements on $Pt_{50}Rh_{50}(511)$ after O_2 treatment

The oxygen is applied to the above discussed clean and ordered surface, showing a surface Pt concentration of 85 +5/-4 % Pt and a step-edge Pt concentration of 95 +5/-6 % Pt. After preparation of this clean surface by oxygen adsorption and subsequent removal of oxygen by reduction at RT, the surface and the step-edge composition were measured. The oxygen exposure experiments have been performed at various temperatures. However, only the results for oxygen adsorption at 400°C are discussed here. Exposures at lower temperatures had little influence on the composition, which we attribute to insufficient mobility of the atoms. Exposures above 400°C showed essentially the same composition as at 400°C, indicating that during sample cooling to RT (necessary for removal of the oxygen by the reduction treatment) the surface and step-edge composition were frozen around 400°C.
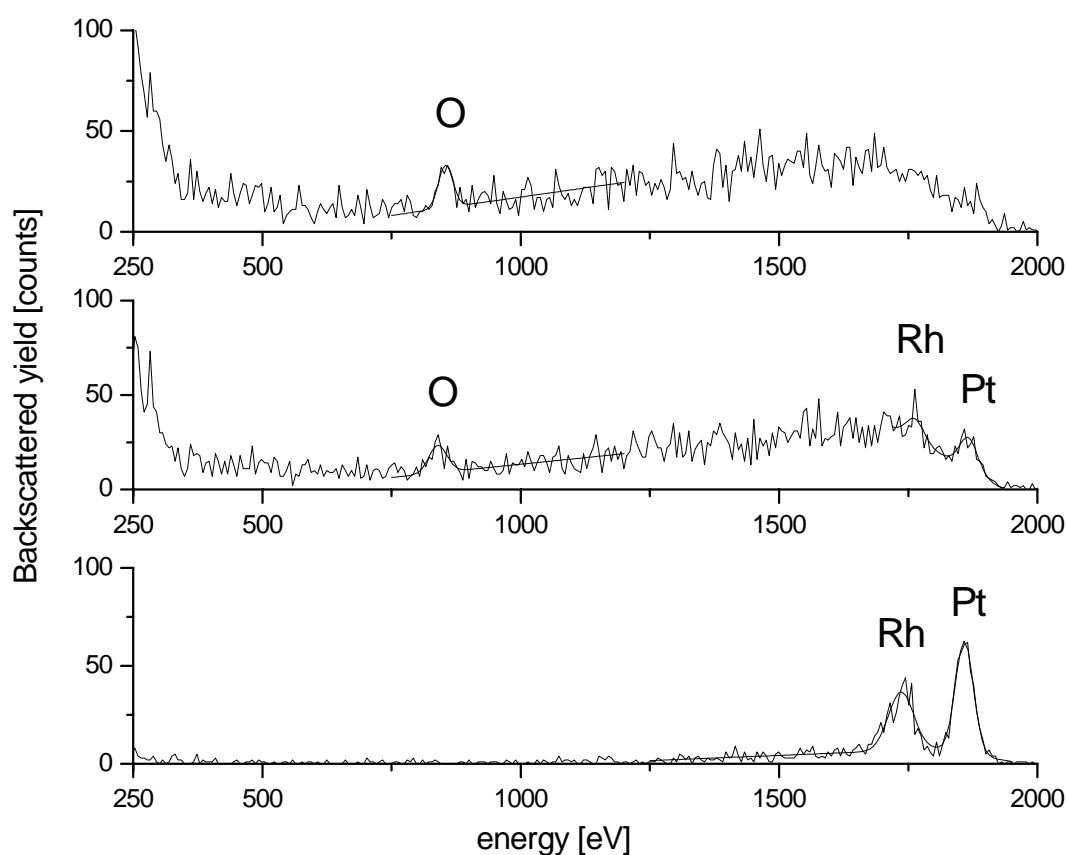
Figure 5.7: *Surface composition measurements with LEIS using 2 keV He^+.*
a) Surface composition measurement after the absorption of oxygen. Only oxygen is visible and a large background is present due to the re-ionisation of projectiles returning from deeper layers.
b) Surface composition measurement after partial reduction of the oxygen treated surface. The oxygen peak has decreased whereas Pt and Rh become visible again. There is still a large background visible.
c) Surface composition measurement after full reduction of the oxygen treated surface. The background and the oxygen are vanished. The Pt/Rh ratio has decreased with respect to the measurements on clean $Pt_{50}Rh_{50}(511)$ (figure 5.4), but is equal to the Pt/Rh ratio of the partially reduced surface as shown in b).

In figure 5.7 the EARISS LEIS spectra, as measured with 2 keV He^+ during the oxygen treatment, are shown to illustrate the changes on the surface. In figure 5.7a the oxygen has just been applied to the surface. The single scattering peaks of Pt and Rh are no longer visible, whereas a peak at 800 eV appears due to scattering of the 2 keV He^+ with oxygen. The background has increased with respect to the clean surface due to re-ionisation of projectiles that return from deeper layers to the detector. Figure 5.7b shows the LEIS spectrum after the surface has been partially reduced. The oxygen peak has decreased while Rh and Pt become visible

again. In figure 5.7c the LEIS spectrum is shown after full reduction of the surface. The strong decrease of the Pt/Rh signal ratio compared to that for the clean surface (figure 5.4) directly indicates that the Pt segregation is strongly reduced, or that possibly segregation of Rh occurs. The fact that the Pt/Rh ratio is almost equal for the partially reduced surface (5.7b) and the fully reduced surface (5.7c) shows that there is only slight preferential shielding of Rh. The vanishing background shows that most of the oxygen has been removed. The efficient removal of the oxygen by the reduction treatment was also confirmed by 2 keV Ar^+ TOF-SARS forward recoiling measurements, which showed that the remaining oxygen coverage was below 0.05 ML. For the final surface composition measurements we again used Ne^+ to minimize the influence of the background.

The measured step-edge and surface compositions of $Pt_{50}Rh_{50}(511)$ after oxygen treatment are presented in table 5.1. The results of four separate measurements are shown, which were obtained on different days. The reproducibility of these measurements is not as good as the segregation measurements on the clean surface. We attribute this to the cooling down procedure, where a different cooling rate can result in a different temperature where the surface composition is frozen. The average final step-edge (47 % $\pm$ 4 % Pt) and surface composition (48 $\pm$ 5% Pt) are below the bulk-composition of $X_{bulk} = 50\%$ Pt. Note, that for each individual experiment the step-edge composition and surface composition are identical, with a much smaller spread than between the experiments. This agrees with the assumption that the spread on the experimental results is caused by the sample preparation rather than by the experimental accuracy. In turn, this suggests that the measurement with the most pronounced Rh enrichment (step-edge: 41 % $\pm$ 6 % Pt, surface: 43 $\pm$ 4% Pt) will be the closest to the actual step-edge and surface composition of the oxidized $Pt_{50}Rh_{50}(511)$ at 400°C.

Table 5.1: *The measured step-edge and surface composition after oxygen treatment at 400°C. The accuracy is the same for all measurements, therefore, it is only mentioned for the first measurement. The number in parenthesis is the systematical error (calibration) part of the given accuracy. The measurements have been sorted by increasing surface Pt concentration.*

Measurement #	X_{Pt} surf (%)	X_{Pt} step-edge (%)
1	43 ± 5 (3)	41 ± 7 (4)
2	45	46
3	48	46
4	54	54

5.5 Discussion

5.5.1 Composition measurements on clean $Pt_{50}Rh_{50}(511)$

For the clean $Pt_{50}Rh_{50}(511)$ surface a strong Pt segregation is found which decreases with increasing temperature. This is comparable to the results of other studies on various PtRh alloys. Auger Electron Spectroscopy (AES) measurements by Van Delft et al. [17] on polycrystalline $Pt_{62}Rh_{38}$ showed about 82 % Pt at the surface upon annealing to 700°C, which is comparable to the surface composition of 84 % Pt as found by AES measurements by Van Langeveld et al. [18] on a polycrystalline sample with the same bulk composition. AES measurements by Siera et al. [19] show a surface composition of 45% Pt for $Pt_{25}Rh_{75}(111)$ and 50% Pt for $Pt_{25}Rh_{75}(100)$. Measurements on a $Pt_{25}Rh_{75}(410)$ crystal by Van Delft et al. [20] with X-Ray Photo-electron Spectroscopy (XPS) and AES showed 45% Pt at 700°C. Beck et al.[21] reported a surface composition of 30% Pt at 700°C on $Pt_{10}Rh_{90}(111)$ using LEIS. A combination of LEIS and quantitative Low Energy Electron Diffraction (LEED) has been used by Platzgummer et al. [22] on $Pt_{25}Rh_{75}(110)$. These measurements showed a transition in the surface structure at 700°C from a (2x1) missing row to a (1x1). The surface composition varied from 80% Pt at 700°C to 48% at 1100°C. Other experiments by Platzgummer et al. [23] on $Pt_{25}Rh_{75}(111)$ and $Pt_{25}Rh_{75}(100)$ showed at 700°C a surface composition of 77% respectively 65% Pt. A wide range of bulk compositions has been measured by T.T. Tsong et al. [24] all showing strong Pt segregation. An overview of these experimentally determined surface compositions at 700°C is given in figure 5.8 by the open squares. The solid curve in figure 5.8 indicates a fit according to the ideal solution model (see e.g. [25]) of all composition values in figure 5.8.

Here, we calculate the surface and step-edge composition using a simple broken bond model, similar to our previous study of the temperature dependent step-edge and terrace segregation of the $Pt_{25}Rh_{75}(410)$ [7] surface. In this model the Gibbs free energy of the crystal is minimized, assuming a random alloy and assuming that atomic bonds are the only contribution to the enthalpy. The crystal is divided into different phases which consist of atoms which are in the same kind of environment (step edges, terrace, second layer, ..., bulk). The Pt concentration of a phase φ, X_φ, can be calculated from the Pt concentration of the bulk, X_b, and the temperature T using:

$$\frac{X_\varphi}{1-X_\varphi} = \frac{X_b}{1-X_b}e^{-\frac{\Delta H_{b\varphi}}{RT}} \quad , \quad \Delta H_{b\varphi} = \frac{\Delta\varepsilon}{2}\left[Z_{bb}-\sum_{i=1}^{N}Z_{i\varphi}\right] - \Omega\left[Z_{bb}(1-2X_b)-\sum_{i=1}^{N}Z_{i\varphi}(1-2X_i)\right] \quad ,(34)$$

with $\Delta\varepsilon = \varepsilon_{PtPt}-\varepsilon_{RhRh}$ the difference between the Pt-Pt and the Rh-Rh bond-energy. The regular solution parameter $\Omega = \varepsilon_{PtRh} - (\varepsilon_{PtPt}+\varepsilon_{RhRh})/2$ is a measure for the energy of mixing. For an ideal solution (Ω=0) the segregation enthalpy for any phase is a function of coordination only. In case of a positive regular solution parameter (Ω>0) the species will tend to cluster (demix). For Ω<0 the species prefer unlike bonds which may ultimately lead to chemical ordering as in the case of Cu_3Au and Pt_3Sn [26]. The number of bonds per atom of phase i to phase φ is given by $Z_{i\varphi}$. This
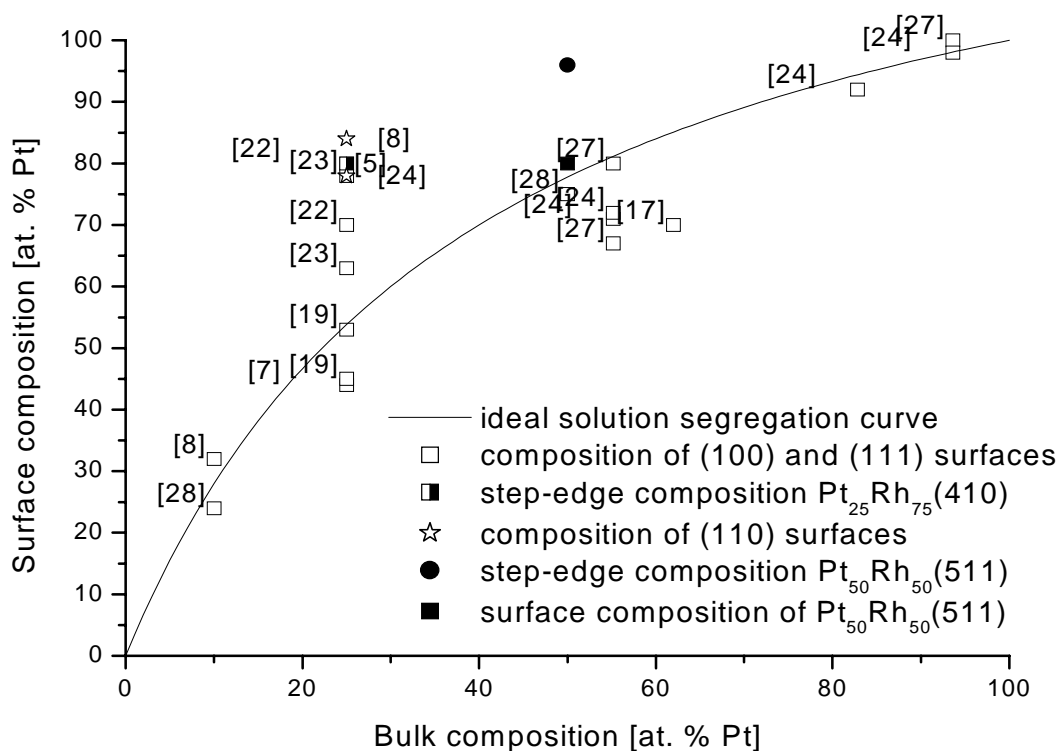
Figure 5.8: *Summary of surface composition versus bulk composition at 700°C. The numbers near the data points correspond to the references in the text. The solid square respectively circle correspond to the measured surface and step-edge composition of $Pt_{50}Rh_{50}(511)$ as presented in this paper.*

can be a fractional number, depending on the used definition of the crystal. If only nearest neighbours are considered, the total number of bonds for an fcc bulk atom is $Z_{bb}=12$. The surface composition has to be calculated from the various phases that contribute to it like the step edge sites and the terrace sites. In our previous work on $Pt_{25}Rh_{75}(410)$ [7] the calculated step-edge Pt concentration was at all temperatures smaller than the measured value when the segregation enthalpy was based exclusively on the number of broken bonds and a constant energy contribution was assumed for all atomic bonds. By using a coordination dependent bond energy (which reflects stronger bonding between the remaining neighbouring atoms when one of the other neighbours is removed) the correct step-edge composition could be obtained. Such a coordination dependent energy contribution to the segregation enthalpy was applied successfully previously by e.g. J. Florencio et al. [27] for PtRh alloys and by Schoeb et al. [28]. Also in the case of Cu_3Au a coordination dependent, or surface specific, energy term has to be used to explain the behaviour of the surface composition as a function of temperature [29, 30]. The same coordination dependent bond energy will be used below to calculate the $Pt_{50}Rh_{50}(511)$ surface and step-edge composition as a function of temperature. Based on the calculations of Schoeb et al. [28], who introduced the surface modified pair potential (SMPP), the bond energies of step-edge atoms will be assumed 10% larger than the bond energies between atoms in the higher

coordinated sites. The value of the regular solution parameter (within reasonable limits for Pt-Rh: -0.2*$|\Delta\varepsilon| < \Omega < 0$) will mainly influence the second layer composition. Therefore its value will be kept fixed in the fitting procedure. This leaves the bond energy difference $\Delta\varepsilon$ as only free parameter. For a regular solution parameter of Ω =-0.4 kJ/mol the surface composition at high temperatures (above 800°C) can be described well by a difference in bond energy of $\Delta\varepsilon$ = 6.1 ± 1.6 kJ/mol. The calculated surface concentration is presented in figure 5.6 by the dashed line with the triangles. The bond energy difference as found for Pt$_{25}$Rh$_{75}$(410) [6] is $\Delta\varepsilon$ = 4.3 ± 1.2 kJ/mol. The fitted values of $\Delta\varepsilon$ for the Pt$_{25}$Rh$_{75}$(410) and the Pt$_{50}$Rh$_{50}$(511) are comparable within the accuracy of the measurements. This shows that the different structure and the different bulk compositions have no major influence on the bond energy difference at the surface.

The calculated surface composition at high temperatures is in good agreement with the measured surface composition. However, at temperatures below 800 °C the measured surface Pt concentration is much larger than the calculated value. Fitting of the low temperature measurements is not possible due to the rapid change in Pt surface concentration between 650°C and 800°C (this rapid decrease between 650°C and 800°C is reproducible and cannot be attributed to experimental errors). When using an extremely large regular solution parameter ($\Delta\varepsilon$=3.1 kJ/mol, Ω = 1.5 kJ/mol), the surface composition can be fitted well over the whole temperature range. Such a large value for the regular solution parameter would also cause bulk demixing. Raub [31] indeed suggested the existence of such a miscibility gap with an upper critical demixing temperature of about 760°C and Lakis et al. [32] recently observed it in an 'indirect' way with analytical electron microscopy on alumina-supported Pt-Rh catalyst particles. What would cause such a phase separation is not clear at present, but a similar behaviour is also experimentally observed for the neighbouring systems Pt-Ir and Pt-Au [33]. Bulk demixing could possibly explain the rapid change in surface composition with decreasing temperature as observed in the experiments. When phase separation occurs, the Pt rich phase (lowest surface energy) will be situated at the outside region of the sample as in a 'cherry-like' configuration resulting in a Pt-rich surface. This Pt-enrichment becomes even more pronounced when the contour of the two phase region is followed at lower temperatures. This in turn explains the sigmoidal kink in the experimental curve where the jump occurs (between 700°C and 800°C) at the same temperature as the upper critical demixing temperature (760°C). More elaborate simulations will be undertaken by Helfensteyn et al. to further investigate this possibility [34].

Another possible explanation is suggested by the results of Platzgummer et al. [21], who observed a similar rapid increase in Pt enrichment with decreasing temperature on Pt$_{25}$Rh$_{75}$(110). This jump in surface composition was caused by a (2x1) to (1x1) phase transition between 500°C and 800°C. The temperature range for this transition is the same as observed in our experiments on the Pt$_{50}$Rh$_{50}$(511) crystal. The (2x1) phase of the (110) surface is a missing row reconstructed surface, which results in (111) facets. Similar narrow (111) facets are formed on the (511) surface when removing a row of atoms on the center of the terraces, parallel to the step edges. Based only on the number of broken bonds, the creation of such structure would be considerably endothermic and thus not be favored. However, other energy contributions like e.g. the step-step interaction (which can be large due to the very small terraces of the (511) crystal), may result in

the above mentioned surface reconstruction at temperatures below 650°C anyway.

Indications of such a structural transition is found in the total LEIS signal. Platzgummer et al. observed the phase transition directly in LEED experiments and found an accompanying increase of the total LEIS signal. In our case, a similar increase in the total LEIS signal has been observed. At temperatures above 800°C the total scattered yield is 25 % larger than at temperatures below 650°C. It should be noted that the change in LEIS signal observed here is significantly smaller than the 100% increase as observed for the $Pt_{25}Rh_{75}(110)$ [21]. This is due to the different experimental setup. In the experiments of Platzgummer et al. a shadowing and blocking configuration was used to ensure surface sensitivity limited to the outermost layer only. In this case the total ion yield is directly proportional to the total number of atoms in that plane, which is twice as large for the (1x1) phase as compared to the (2x1) phase. In our setup the surface sensitivity is guaranteed by the use of an electrostatic analyser and therefore no special scattering geometry was used. An estimation of the change in total ion yield can be made by counting the number of atoms at the surface and determining the range of azimuthal directions for which the ions can reach the detector without skimming other atoms (which would lead to neutralization of the ion). For a close packed surface (like the terraces of the unreconstructed (511) surface) the signal is determined almost completely by the outermost atomic layer. After removal of the central atomic row the (former) second layer atoms will contribute to the surface and hence to the LEIS signal. The projectiles returning from those atoms have to pass the step-edges in two directions on the way to the detector. Therefore the sensitivity for these atoms is about a quarter with respect to the sensitivity for the previous terrace atoms. This results in a moderate decrease in scattered yield in case of a missing row reconstruction, which will be estimated below. The unreconstructed (511) surface has two atoms per terrace that contribute over all azimuthal directions and one atom that contributes over half the azimuthal range. The reconstructed surface has one atom per terrace that contributes over all azimuths (the step edge atom), one atom that contributes over half the azimuthal range (the atom below the step edge atom) and two atoms that contribute over a quarter (the former second layer atoms). A difference of about 20 % in total ion yield between the reconstructed and unreconstructed is thus estimated. A more accurate estimate, based on azimuthal ion scattering data from relatively open crystals like Pt(110) and Pd(110), shows the same increase in total yield in case of the transition from a missing row reconstructed surface to a unreconstructed surface. The observed difference in the total ion yield of about 25% agrees well with the expected difference in total ion yield. The strong increase in the surface Pt concentration of the reconstructed surface is caused by the increased number of missing neighbours of the step-edge atoms in combination with the increased relative contribution of the step-edges to the total yield (the exposure of the atoms with a larger number of missing neighbours increases while the exposure of the atoms with a reduced number of missing neighbours decreases).

In figure 5.6 the step-edge and surface compositions are presented for a reconstructed $Pt_{50}Rh_{50}(511)$ surface (with the central rows of atoms in the terrace missing), using equation (34) and the values for $\Delta\varepsilon$ and Ω as found for the high temperatures data on the unreconstructed surface. The surface composition is indicated by the dashed line without triangles, the step-edge

composition is indicated by the dotted line without triangles. The result shows good agreement with the measured surface composition. The surface composition between 650°C and 800°C is calculated by introducing a transition between the calculated surface composition of the unreconstructed surface (dashed line with triangles) and the calculated surface composition of the reconstructed surface (dashed line without triangles) based on the total ion yield (the relative contribution of both phases to the surface composition is set equal to the relative contribution of both phases to the total ion yield). The resulting surface composition is shown in figure 5.6 by the thick solid line and agrees well with the measurements.

Ion trajectory simulations have been performed for the missing row reconstructed surface. The results look very similar to the results of the unreconstructed surface, especially near the scattering geometry where the step-edge composition is measured. This is due to the fact that the missing rows are shadowed by the step-edge atoms at this geometry anyway (see figure 5.1 and figure 5.2). For the step-edge composition measurements it is thus not important whether the $Pt_{50}Rh_{50}(511)$ has a missing row reconstruction or not. The step-edge composition can therefore be determined using the same method over the whole temperature range. The calculated step-edge Pt concentration for a reconstructed surface (dotted line without triangles) is larger than the calculated step-edge Pt concentration for the unreconstructed surface (dotted line with triangles). This is due to the difference in coordination between the step-edge atoms of the reconstructed surface (6) and the unreconstructed surface (7). It is also clear that a missing row reconstructed surface yields calculated values for the step-edge composition which are much closer to the measured step-edge composition than when assuming an unreconstructed surface. The step-edge composition measurements could not be performed at higher temperatures than 700°C, which prevents the observation of the transition between the reconstructed to the unreconstructed surface in the step-edge composition results.

In conclusion, several temperature regions there have been identified for the $Pt_{50}Rh_{50}(511)$ crystal (see figure 5.6). The temperature in the first region (figure 5.6, indicated by "A"), between room temperature and about 550°C, is too low to reach equilibrium within a reasonable period of time. In this temperature range the measured surface composition and the measured step-edge composition remain constant with temperature. Between 550°C and 650°C (indicated by "B") the step-edges and surface can reach equilibrium within one hour and the composition becomes dependent on the temperature. Only a minor decrease in the Pt concentration with increasing temperature is visible. The next region is 650°C to 800°C (indicated by "C"). Here a large jump in the surface composition occurs which cannot be explained by the used segregation model. A possible cause is a bulk phase separation, with the Pt-rich phase at the outside, from which Pt segregation occurs. An alternative cause is the transition from a missing row reconstructed surface to an unreconstructed surface. In the last region, corresponding to temperatures above 800°C (indicated by "D"), a slow decrease in Pt segregation with increasing temperature is observed. This region shows the expected segregation curve for an unreconstructed $Pt_{50}Rh_{50}(511)$ surface for segregation driving energies similar to those previously found for $Pt_{25}Rh_{75}(410)$ [6]. The assumption that reconstruction of $Pt_{50}Rh_{50}(511)$ occurs can be checked by STM at room temperature, in which case the reconstructed surface should be observed. The assumption that

$Pt_{50}Rh_{50}(511)$ shows phase-separation can be checked by measuring the second layer composition, which should show Pt segregation.

5.5.2 Composition measurements on $Pt_{50}Rh_{50}(511)$ after O_2 treatment

Before the discussion of the results on the compositions measurements, we will address some issues which might limit the accuracy of our experiments. Our measurements of the surface and step-edge compositions on the oxygen treated surface rely on the assumption that reduction by hydrogen at room temperature does not change the composition. This seems reasonable since a temperature of more than 500°C is needed to reach equilibrium of the clean $Pt_{50}Rh_{50}(511)$ surface. Hydrogen can decrease the temperature at which equilibrium can be reached [35], however, it is unlikely that it can lower the temperature by more than 400°C. In order to verify whether the presence of hydrogen induces significant mobility at room temperature we have measured the surface composition of the sputtered $Pt_{50}Rh_{50}(511)$ surface before and after hydrogen treatment (54% Pt). No difference was observed, which confirms that reduction at room temperature does not influence the surface composition.

Another possible issue concerns the formation of new structures on PtRh alloys upon oxidation, like e.g. the p(3x1) phase on $Pt_{25}Rh_{75}(100)$ and $Pt_{50}Rh_{50}(100)$ [36 - 40]. However, these reconstructions disappear after reduction at room temperature and will therefore not influence our composition measurements.

Finally the measurements might be influenced by a small amount of oxygen which remains at the surface after reduction. If oxygen selectively screens Pt or Rh the measured composition will be incorrect. The maximum error in the measured composition equals the oxygen screened part of the surface, which is at most 5 %. The Pt/Rh ratio of the fully reduced surface (figure 5.7c) almost equals the Pt/Rh ratio of the partially reduced surface (figure 5.7b). This shows that there is only a slight preferential shielding of Rh by the oxygen. Consequently the error due to shielding by the remaining oxygen will be much smaller than the maximum value of 5% as calculated above. In case the remaining oxygen would selectively screen the step edges, the error in the measured step-edge composition could be much larger (up to 20%). To test the preferential adsorption of oxygen atoms at the step-edges we carried out angle-dependent TOF-SARS experiments using 3 keV Ar^+ ions. These measurements should show a strong azimuthal dependency in case of preferential oxygen sites at the step-edges. The ratio between the oxygen and the Pt plus Rh recoils was found to be independent of the azimuth, ruling out strong preferential adsorption at the step edges. As for the terraces, the error due to screening by remaining oxygen is thus negligible.

Only few previous studies on the surface composition of PtRh alloys in an oxidizing environment have been published, all of which indicate a moderate Pt depletion. Sporn et al. [40] performed quantitative LEED measurements on oxidized $Pt_{25}Rh_{75}(100)$, and found a surface composition of 10 ± 32 % Pt during oxidation and 16 ± 25% Pt after reduction at room temperature. Composition measurements with LEIS on $Pt_{10}Rh_{90}(100)$ by Beck et al. [8] yielded

a surface composition of 6% Pt after NO adsorption. Our experiments show weak Rh segregation of $Pt_{50}Rh_{50}(511)$ after oxygen treatment. The measurements presented in table 5.1 show an average surface composition of 48 ± 4 % Pt and an average step edge composition of 47 ± 5 % Pt. For each measurement the surface and step-edge compositions are nearly equal, indicating that the (larger) spread in the measured compositions is due to variations in the preparation of the sample. The most probable causes are variations in the partial pressures of O_2 and H_2 and the temperature of the sample during the oxygen treatment. This suggests that the results of the measurements with the most pronounced Rh segregation, showing a step-edge of 41 % ± 6 % Pt and a surface composition of 43 ± 4% Pt, are closest to the actual composition.

In section 4.1 the segregation for the clean $Pt_{50}Rh_{50}(511)$ surface was calculated using equation (34). It was concluded that $Pt_{50}Rh_{50}(511)$ is very similar to an ideal solution ($\Omega \approx 0$). The segregation enthalpy can thus be approximated by the number of broken bonds times the energy difference between the Pt-Pt and the Rh-Rh bonds. For the oxygen covered surface the same approach can be used based on equation (34), where the broken bonds have to be replaced by bonds with oxygen. We observe no significant segregation on the oxidized surface, which implies that the Pt-O and Rh-O bond energies must be nearly equal. Therefore the number of bonds with the oxygen will have a reduced influence on the segregation, which also explains the almost equal Pt concentrations of the terraces and the step edges.

5.6 Conclusions

At all temperatures a strong Pt segregation is observed to the surface and to the step edges of clean $Pt_{50}Rh_{50}(511)$. The segregation to the step edges is larger than to the terraces, which is caused by the lower coordination of the step-edge atoms. The surface composition has been calculated using a simple broken bond model, considering only nearest neighbour interactions. For temperatures above 800°C, the surface composition of $Pt_{50}Rh_{50}(511)$ can be described well by this model. Below this temperature, however, a larger Pt segregation to the surface and step-edges is observed than calculated. Furthermore, there is an increase in total ion yield between 650°C and 800°C. The increase in total ion yield and the jump in the surface composition can be explained by assuming a missing row reconstruction below 650°C and a smooth transition to an unreconstructed $Pt_{50}Rh_{50}(511)$ surface above 800°C. However, an equally acceptable explanation of the enhanced segregation at temperatures below 650°C is a bulk phase separation with the Pt-rich phase on the outside. From which the Pt segregation occurs.

Oxidized $Pt_{50}Rh_{50}(511)$ shows weak Rh segregation instead of strong Pt segregation. The step-edge and the surface Pt concentrations become equal due to the reduced segregation driving force. The differences in catalytic behaviour of stepped versus "flat" PtRh alloys towards NO and CO as well as the extreme activity of $Pt_{25}Rh_{75}(410)$ should therefore be attributed to the structure only.

References:

1. B.E. Nieuwenhuys, J. Siera, K-I. Tanaka, H. Hirano, ACS. Symp. Series. 552; Environmental Catalysis, ACS, Washington DC, 1994

2. B.E. Nieuwenhuys, Advances Catal. 44 (1999) 259

3. P.T. Wouda, B.E. Nieuwenhuys, M. Schmid, P. Varga, Surf. Sci. 359 (1996) 17

4. S. Helfensteyn, C. Creemers, Surf. Sci. 507 (2002) 783

5. E.L.D. Hebenstreit, W. Hebenstreit, M. Schmid, P. Varga, Surf. Sci. 441 (1999) 441

6. M. Aono, M. Katayama, E. Nomura, T. Chassé, D. Choi, M. Kato, Nuclear Instruments and Meth. in Phys. Research B37/38 (1989) 264

7. B. Moest, P.T. Wouda, A.W. Denier van der Gon, M.C. Langelaar, H.H. Brongersma, B.E. Nieuwenhuys, D.O. Boerma, Surf. Sci. 473 (2001) 159 (chapter 4 of this thesis)

8. D.D. Beck, G.L. Dimaggio, G.B. Fisher, Surf. Sci. 297 (1993) 303

9. W. Athenstaedt, M. Leisch, Appl. Surf. Sci. 94/95 (1996) 403

10. M. Henzler, Surf. Sci. 22 (1970) 12

11. W. Ceelen, Structure and Morphology of thin metallic overlayers, Eindhoven, 1997 ISBN 90-386-0577-3

12. G. Helling, M.O. Ottevanger, S.W. Boelens, C.L.C.M. Knibbeler, H.H. Brongersma, Surf. Sci. 162 (1985) 913

13. M.H. Langelaar, M. Breeman, A.V. Mijiritskii, D.O. Boerma, Nucl. Instrum. Meth. Phys. Res. B (1997) 587

14. J.P. Biersack, L.G. Haggman, Nucl. Instr. Meth. 174 (1980) 257

15. J.F. Ziegler, J.P. Biersack, U. Littmark, The stopping and range of ions in solids, Pergamon, New York (1985)

16. H.H. Brongersma, P.M. Mul, Surf. Sci. 35 (1973) 393

17. F.C.M.J.M. van Delft, A.D. van Langeveld, B.E. Nieuwenhuys, Surf. Sci. 189/190 (1987) 1129

18. A.D. van Langeveld, J.W. Niemandsverdriet, Surf. Sci. 178 (1986) 880

19. J. Siera, F.C.M.J.M. van Delft, A.D. van Langeveld, B.E. Nieuwenhuys, Surf. Sci. 264 (1992) 435

20. F.C.M.J.M. van Delft, J. Siera, B.E. Nieuwenhuys, Surf. Sci. 208 (1989) 365

21. D.D. Beck, G.G. DiMaggio, G.B. Fisher, Surf. Sci. 297 (1993) 293

22. E. Platzgummer, M. Sporn, R. Koller, M. Schmid, W. Hofer, P. Varga, Surf. Sci. 423 (1999) 134

23. E. Platzgummer, M. Sporn, R. Koller, S. Forsthuber, M. Schmid, W. Hofer. P. Varga,

Surf. Sci. 419 (1999) 236

24. T.T. Tsong, D.M. Ren, M. Ahmad, Phys. Rev. B. 38 (1988) 7428

25. J. Du Plessis, Surface segregation, Solid State Phenomena vol. 11, Sci-Tech Publications, ISBN: 3-908044-06-5, Vaduz Lichtenstein 1990

26. M.A. Vasiliev, J. Phys. D 30 (1997) 3037

27. J. Florencio, D.M. Ren, T.T. Tsong, Surf. Sci. 345 (1996) L29

28. A.M. Schoeb, T.J. Raeker, L. Yang, X. Wu, T.S. King, A.E. DePristo, Surf. Sci. 278 (1992) L125

29. J.M. Sanchez, J.L. Morán-López, Phys. Rev. B 32 (1985) 3534

30. B. Moest, A.W. Denier van der Gon, H.H. Brongersma, Surf. Sci., to be published

31. E. Raub, J. Less Com. Met. 1 (1959) 3.

32. R.E. Lakis, C.E. Lyman and H.G. Strenger Jr., J. Catal. 154 (1995) 261.

33. T.B. Massalski, Binary alloy phase diagrams, ASM International, Materials Park, Ohio (1990) ISBN 0-87170-261-4.

34. S. Helfensteyn, C. Creemers, to be published

35. L.C.A. van den Oetelaar, O.W. Nooij, S. Oerlemans, A.W. Denier van der Gon, H.H. Brongersma, L. Lefferts, A.G. Roosenbrand, J.A.R. van Veen, J. Phys. Chem. B 102 (1998) 3445

36. H. Hirano, T. Yamada, K-I Tanaka, J. Siera, B.E. Nieuwenhuys, Surf. Sci. 222 (1989) L804

37. Y. Matsumoto, Y. Okawa, T. Fujita, K.I. Tanaka, Surf. Sci. 355 (1996) 109

38. Y. Matsumoto, Y. Aibara, K. Mukai, K. Moriwaki, Y. Okawa, B.E. Nieuwenhuys, K.I. Tanaka, Surf. Sci. 377 (1997) 32

39. K.I. Tanaka, Surf. Sci. 357 (1996) 721

40. M. Sporn, E. Platzgummer, E.L.D. Gruber, M. Schmid, W. Hofer, P. Varga, Surf. Sci. 416 (1998) 384

The step-edge and surface composition of $Cu_3Au(17,1,1)$ near the order-disorder transition

<div align="right">

6

</div>

6.1 Abstract

The temperature dependent surface and step-edge compositions of $Cu_3Au(17,1,1)$ have been measured between room temperature and 980°C using Low Energy Ion Scattering (LEIS). Below the ordering temperature of $T_o = 390$°C we observe a constant surface Au concentration that is smaller than the surface Au concentration of $Cu_3Au(100)$. The terrace and step-edge compositions of $Cu_3Au(17,1,1)$ are the same within the measurement accuracy. Above the ordering temperature the surface Au concentration slowly decreases with increasing temperature, whereas the step-edge Au concentration shows a small increase over the observed temperature range. Above T_o the Au segregation is no longer inhibited by the interplay between ordering and the specific structure of $Cu_3Au(17,1,1)$. As a result the Au surface concentration of $Cu_3Au(17,1,1)$ approaches that of $Cu_3Au(100)$.

Spot Profile Analysis - Low Energy Electron Diffraction (SPA-LEED) measurements below the order-disorder transition show an average terrace width of 52 ± 4 Å. These measurements agree with Atomic Force Microscope (AFM) measurements in air and at room temperature which show 50 ± 5 Å wide terraces that are separated by straight step-edges along the <011>. Based on these measurements and the close similarity with $Cu_3Au(12,1,1)$ it was suggested that $Cu_3Au(17,1,1)$ has paired steps below the order-disorder temperature. The step-edge and surface compositions have been calculated for a $Cu_3Au(17,1,1)$ crystal with paired steps as a function of the temperature using Monte Carlo simulations. The calculated surface composition shows good agreement with the LEIS measurements over the whole temperature range. The calculated step-edge composition shows a small increase in the Au concentration below the ordering temperature. The step-edge composition measurements and simulations suggest that the chemical ordering below the ordering temperature inhibits stronger segregation of Au to the step-edges.

6.2 Introduction and method

The surface composition of alloys is generally different from the bulk composition due to segregation. Many applications (catalysts, cathodes, thin film substrates) and material properties (like e.g. friction) depend on the surface properties. Therefore it is important to know the morphology and composition of the surface under various conditions. Chemically ordered alloys are very interesting in this aspect since there is an interplay, or even competition, between segregation to the surface and the continuation of the bulk-ordering. The surface of clean Cu_3Au, one of the most studied alloys in this respect, unexceptionally shows Cu-Au termination in favour of the completely Cu terminated surface.

The Cu_3Au bulk shows a transition from the $L1_2$ ordered phase (see figure 6.1a) to a disordered phase at $T_o = 390°C$ [1]. In the case of $Cu_3Au(100)$ a simple truncation of the bulk could lead either to Cu-Au or fully Cu terminated surfaces. From the measurements of Buck et al. [2], using Low Energy Ion Scattering (LEIS), it was concluded that the $Cu_3Au(100)$ surface exclusively shows Cu-Au termination. These results have been confirmed by numerous other authors (see for a review e.g. [3]). Besides LEIS other techniques like Auger Electron Spectroscopy (AES) [4] and X-Ray scattering [5] have been used to study the composition of the $Cu_3Au(100)$ surface. In all cases gold enrichment of the first layer is observed. Composition measurements on Cu-Au alloys have also been performed for different bulk compositions [6], other low index planes [7] and poly-crystalline samples [8, 9]. All of these studies point to a strong gold enrichment of the first layer. One exception to the generally observed Au enrichment, most probable caused by sulphur contamination, is presented in [10].

The structure of the $Cu_3Au(100)$ surface has also extensively been studied. Several techniques have been used like Low Energy Electron Diffraction (LEED) [11, 12], Scanning Tunneling Microscopy (STM) [13] and X-Ray scattering [14, 15]. The LEED and X-Ray scattering studies show that the long range order (LRO) of the surface starts to decrease at a temperature slightly below the bulk transition temperature T_o. The order-disorder transition is continuous (or second order) at the surface, whereas the bulk has an abrupt (or first order) transition. This is occasionally referred to as wetting. Both the measured surface composition and the LRO can be satisfactory reproduced by cluster calculations [16], especially if a surface specific energy term is included [17, 18] which represents the modified atomic bonds at the surface (e.g. due to relaxation). Other techniques like Monte Carlo simulations [19, 20] primarily focus on extracting the composition information as a function of temperature and/or layer depth.
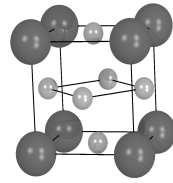
In this paper we present surface and step-edge composition measurements on a vicinal Cu_3Au single crystal below and above the ordering temperature. In the case of random alloys, like $Pt_{25}Rh_{75}(410)$ [21], the lower coordination of step-edge atoms will generally lead to enhanced segregation. However, for ordered alloys like Cu_3Au there is a strong competition between ordering and segregation which will both be enhanced by the lower coordination of the step-edge atoms. Here subtle effects, like the coordination dependency of the bond energies, may shift the wage between ordering and segregation. A lot can thus be learned from the basics of

segregation by measuring the temperature dependent step-edge and surface composition of a vicinal crystal that exhibits bulk ordering like Cu_3Au.

The $Cu_3Au(17,1,1)$ crystal has been selected for several reasons. First of all, extensive studies have been performed on the low index crystal $Cu_3Au(100)$ [2, 5, 14, 16, 17, 22], which is similar to the terraces of the $Cu_3Au(17,1,1)$ crystal, providing a good reference to our measurements. Furthermore the surface of $Cu_3Au(100)$ shows incomplete segregation, which enables possible enhanced segregation to the step-edges due to the lower coordination of these atoms. The (17,1,1) orientation has been chosen because various authors report ragged step-edges along the <001> and straight step-edges along the <011> on $Cu_3Au(100)$ [22, 23]. This is attributed to the stronger interaction between the step-edge atoms along the <011> (nearest neighbours) with respect to the step-edge atoms along the <001> (next nearest neighbours). Stable step-edges will probably result in a better defined average terrace width. Publications about structure measurements on $Cu_3Au(100)$ below the ordering temperature report respectively double atomic height steps [22], combinations of single and double atomic height steps [23] and paired steps [24, 25]. Here paired steps refer to the specific combination of double atomic height steps and single atomic height steps separated by a short terrace as shown in figure 6.1. A relatively large terrace width has been chosen to increase the chance on single atomic height steps. Single atomic height steps are expected to introduce a strong competition between Cu-Au and bulk-like termination at the surface that vanishes near the order-disorder temperature. The introduction of single atomic height steps would thus enhance the expected effects near the order-disorder temperature. However, the terraces should be short enough to provide sufficient step-edges for the composition measurements. Of all publications about the structure of Cu_3Au below the order-disorder transition, the $Cu_3Au(12,1,1)$ and $Cu_3Au(13,1,1)$ as used by Le Goff et al. [25] show the closest similarity with $Cu_3Au(17,1,1)$. On $Cu_3Au(12,1,1)$ and $Cu_3Au(13,1,1)$ paired steps are reported. Therefore it is expected that $Cu_3Au(17,1,1)$ will either show paired steps or, due to the wider terraces, single atomic height steps.
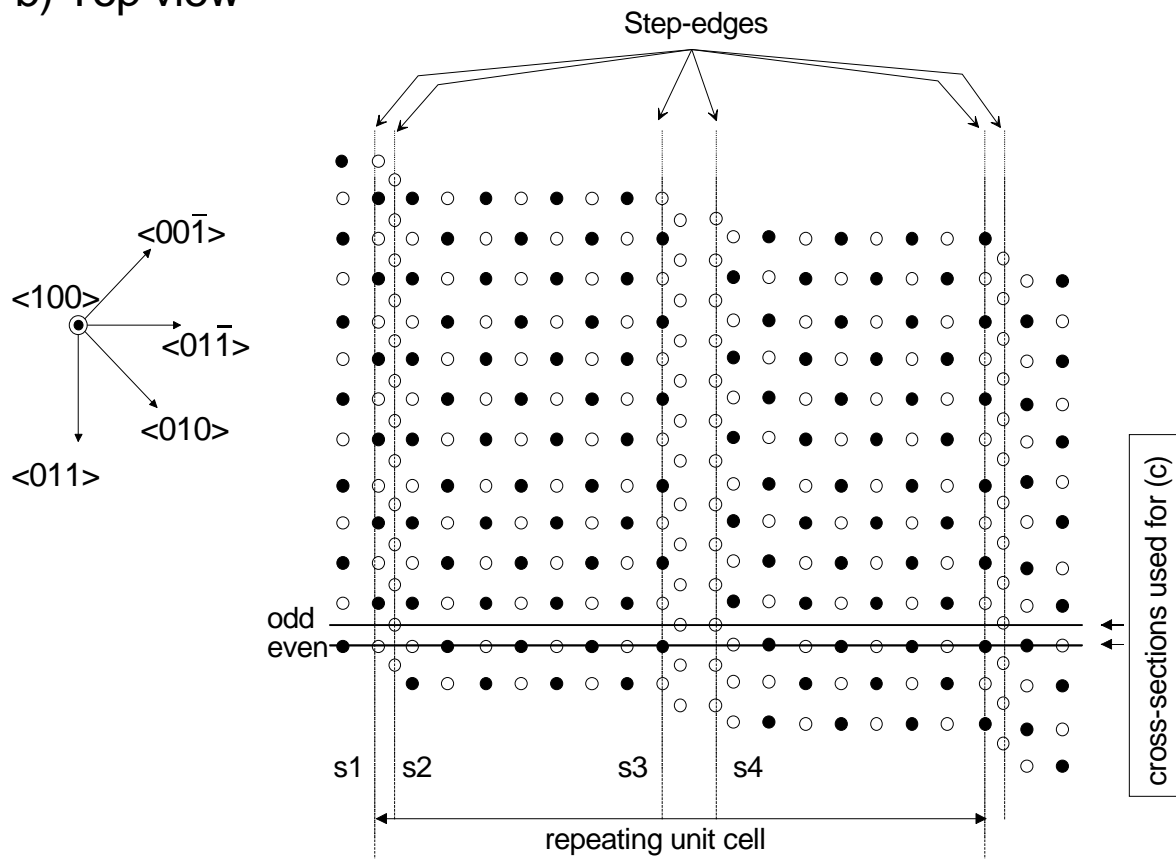
In figure 6.1 the schematic representation of the $Cu_3Au(17,1,1)$ crystal is presented in the top view (figure 6.1b) and side view (figure 6.1c), assuming simple bulk truncation and paired steps. The side view shows a compound picture of two successive cross sections (indicated by "odd" and "even") of $Cu_3Au(17,1,1)$ perpendicular to the step edges. The crystal consists of alternating "odd" and "even" layers. The atoms that belong to the "even" cross section are connected by lines in the side view (figure 6.1c). As can be seen from the side view, the uppermost atoms belong alternatively to the "odd" or "even" layer. This is illustrated more clearly in the top view of figure 6.1b which shows only the topmost atoms, and therefore shows the alternating atomic layers. The following definitions will be used: the terrace atoms are those atoms in figure 6.1 that have 8 or 10 nearest neighbours. The step-edge atoms are those atoms that have 7 (step-edges s1, s3 and s4 in figure 6.1) or 9 (step-edge s2 in figure 6.1) nearest neighbours. The surface consists of all step-edge atoms and terrace atoms together. In this chapter paired steps are defined by the combination of double atomic height steps (s1 and s2) and an equal amount of single atomic height steps that are separated by a very short terrace (s3 and s4). The terrace atoms with 2 missing neighbours are positioned just below the step-edge atoms.

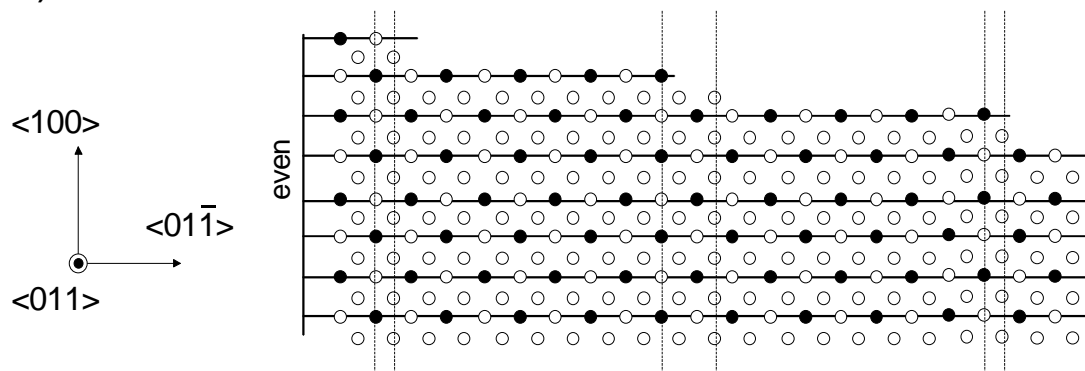a) L1$_2$ arrangement of Cu$_3$Au

○ Cu
● Au

b) Top view

Step-edges

<00$\bar{1}$>
<100>
<01$\bar{1}$>
<010>
<011>

odd
even

cross-sections used for (c)

s1   s2   s3   s4

repeating unit cell

c) Side view

<100>
<01$\bar{1}$>
<011>

even

Figure 6.1: *a) The schematic representation of the L1$_2$ structure b) Top and c) side view of the Cu$_3$Au(17,1,1) surface structure, assuming step-pairing and simple truncation of the ordered bulk. A detailed description of the figures is presented in the text.*

Projectiles returning from those atoms or from the atoms in step-edge s2 have a larger chance on neutralization than the projectiles returning from the terrace atoms with 4 missing neighbours (which are not shielded by the step-edge atoms). In the case of surface composition measurements with an electrostatic analyser, the relative contribution of the terrace atoms with 2 missing neighbours will therefore be smaller than the relative contribution of the terrace atoms with 4 missing neighbours and the step-edge atoms.

The morphology of the $Cu_3Au(17,1,1)$ surface has been studied with Spot Profile Analysing - Low Energy Electron Diffraction (SPA-LEED) and Atomic Force Microscopy (AFM). The positions of the LEED spots contain information on the surface structure and lattice size whereas the spots themselves contain information about the average domain size, step-height, terrace width and mosaicity of the crystal. See [26, 27] for more details on SPA-LEED. The composition of the surface and the step-edges has been measured with Low Energy Ion Scattering (LEIS). LEIS is a quantitative technique that can be used with extreme sensitivity to determine the composition of the outermost layers [28]. A detailed description of the LEIS technique is provided in reference [29]. The technique can also be used for site-selective measurements of the step-edge composition, as discussed in the previous chapters, by performing backscattering Time Of Flight (TOF) measurements at glancing angles of incidence.

6.3 Experimental

The Cu_3Au sample was oriented in-situ by Laue diffraction and cut within $0.1°$ of the (17,1,1), the final polishing step was carried out with a roughness below 0.05 μm [30]. See figure 6.3 for the Laue picture after cutting and polishing of the sample. The sample is mounted on a titanium sample holder by tantalum wires through spark-cut trenches at the sides of the crystal to avoid any foreign objects on the surface of the sample. The sample was initially cleaned by repeated cycles of sputtering with 2 keV Ar^+ at various temperatures and analyzed with Auger Electron Spectroscopy (AES) until impurities like oxygen and carbon were below the detection limit (~0.01 ML). After this procedure the sample is routinely sputtered at 550°C with 2 keV Ar^+ during the night, annealed up to 950°C to reconstruct the surface and then slowly cooled to the desired temperature to restore the chemical ordering. The temperature of the sample is measured by an Impac IP 120 pyrometer with a reproducibility of $\pm1°$C over the measuring range of 160°C-1250°C. However, the factory supplied emissivity for polished Cu/Au samples of $\varepsilon=0.05$ is below the minimum usable limit of $\varepsilon = 0.1$ of the pyrometer which will result in a measurement error. All temperatures presented in this paper are corrected for this error (the actual value is twenty percent larger that the measured value), based on the measured temperature where the order-disorder transition is observed.

The morphology of the sample has been checked in a setup providing AES and SPA-LEED, which has been described in detail elsewhere [31]. After the above described cleaning/surface reconstruction routine, a sharp c(2x2) LEED pattern is measured at room temperature (RT) on a low background. This indicates a well ordered surface (see figure 6.2). At RT the width of the (0,0) spot has been measured as a function of the electron-beam energy

between 40 eV and 170 eV to determine the mosaicity, the average domain size and the step-height between the terraces of the $Cu_3Au(17,1,1)$ surface. The same measurements have been performed above the phase transition, but for fewer electron energies because of the intensity loss at elevated sample temperatures.
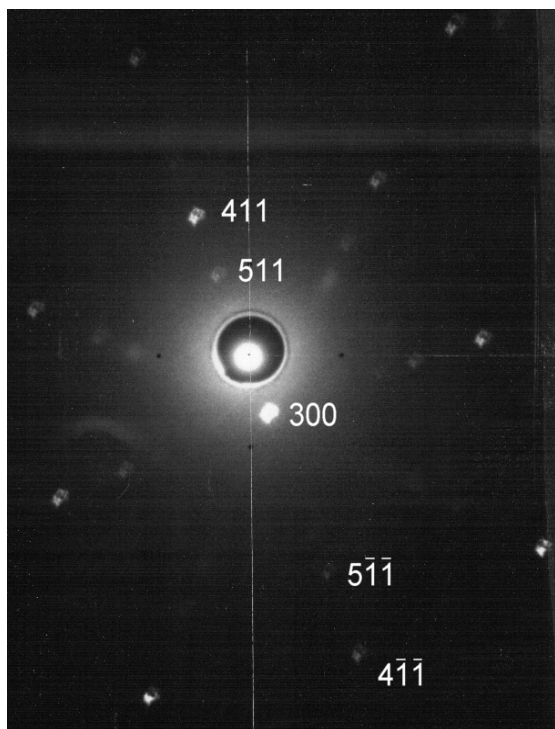

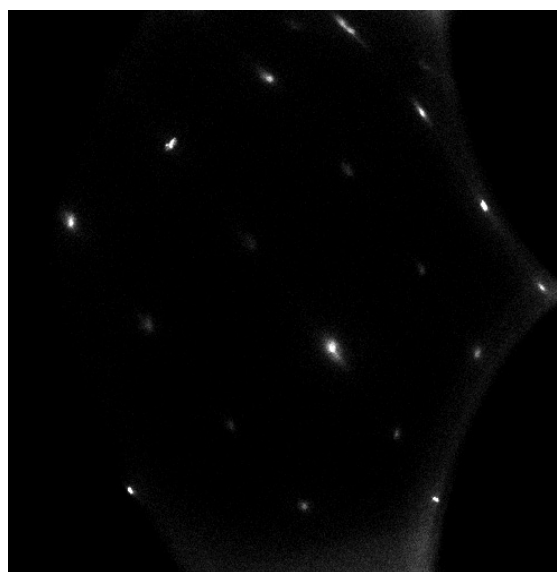**Figure 6.3:** *Laue picture of the Cu3Au(17,1,1) crystal taken after cutting and polishing of the crystal.*

Figure 6.2: *c(2x2) LEED pattern of Cu_3Au in the ordered phase.*

After the AES and SPA-LEED measurements the sample was transferred to the Energy and Azimuth Resolved Ion Scattering Spectrometer (EARISS [32]) for the LEIS measurements. This setup, with a base pressure of $1*10^{-9}$ mbar (mainly H_2 and noble gas), includes a computer controlled manipulator with six degrees of freedom, a standard VARIAN LEED screen, forward scattering and recoiling TOF , a near-180 degrees backscattering TOF and a special toroidal electrostatic analyser (the EARISS analyzer). In this system the same cleaning and surface reconstructing routine was used as for the AES/SPA-LEED measurements. The surface has been routinely checked for contamination before and after measurements with forward scattering and recoiling TOF using 2 keV Ar^+. Forward and recoiling TOF is very sensitive to light elements like carbon, sulphur and oxygen due to the large differential cross-section. No traces of these impurities could be detected (detection limit ~ 0.01 ML) indicating a very clean surface. After cleaning, the sample can be kept for several hours in the main vessel without picking up noticeable contamination. This inert behaviour of the clean Cu_3Au surface has already been reported by other authors [15]. Azimuthal alignment of the sample is performed by measuring the azimuthal dependence of the TOF spectra (forward and back scattering) and identifying the

main crystal axis. The tilt of the sample is adjusted by performing forward scattering TOF measurements until the mirror-reflection mode is reached. In the mirror reflection mode, where the angle of incidence equals the outgoing angle (with respect to the terraces), a maximum in the forward scattered yield is measured. Starting from this well defined orientation, the desired angles of incidence and azimuth are selected. These measurements also provide an easy identification of the step-up and step-down geometry.

The EARISS has been used to measure the surface composition as a function of temperature between RT and 980°C with 2 keV He^+. The surface sensitivity is guaranteed by the properties of the electrostatic analyser, which allows the detection of ions only, in combination with the use of noble gas ions. Projectiles returning from deeper layers have a large chance on neutralization and will hence not be detected. Calibration was performed by measuring pure gold and pure copper poly-crystalline samples. The reference samples were annealed to restore the surface damage caused by the sputter cleaning. See e.g. ref. [33] for more details on ion yields due to the sputtering and annealing of poly- and single crystalline samples. The reduction in calibration accuracy due to the usage of poly-crystalline samples, and the resulting uncertainty in surface density, will be estimated in the discussion section. Radiation damage of the $Cu_3Au(17,1,1)$ sample during the experiments is minimized by using doses of less than 10^{14} ions/cm^2 per measurement after which the surface is annealed at 980°C and slowly cooled (~5°C/minute) to the desired temperature again. Once this temperature is reached, the sample is allowed to reach equilibrium for half an hour for temperatures above 500°C up to 4 hours at RT. Quenching will lead to measurement errors due to a shift in composition while cooling. Segregation time constants can be estimated from composition measurements during sputtering, like performed by Li et al. [34, 35]. These measurements show that even at room temperature the surface composition can change between composition measurements. Therefore, all LEIS measurements are performed at the desired temperature instead of trying to "freeze" the composition at a certain temperature by quenching.

The backscattering TOF has been calibrated by measuring the surface composition at RT, using a geometry in which the deeper layers are obscured by the surface atoms (see e.g. [36]). The sensitivities for Cu and Au are determined by comparing the TOF backscattered yields of Cu and Au with the surface composition as measured with the EARISS at RT. This procedure has been repeated at 980°C, which gave identical results. The step-edge composition is measured between a glancing angle of incidence of 8° and 12° with respect to the (100) terraces in the step-up direction. All TOF measurements are performed using 3 keV He^+ and a maximum dose of $2*10^9$ ions/cm^2. This dose is so small that even if every projectile would selectively cause damage to the step-edge, the effect would not be noticed due to the remaining undamaged areas ("static LEIS measurements"). The choice for the used angle of incidence is based on the fact that alignment of the sample becomes increasingly difficult with decreasing angles of incidence and the backscattering from the step-edges should still be possible (this poses the lower limit). On the other hand only contributions from the step-edges to the scattered yield should be allowed, keeping in mind the acceptance angle of the detector (which poses the upper limit).

The maximum angle of incidence that yields exclusive information about the step-edge composition has been determined from full 3D ion trajectory simulations with a modified version of MATCH [37]. MATCH uses a screened Coulomb potential (Ziegler/Biersack/Wittmark) to describe the interaction between the projectiles and the atoms in the sample. The screening factor was chosen 0.70 [38] for the Cu and 0.95 for the Au. The ion trajectory simulations have been performed for terraces that are separated by single, double and paired steps. The step-edge compositions have been varied between 0% Au and 100% Au whereas simple truncation of the bulk-ordering for $Cu_3Au(17,1,1)$ was assumed with preference for Cu-Au termination at the surface. The simulations include the angular spread of the source (1°) and the acceptance angle of the detector (4°). The energy spread of 10 eV on the primary ion energy of 2 keV is not included since it has a negligible influence on the angular dependent yield. The angular dependent yield in the case of single, double and paired steps is shown in figure 6.5. From the total yield as a function of the angle of incidence it is concluded that no backscattering is possible below an angle of incidence of 4 degrees. The peak at 13 degrees is caused by focussing of the ion beam on each other by the neighbouring atoms. In the case of low index planes no yield would be expected below this angle of incidence. The contribution of the step-edges to the total yield in the case of single, double and paired steps is shown in figure 6.4. From the results it is concluded that the step-edges contribute at least 99 % to the total yield up to an angle of incidence of 12 degrees for all three types of step-edges.
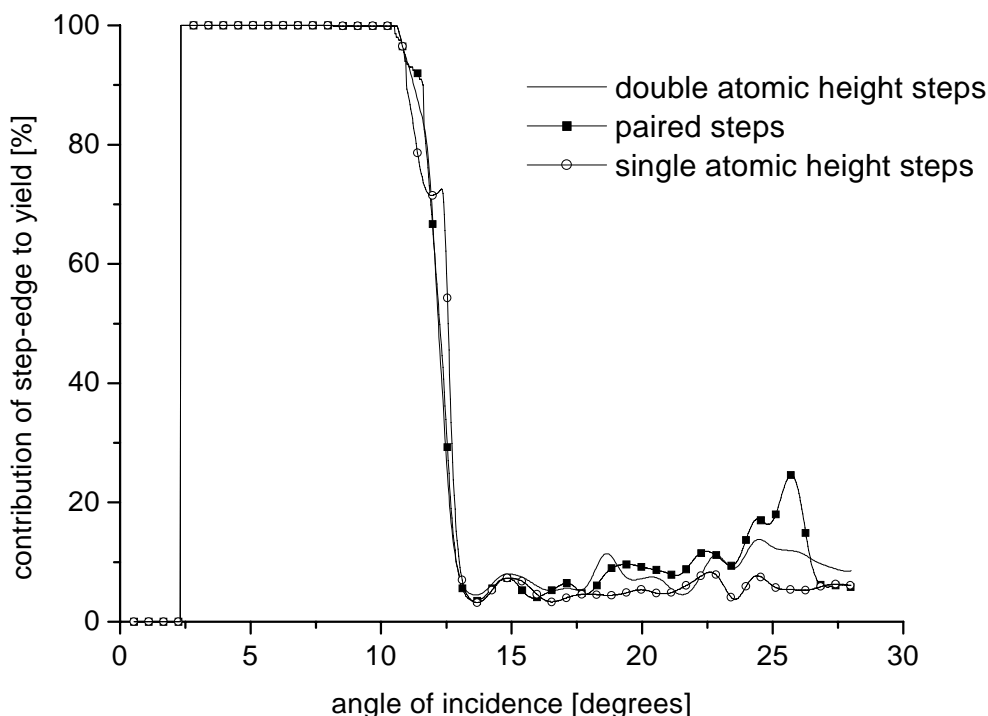

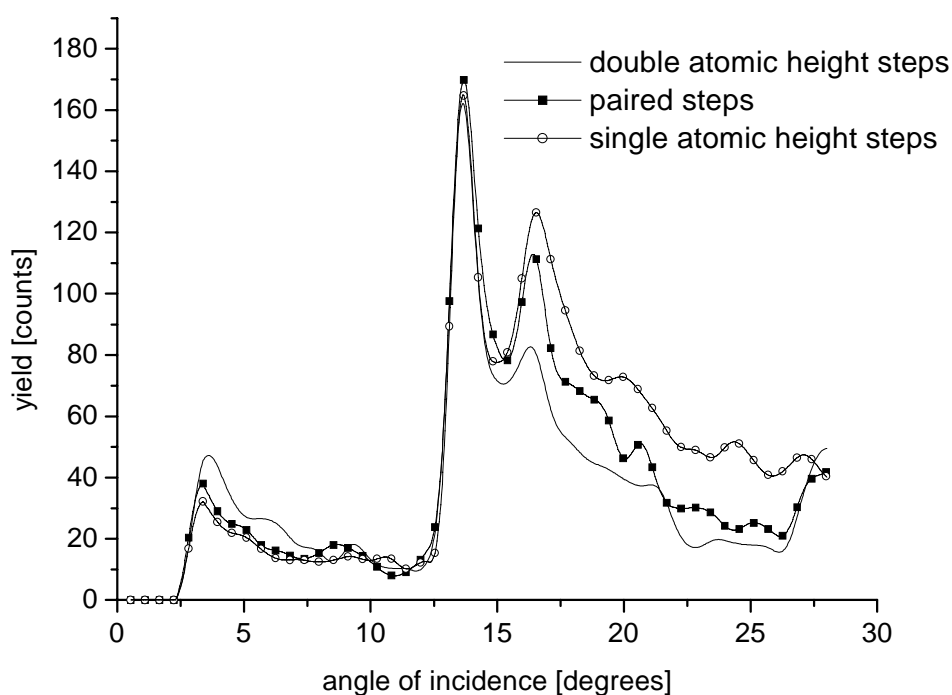**Figure 6.4:** *The angle of incidence dependent contribution of the step-edge to the backscattered yield.*

Figure 6.5: *The angle of incidence dependent yield of 3 keV He on CuAu(17,1,1) according to full trajectory simulations with MATCH.*

The simulation results show that the sensitivities for Au and Cu are independent of the step-edge composition (no focussing effects). Based on the above simulation results, the step-edge measurements are performed from an angle of incidence of $\alpha=4°$ to an angle of incidence of $\alpha=8°$ with respect to the surface, using 1° steps. This is equivalent to $\alpha=8°$ to $\alpha=12°$ with respect to the (100) terraces of the Cu$_3$Au(17,1,1) crystal. At these small angles of incidence the backscattered yield from the crystal's side can be larger than the yield from the step-edges if the sample is misaligned with respect to the ion-beam. Therefore much care is taken to prevent the ion-beam from hitting the side of the crystal in each experiment. Since the sample holder position and rotation will change due to expansion and/or shrinking at different sample temperatures, the sample is aligned each time after the desired measurement temperature is reached.

6.4 Results

6.4.1 Morphology

SPA-LEED measurements have been performed at room temperature (RT) and above the order-disorder transition temperature. The Full Width at Half Maximum (FWHM) of the (0,0) spot has been measured in the perpendicular and parallel direction with respect to the step-edges as a function of the electron energy. The results and expected in-phase and out-of-phase energies

(corrected for the inner potential of 10 eV of the Cu3Au crystal [39]) for single and double atomic height steps are shown in figure 6.6. The FWHM cannot be determined accurately at all energies because the (0,0) spot contains several peaks due to the mosaicity of the crystal. The positions and overlap of these peaks depend on the used primary electron energy. Therefore it is not possible to determine unambiguously if the terraces are separated by single or double atomic height steps. The results at electron energies below 100 eV suggest single atomic height steps, whereas the results at electron energies above 100 eV suggest double atomic height steps. The separation between the peaks becomes larger at higher primary electron energies. Therefore it is expected that the measurements at higher energies are more reliable.
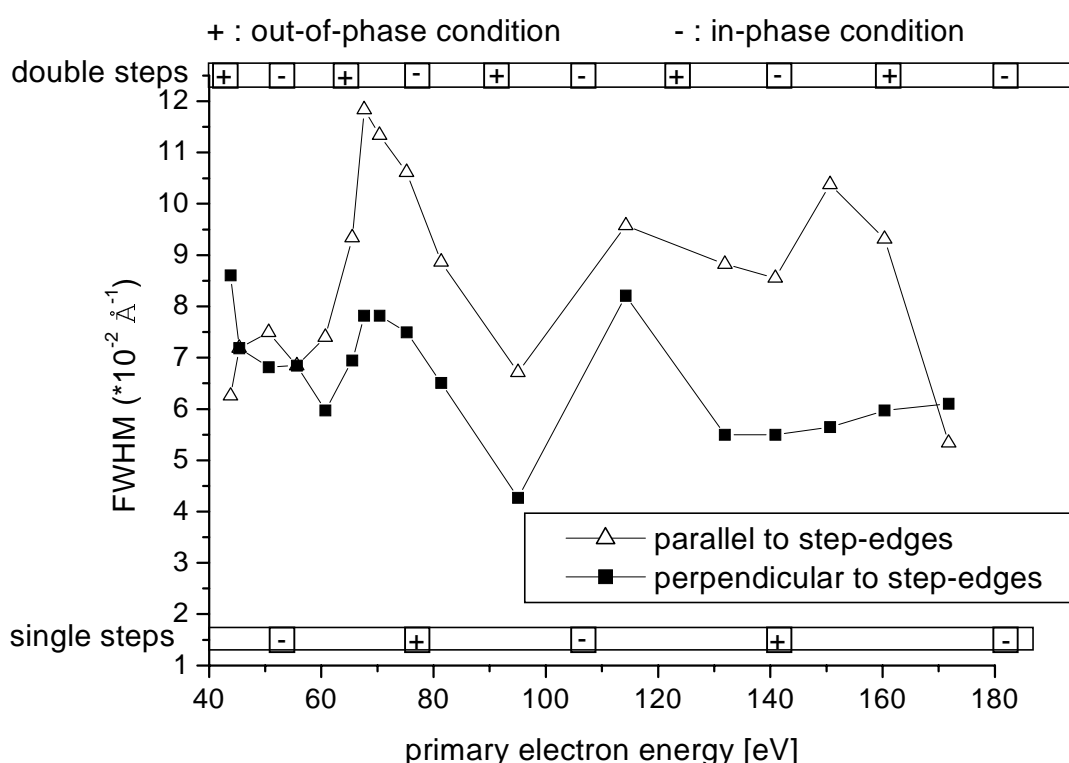

Figure 6.6: *The FWHM of the (0,0) spot as a function of the primary electron energy below the order-disorder temperature (RT). The in-phase and out-of-phase conditions in the case of single and double atomic height steps are indicated in the figure by the minus (in-phase) respectively plus signs (out-of-phase).*

Above the order-disorder temperature the intensity of the (0,0) spot is much smaller which prevents an accurate spot-width determination at even more energies. Measurements at two specific energies (67 eV and 97 eV) have therefore been performed, corresponding to calculated in-phase energies in the case of double atomic height steps, or one out-of-phase and one in-phase energy in the case of singe atomic height steps. These measurements are shown in figure 6.7. Figure 6.7 shows broad peaks for the measurement at 67 eV and narrow peaks for the

measurement at 97 eV. This indicates that above T_o the terraces are separated by single atomic height steps.
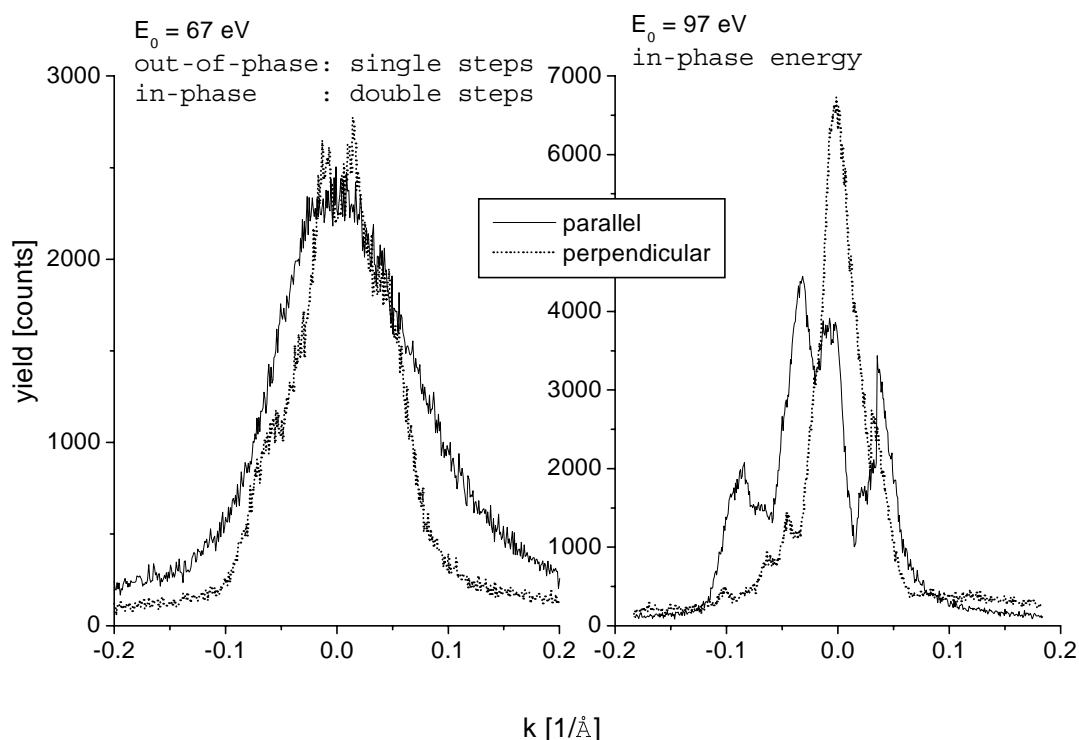

Figure 6.7: *Perpendicular and parallel (with respect to the step-edges) cross-section of the (0,0) spot at one out-of-phase (67 eV) and one in-phase (97 eV) energy above the ordering temperature (T=440°C). The narrow peaks shown in the in-phase measurement are caused by the mosaicity of the crystal. These peaks merge in the out-phase measurement due to broadening.*

From the distance between the peaks of the (0,0) spot in the RT in-phase FWHM measurements a mosaic spread is calculated of ±0.2° (0.4°). From the width of the (0,0) spot at out-of-phase energies an average terrace width of 52 ± 4 Å is calculated. Based on the vicinal angle of the $Cu_3Au(17,1,1)$ crystal, a terrace width of 44 ± 2 Å is expected for terraces that are separated by double atomic height steps. Because of the ambiguity in the determination of the step-height and the calculated versus the expected terrace width, the surface has been cross-checked by AFM in air at RT after preparation in UHV. The result is shown in figure 6.8.

The AFM measurement in figure 6.8 shows equidistant straight step-edges along the <011>. The average terrace width is 50 ± 5 Å. Straight step-edges along the <011> have also been reported by other authors [22, 23] for $Cu_3Au(100)$ crystals. This terrace width is not

compatible with single atomic height steps as were suggested by the FWHM SPA-LEED measurements at primary energies below 100 eV (however, these measurements were in UHV instead of air). Below the ordering temperature the terraces of $Cu_3Au(17,1,1)$ are thus probably separated by double atomic height steps or by paired steps. This will be discussed in more detail in 6.5.1 (discussion section). Above the ordering temperature the terraces are separated by single atomic height steps.
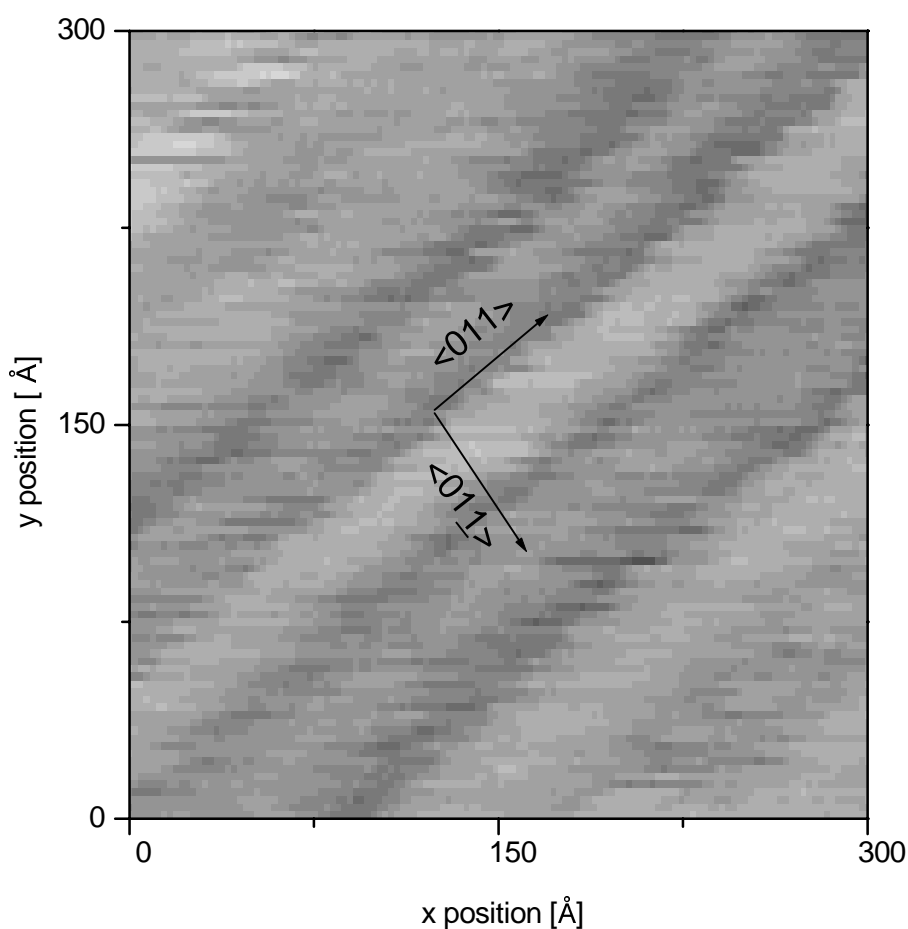

Figure 6.8: *AFM measurement of the $Cu_3Au(17,1,1)$ surface, showing straight step-edges along the <011> and terraces with an average width of 50 Å.*

6.4.2 Surface composition

The surface composition of Cu$_3$Au(17,1,1) has been measured as a function of the temperature with 2 keV He$^+$ using the EARISS [12, 32]. The results are shown in figure 6.9 by the solid squares, the RT surface composition after sputtering is indicated by a star. The maximum error in the determined surface composition is estimated using the following assumptions:

1. The error in the elemental sensitivity has a single sided error bar since the surface density of the poly-crystalline samples is assumed equal to the surface density of the corresponding (111) crystal. However, since the annealing will not be sufficient to actually reach this surface density, the determined sensitivity is an underestimation of the actual value.

2. Due to the larger mobility of gold atoms, the actual surface density of the Au poly-crystalline sample will be closer to the assumed value than in the case of Cu. Therefore a maximum relative error has been assumed of -0%/+20% in the determined sensitivity for Cu, whereas a maximum relative error of -0%/+10% has been assumed for in the determined sensitivity for Au.

3. The LEIS measurements of the Cu$_3$Au(17,1,1) surface composition will show a smaller gold concentration than actually present due to the contribution of the second layer to the scattered yield. From the background of the LEIS spectra it can be estimated that less than 5% of the detected ions are originating from the second and deeper layers. The second layer composition is close to 100% Cu [4, 5, 45], the contribution of the second layer to the yield will thus cause a maximum relative error of -0%/+5% in the determination of the surface composition.

The above mentioned systematical errors cause a maximum absolute error of -3%/+6% Au in the determination of the surface composition, which is a large contribution to the accuracy when compared to the average statistical error of only ±1% Au. The surface composition after sputtering is (30 -4/+7)% Au due to preferential sputtering of Cu. This value is presented by a star in figure 6.9. The error bar on this value indicates the accuracy of the surface composition measurements. For brevity, only the statistical error has been drawn on the remaining surface and step-edge composition measurements.

If the sample is annealed to 950°C, slowly cooled to RT and given an additional period of three hours to reach equilibrium, the measured surface composition at RT is (44 -4/+7)% Au. This equals the surface composition that is calculated assuming step-pairing, simple truncation of the bulk ordering according to figure 6.1 and a detection efficiency of the shielded atoms that is half the value of the unshielded atoms.
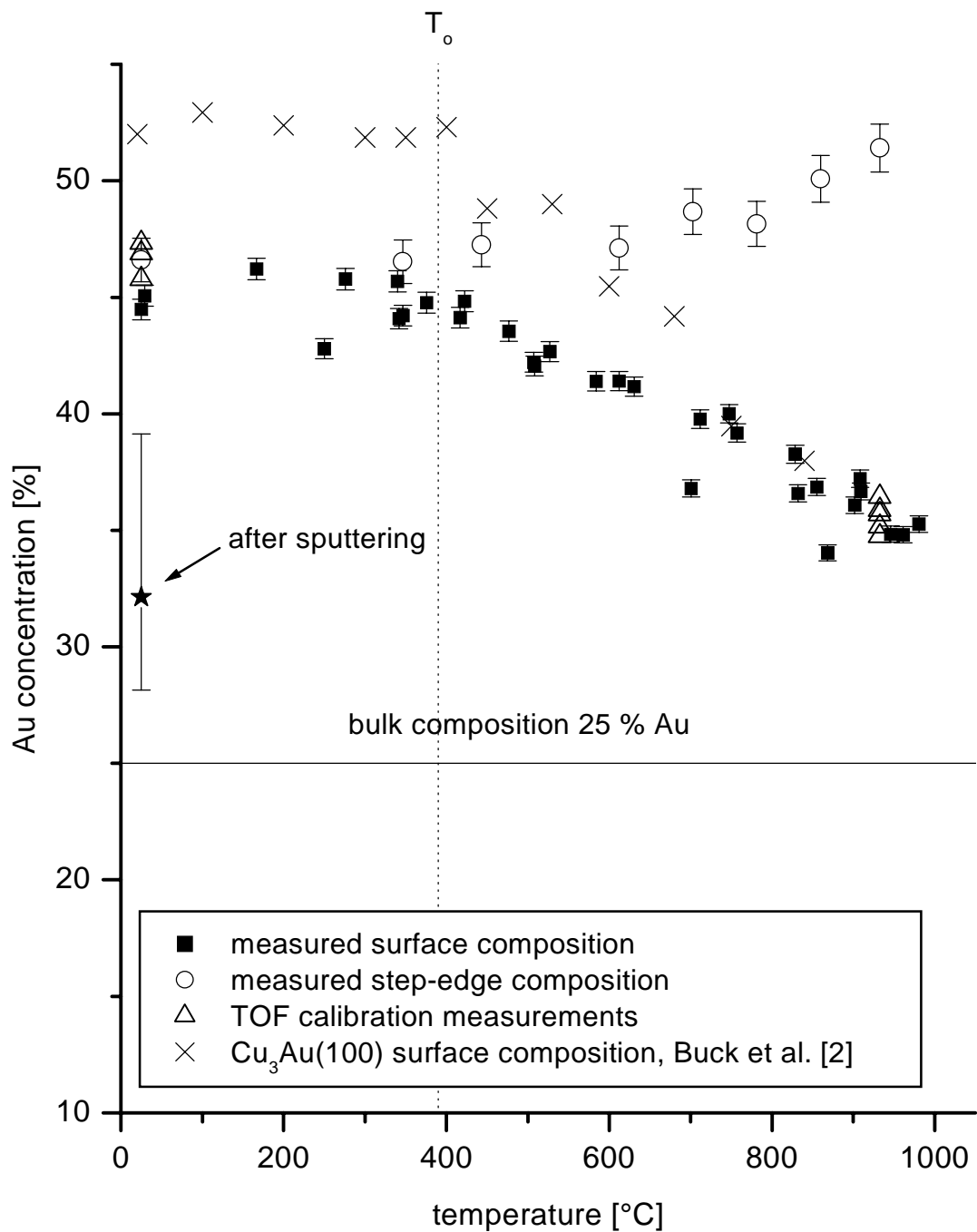
Figure 6.9: *The temperature dependent surface composition (solid squares) and step-edge (circles) composition of Cu₃Au(17,1,1) as measured with the EARISS and the backscattering TOF. The TOF calibration measurements (RT) and verification measurements (980°C) are indicated by the open triangles. The measurement accuracy (including systematic errors) is indicated by the error bar on the composition measurement after sputtering (star). The temperature dependent surface composition of Cu₃Au(100) as reported by Buck et al. [2] is presented by the crosses.*

The measured temperature dependent surface composition of $Cu_3Au(17,1,1)$ is presented in figure 6.9 by the solid squares. In the same figure the temperature dependent surface composition of $Cu_3Au(100)$ as reported by Buck et al.[2] is presented by the crosses. At RT a surface gold concentration of 44% Au is measured for the $Cu_3Au(17,1,1)$ surface, which is smaller than the 52% Au as reported by Buck et al. on $Cu_3Au(100)$ [2]. Similar to the $Cu_3Au(100)$ surface, the gold enrichment slowly decreases with increasing temperatures above T_o. At temperatures well above T_0 the measured surface composition corresponds to the values as reported for the $Cu_3Au(100)$ surface.

6.4.3 Step-edge composition

The backscattering TOF is calibrated by setting the surface composition as measured with the TOF at RT equal to the surface composition as measured with the EARISS. Verification measurements have been performed at 980°C. The TOF surface composition measurements at RT and 980°C are shown in figure 6.9 by the open triangles. The statistical error on the average of the TOF calibration measurements is negligible. Therefore the same accuracy of -4/+7 % Au, as calculated in 6.4.2 for the EARISS measurements and shown in figure 6.9 by the error bars on the measured surface composition after sputtering, is applicable for the TOF surface composition measurements.

The measured temperature dependent step-edge composition is presented by the open circles in figure 6.9. At RT the measured step-edge composition equals the surface composition. With increasing temperature an increase in the step-edge gold concentration is observed. The accuracy on the step-edge composition measurements is also -4/+7 % Au since the step-edge Au concentration is almost equal to the surface Au concentration over the whole temperature range. The yield during the step-edge composition measurements is smaller than the yield during surface composition measurements. Furthermore there is performed only one measurement at each temperature, whereas there are several surface composition measurements performed at RT and 980°C for the calibration. As a result the statistical error during the step-edge composition measurements cannot be neglected. For all step-edge composition measurements the maximum relative error is at most ±2%, the corresponding error bars are shown in figure 6.9 .

6.5 Discussion

6.5.1 Morphology

SPA-LEED measurements above the ordering temperature show terraces that are separated by single atomic height steps (see figure 6.7). The combination of SPA-LEED and AFM measurement results below the ordering temperature suggest that the terraces are separated by double atomic height steps or by paired steps. The used techniques do not provide further discrimination between these types of step-edges. Several types of step-edges are reported on Cu_3Au. First of all, paired steps are reported by Le Geoff et al. for $Cu_3Au(12,1,1)$ [25]. STM

measurements on $Cu_3Au(100)$ by Lin et al. [23] show a mixture of single and double atomic height steps without pronounced preference for either, which is comparable to the paired steps as reported by Le Goff. Mannori et al. [24] report a mixture of single and double atomic height steps based on He diffraction experiments on $Cu_3Au(100)$, with a strong preference for double atomic height steps. Finally, Niehus et al. [22] report double atomic height steps for $Cu_3Au(100)$ based on STM measurements. However, figure 5 of [22] also shows terraces between 40 Å and 50 Å that are separated by paired steps along the <011>. Theoretical work by Aslanides [40] predicts double atomic height steps for ordered $Cu_3Au(11n)$ surfaces and a transition to single atomic height steps above the ordering temperature. However, these results did not include the possibility of paired steps and are based on bulk termination of the surface in the ordered state. In the case of bulk termination and double atomic height steps, a step-edge gold concentration of 25% should be measured. This is incompatible with the results of our step-edge composition measurements that show 44% Au. Based on the close similarity with $Cu_3Au(12,1,1)$ [25] and the fact that none of the other publications is in strong disagreement with paired steps, we assume that the terraces of $Cu_3Au(17,1,1)$ are separated by paired steps.

The measured terrace width of 52 ± 4 Å (SPA-LEED) respectively 50 ± 5 Å (AFM) is larger than the expected terrace width of 45 ± 1 Å based on the vicinal angle and the specified maximum miscut of the $Cu_3Au(17,1,1)$. This suggests a preference for a particular terrace width of about 50 Å, which is also visible in the STM measurements of Niehus et al. [22] and Lin et al. [23]. A possible cause are the Anti-Phase Boundaries (APB's) that exist in Cu_3Au [41, 42] to reduce the stress due to the size mismatch between Cu and Au. The period of the APB's is 37 Å to 68 Å [41, 42], depending on the bulk composition, which is close to the measured average terrace width of 52 Å of the $Cu_3Au(17,1,1)$ crystal.

6.5.2 Surface and step-edge composition

$Cu_3Au(17,1,1)$ shows a constant surface gold concentration of (44 -4/+7)% up to the order-disorder temperature T_o. Above T_o the gold enrichment slowly decreases with increasing temperature. The measured surface gold concentration at 980°C equals (34 -4/+7)%. Similar behaviour was found by Buck et al. for a $Cu_3Au(100)$ surface [2]. For temperatures far above T_o there is good agreement between the measured surface composition of $Cu_3Au(17,1,1)$ and $Cu_3Au(100)$ [2]. Below the order-disorder temperature a larger surface gold concentration of 52% is reported for the $Cu_3Au(100)$ surface. This behaviour is attributed to the structure of the $Cu_3Au(17,1,1)$ crystal. Below T_o there is competition between the continuation of the bulk ordering and the tendency to have Cu-Au termination on the short terraces that are Cu terminated in the case of bulk truncation. This will cause a surface gold concentration below the 50% Au that corresponds to the complete Cu-Au termination that is possible for the $Cu_3Au(100)$ surface. Above T_o the competition between ordering and segregation disappears and the terraces of $Cu_3Au(17,1,1)$ can behave similar to the (100) surface. Since all terraces may become Au enriched above the ordering temperature the drive for the paired steps disappears and a surface reconstruction occurs to terraces that are separated by single atomic height steps.

A surface gold concentration of 44% is calculated for $Cu_3Au(17,1,1)$ when assuming paired steps and simple bulk termination. In this case the pure Cu step-edges and short terraces are responsible for the different calculated surface composition with respect to $Cu_3Au(100)$. However, as will be discussed below, simple bulk truncation is not expected for $Cu_3Au(17,1,1)$. The surface of $Cu_3Au(100)$ unexceptionally shows Cu-Au termination. This indicates gold segregation to the lower coordinated sites. The s4 step-edges of $Cu_3Au(17,1,1)$ (see figure 6.1) are the lowest coordinated sites at the end of a pure Cu layer. Au segregation to the s4 step-edge is therefore expected to cause Cu-Au termination in a way that is similar to the Cu-Au termination of the surface in the case of $Cu_3Au(100)$. The segregation of Au to the step-edges is confirmed by the step-edge composition measurements that show 44% Au, which is much larger than the step-edge gold concentration of 25% Au that should have been measured otherwise.

Above the ordering temperature an increase in the step-edge gold concentration is observed. There are two effects, both related to the order-disorder transition at T_0, that can cause the observed behaviour. First of all, the segregation of gold to the step-edges can be (partly) inhibited as long as chemical ordering is present since the gold concentration of the individual step-edges s1-s4, as shown in figure 6.1, will never exceed 50% Au. Above T_0 the segregation is no longer inhibited by ordering so the gold concentration may become larger than 50%. The second effect that can cause an increase in the measured step-edge Au concentration with increasing temperature is the surface reconstruction from paired steps to single atomic height steps at T_o. In the ordered phase the step-edge s2 has more nearest neighbours than the surface atoms (2 missing neighbours versus 4). Above the order-disorder transition there are only single-atomic height steps, each with 5 missing neighbours. Based on the decrease in average coordination of the step-edge atoms an enhanced gold segregation to the step-edges is therefore expected with respect to the terraces above the order-disorder transition.

The above discussion shows that simple bulk truncation of the $Cu_3Au(17,1,1)$ surface is neither expected nor measured. Two things become apparent from the presented measurement results and the above considerations. First of all segregation of gold to the step-edges of the short (otherwise pure Cu) terraces should occur to explain the observed step-edge gold concentration. However, at the same time a weaker Au segregation should occur to the terraces to explain the lower surface gold concentration with respect to $Cu_3Au(100)$ surface. To check this, the composition of the $Cu_3Au(17,1,1)$ crystal has been calculated for the used temperature range. The general calculation of the composition by minimization of the total free energy requires an enthalpy and an entropy term. The entropy of a phase (the phase being defined as alike atomic positions within the crystal model) can be easily evaluated if the distribution of atoms within that phase has no influence on the enthalpy. For an ordered crystal, like Cu_3Au, this is clearly not the case. Therefore, we will use a Monte Carlo (MC) simulation instead.

Conform to the usual metropolis scheme [43] sequential configurations will be generated that, depending on the energy difference with respect to the previous configuration, will either be accepted or rejected. These configurations are based on the exchange of atoms at two randomly selected lattice sites. The energy difference is calculated from the bond energies of the

involved lattice sites. In the case of an energy decrease the new configuration is always accepted. In the case of an energy increase the new configuration is only accepted if a generated random number between zero and one is smaller than the acceptance chance P_{accept}. (see also chapter 2):

$$P_{accept} = e^{-\frac{\Delta E}{kT}} \quad , \tag{35}$$

with ΔE the energy difference between the old and the new configuration, k the Boltzmann constant and T the temperature. Only bonds between nearest neighbours will be considered. The energy difference between the configurations will be calculated based on the bond energies according to the Surface Modified Pair Potential (SMPP) [44]. The SMPP is a simple empirical model that yields the bond energies between nearest neighbours as a function of the coordination of the involved atoms. Given an n and an m coordinated A (with A being Cu or Au) atom, the total bond energy between these atoms is defined by [44]:

$$E_{nm}^{A} = \varepsilon_{n}^{A} + \varepsilon_{m}^{A} \quad , \tag{36}$$

with ε_{n}^{A} the partial bond energy of an n coordinated A atom. The partial bond energy of an A atom is expressed by:

$$\varepsilon_{n}^{A} = a^{A} + b^{A} * n + c^{A} * n^{2} \quad , \tag{37}$$

with a^{A}, b^{A} and c^{A} empirical constants that have been determined by King et al. [44] for Au and Cu from the heat of sublimation, the energy of bulk vacancy formation and the surface energy. These constants are presented in the table below.

Table 6.1: *Empirical constants a^{A}, b^{A} and c^{A} for Cu and Au as determined by King et al. [44].*

A	a^{A} (eV)	b^{A} (eV)	c^{A} (eV)
Cu	-0.3925	-0.00111	0.000808
Au	-0.3049	-0.02587	0.002070

For Cu$_3$Au the Cu-Au bonds are energetically favourable with respect to the average of the Cu-Cu and Au-Au bonds. In the SMPP model unlike atom interactions between an n coordinated A atom and an m coordinated B atom are given by:

$$E_{nm}^{AB} = \Omega + \varepsilon_{n}^{A} + \varepsilon_{m}^{B} \quad , \tag{38}$$

with Ω the regular solution parameter (see also chapter 2). For negative solution parameters the bulk will tend to order. The actual value of Ω is determined by fitting the measured temperature dependent $Cu_3Au(17,1,1)$ surface composition.

The simulation slabs for $Cu_3Au(100)$ and $Cu_3Au(17,1,1)$ are created periodical in x (the $<01\underline{1}>$ direction) and y (the $<011>$ direction). In z (the $<100>$ direction) two surfaces are defined. Like [45] we will use a rigid lattice (no relaxation) in the MC simulation. Unlike [45] we will not remove one complete layer of Cu to enable Cu-Au termination without competition between segregation and ordering. The rationale here is that the bulk may be an infinite reservoir, but the excess Cu will still cause an energy penalty when it has to be put in the bulk due to the preferential Cu-Au bonding and the assumption of a perfect Cu_3Au lattice in complete thermodynamic equilibrium. The $Cu_3Au(100)$ and $Cu_3Au(17,1,1)$ crystals are defined by 40 (z) atomic layers of 34 (x) by 40 (y) atoms. Back wrapping boundary conditions are applied to the $Cu_3Au(17,1,1)$ crystal in the x direction. In total there are thus 119680 atoms (29920 Au and 89760 Cu) in the slab, of which 320 are step-edge atoms and 2240 are terrace atoms in case of the $Cu_3Au(17,1,1)$ crystal.

At the start of the simulation the atoms are randomly distributed over the lattice. At the first temperature at least 10^6 random exchange attempts are performed to reach equilibrium. More exchanges are tried if the number of accepted exchange attempts is smaller than twice the number of atoms in the slab. Equilibration of the slab is also performed at intermediate temperatures if the temperature difference between two simulation steps is larger than 25°C. Once equilibrium has been approached this way, the composition and ordering of the crystal are evaluated over 2000 generated configurations. Each new configuration is accepted when there have been at least 500 accepted exchange attempts with respect to the previous configuration. The simulation at a certain temperature is stopped if the moving average of the surface concentration over the last 2000 configurations is stable within 0.05% Au during the generation of the last 200 configurations.

The ordering parameter cannot be evaluated at the step-edges and the surface according to the usual long range ordering (LRO) definition for $L1_2$ crystals [3] since it requires the composition calculation over four simple cubic cells, which extend over several atomic layers. Therefore a short range ordering parameter (SRO) has been used according to the following definition:

$$SRO = \frac{\frac{1}{n}\sum_{i=0}^{n-1}|X_i - X_{i+1}| - \overline{dX}}{1 - \overline{dX}} \quad , \quad \overline{dX} = 2\sum_{i=0}^{n-1}X_i\left(1 - X_i\right) \quad , \tag{39}$$

here X_i signals the presence of Au ($X_i = 1$) or Cu ($X_i = 1$) at the ith site. The sum extends over the number of atoms (n) over the lines perpendicular to the simulation slab (y-direction). Using this

definition, the SRO can also be calculated over the step-edge atoms and the surface atoms. Since the slab consists of 34x40 atoms, the number of atoms perpendicular to the simulation slab is n=40. As in the case of the composition calculation, the SRO's of the different phases are averaged over the last 2000 configurations. The SRO is defined in such way by equation (39) that complete ordering of a phase corresponds to SRO=1 and complete disorder corresponds to SRO=0.

In figure 6.10 the temperature dependent SRO's for the first and third layer of $Cu_3Au(100)$ are presented for the selected value of $\Omega = -0.047$ eV. The SRO's show good agreement with the reported trends for $Cu_3Au(100)$ in literature. The slower decrease in the surface SRO with respect to the third layer SRO with increasing temperature mimics the continuous decrease in the surface ordering (second order transition) and the abrupt decrease in the bulk ordering (first order transition). The calculated temperature dependent third layer SRO for $Cu_3Au(17,1,1)$ is presented in figure 6.10 by the solid line with open squares. An abrupt order-disorder transition is observed at the same temperature as for the third layer of the $Cu_3Au(100)$ crystal. The final value at temperatures below the order-disorder temperature is smaller than one, which shows that there is no perfect ordering of the third layer.
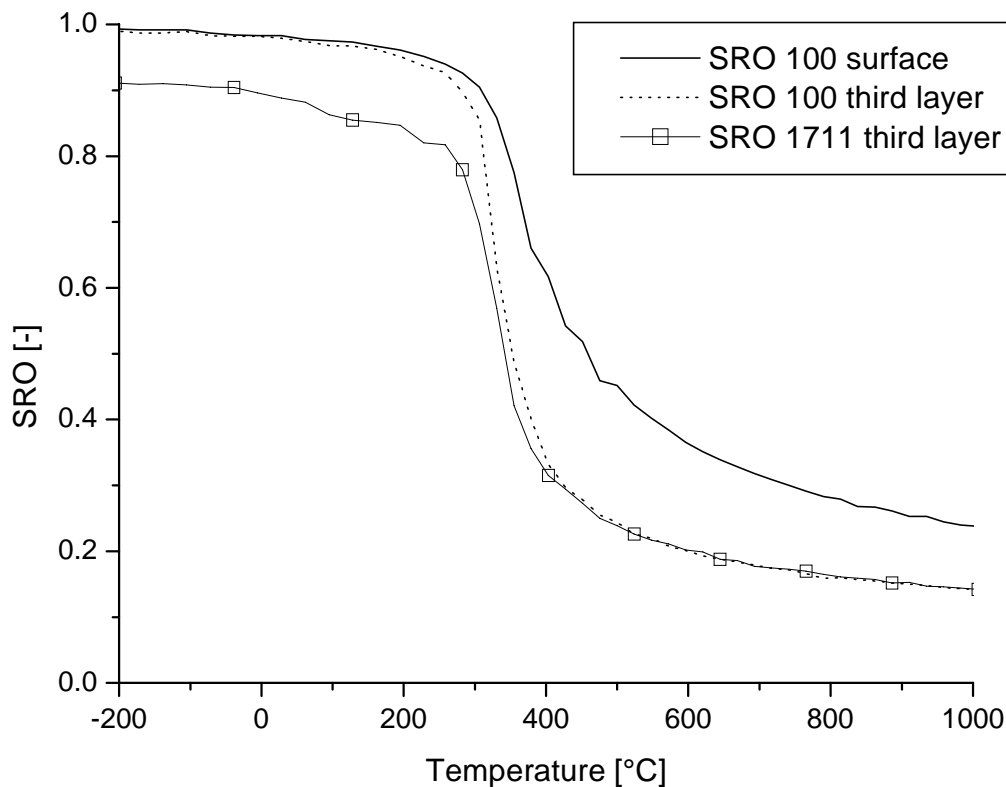

Figure 6.10: *The calculated SRO for the surface and the third layer of $Cu_3Au(100)$ and the third atomic layer of $Cu_3Au(17,1,1)$.*

  The calculated surface compositions of Cu$_3$Au(17,1,1) (solid line) and Cu$_3$Au(100) (solid line with open squares) are presented in figure 6.11. The measured surface composition of Cu$_3$Au(17,1,1) is presented in figure 6.11 by the solid squares. The calculated surface composition shows good agreement with the measured surface composition over the whole temperature range. At temperatures far above the transition temperature, the calculated surface composition of Cu$_3$Au(17,1,1) approaches the calculated surface composition of Cu$_3$Au(100). This behaviour is also observed in the measured surface composition on Cu$_3$Au(100) by Buck et al. [2] with respect to the measured surface composition of Cu$_3$Au(17,1,1). Above the order-disorder temperature there is a surface reconstruction from paired steps to single atomic height steps. However, as can be seen from the difference between the calculated surface composition of Cu$_3$Au(17,1,1) with respect to that of Cu$_3$Au(100) in figure 6.11, the influence of the step-edges is only moderate far above the order-disorder temperature. A correction for four single atomic height steps, separated by equally spaced terraces instead of the s1-s4 type step-edges as shown in figure 6.1, would yield a surface Au concentration that is 1.2% Au larger due to the decreased coordination and increased visibility of step-edge s2.
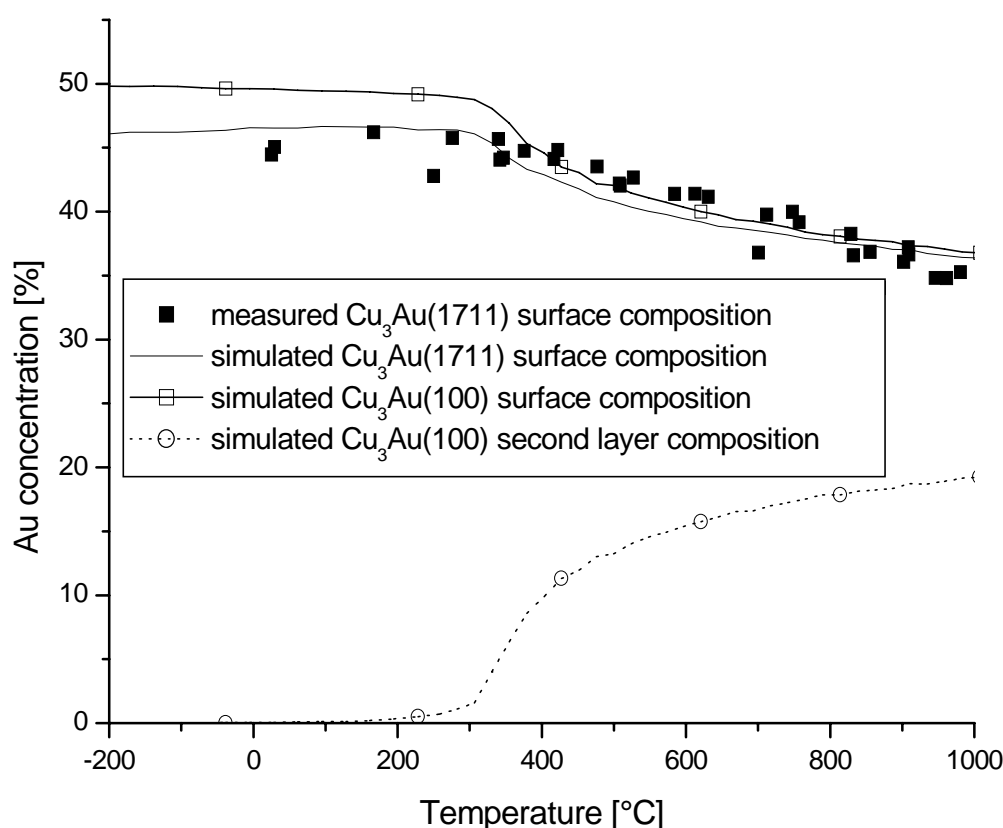

Figure 6.11: *The calculated(solid line) and measured (solid squares) temperature dependent surface composition of Cu$_3$Au(17,1,1). Also the calculated surface (solid lines with the solid squares) and second layer (dotted lines with solid circles) compositions of Cu$_3$Au(100) are shown.*

6.6 Conclusions

According to SPA-LEED FWHM measurements of the (0,0) spot, the $Cu_3Au(17,1,1)$ surface has single atomic height steps above the ordering temperature. Below the ordering temperature the combination of AFM and SPA-LEED measurements and the results of STM measurements on $Cu_3Au(12,1,1)$ and $Cu_3Au(13,1,1)$ (which are very similar to our crystal) as presented by Le Goff et al. [25] suggest that $Cu_3Au(17,1,1)$ has paired steps.

The temperature dependent composition of $Cu_3Au(17,1,1)$ has been calculated using Monte-Carlo simulations. The bond energies have been calculated according to the Surface Modified Pair Potential (SMPP) [44]. The main feature of the SMPP is an empirical coordination dependent bond energy which is derived from the heat of sublimation, the energy of bulk vacancy formation and the surface energy of the used elements. The regular solution parameter that describes the energy difference due to unlike neighbour interactions is fitted to the measured surface composition of $Cu_3Au(17,1,1)$. The calculated $Cu_3Au(17,1,1)$ surface Au concentration shows excellent agreement with the measured values over the whole temperature range. The smaller gold segregation of $Cu_3Au(17,1,1)$ with respect to $Cu_3Au(100)$ below T_o can be explained by the reduction in driving force due to the competition between the continuation of the bulk ordering and segregation of gold to the, otherwise completely Cu terminated, short terraces and the s2 and s4 type step-edges (see figure 6.1).

Above the order-disorder temperature the (100) terraces of $Cu_3Au(17,1,1)$ behave identical to the surface of the (100) crystal. A surface reconstruction occurs from paired steps to single atomic height steps since both terraces may become Au enriched in the absence of bulk ordering. As a result the calculated surface composition of $Cu_3Au(17,1,1)$ becomes almost equal to the calculated surface composition of $Cu_3Au(100)$. The effect of the different step-edge composition on the measured surface composition may be neglected due to the large terrace width.

The increase in the step-edge Au concentration with increasing temperature is caused by two effects. First of all, the segregation of Au to the low coordinated step-edges (s1, s3 and s4) is inhibited beyond 50% Au by the ordering below the order-disorder temperature. Above the order-disorder temperature the gold concentration can exceed 50%. The second effect is the surface reconstruction to single atomic height steps at the order-disorder temperature. The s2 step-edge is slightly Cu enriched in the ordered phase due to the high coordination in combination with the fact that it is located in the pure Cu layer. Due to the surface reconstruction the coordination decreases and the ordering is lost, causing a strong increase in the Au concentration of the s2 step-edge.

References:

1. J. M. Cowley, J. Appl. Phys. 21 (1950) 24

2. T. M. Buck, G. H. Wheatley, L. Marchut, Phys. Rev. Letters 51 (1983) 43

3. M.A. Vasiliev, J. Phys.. D: Appl. Phys. 30 (1997) 3037

4. S. Mróz, Progress in Surf. Sci. 59 (1998) 323

5. H. Reichert, H. Dosch, Surf. Sci. 345 (1996) 27

6. S. Schömann, E. Taglauer, Surf. Rev. and Letters 3 (1996) 1823

7. M. J. Sparnaay, G. E. Thomas, Surf. Sci. 135 (1983) 184

8. Y. Asahara, H. Tokutaka, K. Nishimori, N. Ishihara, J. Le Héricy, J. P. Langeron, Appl. Surf. Sci. 33/34 (1988) 107

9. W. Losch, J. Kirschner, J. Vac. Sci. Tech. 15 (1978) 1541

10. R. A. van Santen, L. H. Toneman, R. Bouwman, Surf. Sci. 47 (1975) 64

11. H. Over, G. Gilarowski, H. Niehus, Surf. Sci. Letters 381 (1997) L619

12. E. G. McRae, T. M. Buck, R. A. Malic, W. E. Wallace, Surf. Sci. Letters 238 (1990) L481

13. R. Beikler, E. Taglauer, Nucl. Instr. Meth. B 161 (2000) 390

14. H. Reichert, P.J. Eng, H. Dosch, I. K. Robinson, Phys. Rev. Letters 74 (1995) 2006

15. S. B. Rivers, W. N. Unertl, H. H. Hung, K. S. Liang, Phys. Rev. B 52 (1995) 12601

16. V. Kumar, K. H. Bennemann, Phys. Rev. Letters 53 (1984) 278

17. J. M. Sanchez, J. L. Marán-López, Surf. Sci. Letters 157 (1985) L297

18. J. M. Sanchez, J. L. Morán-López, Phys. Rev. B 32 (1985) 3534

19. M. Hou, M. El Azzaoui, Surf. Sci. 380 (1997) 210

20. M. A. Hoffman, P. Wynblatt, Surf. Sci. 236 (1990) 369

21. B. Moest, P.T. Wouda, A.W. Denier van der Gon, M.C. Langelaar, H.H. Brongersma, B.E. Nieuwenhuys, D.O. Boerma, Surf. Sci. 473 (2001) 159 (chapter 4 of this thesis)

22. H. Niehus, C. Achete, Surf. Sci. 289 (1993) 19

23. M.T. Lin, J. Shen, W. Kuch, H. Jenniches, M. Klaua, C.M. Schneider, J. Kirschner, Surf. Sci. 410 (1998) 290

24. C. Mannori, T. Scimia, P.Cantini, S. Terrini, M. Canepa, L. Mattera, Surf. Sci. 433-435 (1999) 307

25. E. Le Goff, L. Barbier, S. Goapper, A. Loiseau, B. Salanon, Surf. Sci. 466 (2000) 73

26. U. Scheithauer, G. Meyer, M. Henzler, Surf. Sci. 178 (1986) 441

27. M. Henzler, Surf. Sci. 152/153 (1985) 963

28. H.H. Brongersma, P.M. Mul, Surf. Sci. 35 (1973) 393

29. H. Niehus, W. Heiland, R.J. MacDonald, Surface Science Reports 17 (1993) 213

30. R. Koper, Surface Preparation Laboratory, Penningweg 69F, 1507 DE Zaandam, The Netherlands

31. Structure and morphology of thin metallic over layers, PhD thesis W.C.A.N. Ceelen, Eindhoven, ISBN 90-386-0577-3, 1997

32. J.A. Hellings, H. Ottevanger, S.W. Boelens, C.L.C.M. Knibbeler, H.H. Brongersma, Surf. Sci. 162 (1985) 913

33. R. Cortenraad, S.N. Ermolov, B. Moest, A.W. Denier van der Gon, V.G. Glebovsky, H.H. Brongersma, Nucl. Instr. Meth. B 174 (2001) 173

34. R.S. Li, Surf. Sci. 193 (1988) 373

35. R.S. Li, T. Koshikawa, Surf. Sci 151 (1985) 459

36. T. M. Buck, G. H. Wheatley, D. P. Jakson, Nucl. Instr. Meth. B 218 (1983) 257

37. M.H. Langelaar, M. Breeman, A.V. Mijiritskii, D.O. Boerma, Nucl. Instr. Meth. B (1997) 587

38. H. Niehus, R.P. Blum, D. Ahlbehrendt, phys. stat. sol. 187 (2001) 151

39. F. Bruno, S. Terreni, L. Floreano, A. Cossaro, D. Cvetko, P. Luches, L. Mattera, A. Morgante, R. Moroni, M. Repetto, A. Verdini, M. Canepa, Phys. Rev. B 66 (2002) 045402

40. A. Aslanides, M. Hayoun, V. Pontikis, Surf. Sci. 370 (1997) L163

41. T. Shinohara, S. Saitoh, F. Wagutama, S. Yamaguch, Philos. Mag. A 79 (1999) 437

42. Y. Huang, J. M. Cowley, Surf. Sci. 285 (1993) 42

43. A modern course in statistical physics, L.E. Reichl, University of Texas, ISBN 0-7131-35174, 1980

44. T.S. King, R.G. Donnelly, Surf. Sci. 141 (1984) 417

45. M. Hayoun, V. Pontikis, C. Winter, Surf. Sci. 398 (1998) 125

Summary

The goal of this thesis is to determine the morphology and/or composition of the surface region of metallic single crystal model systems. The emphasis is put on establishing a relation between the temperature dependent surface and step-edge composition of vicinal bimetallic single crystals using Low Energy Ion Scattering (LEIS). It is shown that the Time-Of-Flight (TOF) technique can be used in a near 180 degrees backscattering mode (Co-Axial Impact Scattering Ion Spectroscopy: CAICISS) to selectively probe the step-edge composition of such vicinal crystals. The measurements have been compared with the calculated step-edge and surface composition in the framework of the broken bond model. Two model alloys, the random mixing PtRh and the ordering CuAu, have been selected because of the extensive studies that have been performed on the low index planes of these systems in the past. The results in chapters 4-6 show that the broken bond model can be successfully applied to explain both the enhanced segregation of Pt to the step-edges of PtRh and the inhibition of Au segregation to the step-edges of CuAu. However, at the same time it is clear that more research is required to verify the assumptions that were made in explaining the features of e.g. PtRh(511).

In chapter 3 the results of a morphology study on the clean K/Fe(110) system are presented. Here the Normal Incidence X-Ray Standing Wave (NIXSW) technique is applied in the (220), (200) and (112) Bragg reflection to determine the bond length and the adsorption site after saturation coverage of potassium on Fe(110) at room temperature. The Low Energy Electron Diffraction (LEED) measurements show a combination of hexagons due to the potassium overlayer and rectangular patterns due the bcc lattice of Fe(110). A perfect hexagonal overlayer is ruled out based on the XSW results that show a correlation between the iron lattice and the potassium in both direction perpendicular to the surface. Deformed hexagons, with the long bridge site as preferential site, can explain the XSW results and the observed LEED patterns, including the extra spots which have been attributed to multiple scattering in literature. The observed potassium hard sphere radius of 2.11 ± 0.22 Å is among the largest reported. This is in agreement with the fact that the radius of adsorbed potassium on metal substrates tends to increase with increasing coverage and increasing coordination.

In chapter 4 it is shown that the temperature dependent surface composition of clean $Pt_{25}Rh_{75}(410)$ can be described well by the broken bond model. An enhanced segregation to the step-edge is observed, which is even stronger than expected based on the reduced coordination of the step-edge atoms. Good agreement with the measurement results is obtained when a coordination dependent bond energy is used, which indicates a stronger relaxation of the step-

edge atoms with respect to the terrace atoms. Efficient, easy adaptable and reliable ion trajectory simulation software proved to be a necessity in explaining the measured CAICISS-TOF spectra. In this respect MATCH showed itself superior to SISS-92. Ion trajectory simulations have been used to verify the existence of the double atomic height steps of $Pt_{25}Rh_{75}(410)$ and to determine the contribution of the different atomic sites to the scattered yield as a function of the angle of incidence. The latter was especially important due to the specific scattering geometry.

The temperature dependent step-edge and surface composition of clean and oxidized $Pt_{50}Rh_{50}(511)$ are presented in chapter 5. The surface composition of clean $Pt_{50}Rh_{50}(511)$ shows a steep decrease in Pt segregation with increasing temperature at 750°C. The step-edge composition of clean $Pt_{50}Rh_{50}(511)$ is near 100% Pt over the measured temperature range. This is even stronger than can be expected by the coordination dependent bond energy as found in the case of $Pt_{25}Rh_{75}(410)$. Both the steep decrease in Pt surface segregation as the extreme Pt segregation to the step-edges can be reproduced by assuming a unreconstructed surface above 800°C and a missing row structure below 750°C. The transition to a unreconstructed surface between 750°C and 800°C would explain the steep decrease in segregation, whereas the decreased coordination of the step-edge atoms would explain the extreme segregation of Pt to the step-edges. The surface and the step-edge composition of oxidized $Pt_{50}Rh_{50}(511)$ are equal within the measurement accuracy. This suggests that there is no energy difference between Pt-O and Rh-O bonds.

In chapter 6 the temperature dependent surface and step-edge composition of the ordering $Cu_3Au(17,1,1)$ are presented. From the performed Atomic Force Microscope (AFM) and SPA-LEED measurements it was not possible to draw a final conclusion about the type of step-edges of the $Cu_3Au(17,1,1)$ crystal. It was assumed that $Cu_3Au(17,1,1)$ has paired steps (a specific combination of single and double atomic height steps) based on the close similarity with the $Cu_3Au(13,1,1)$ crystal, for which paired steps are reported in literature. At room temperature the measured step-edge and surface gold concentrations of 43% Au are smaller than the 50% Au as reported for the surface of $Cu_3Au(100)$. Above the ordering temperature the measured surface composition approaches the surface composition of $Cu_3Au(100)$, whereas the step-edge gold concentration increases. Both observations are attributed to the step-edges of $Cu_3Au(17,1,1)$. Monte Carlo simulations have been performed to calculate the surface and the step-edge composition over the whole temperature range. Excellent agreement exists between the measured and the calculated surface composition. The calculated step-edge composition equals 50% Au over the whole temperature range. Ion trajectory simulations show that double atomic height steps cause a contribution of the second (Cu rich) layer to the scattered yield. This results in a measured step-edge gold concentration below 50% Au below the ordering temperature. At the order-disorder temperature the double atomic height steps disappear in favour of single atomic height steps. This causes the observed increase of the Au segregation.

Samenvatting

Het doel van het promotie onderzoek was het onderzoeken van de oppervlakte struktuur en/of samenstelling van metalen mono-kristallen. De nadruk lag op het vinden van de relatie tussen de temperatuurafhankelijke oppervlakte en staprand samenstelling van gestapte mono-kristallijne legeringen met lage energie ionen strooiing (LEIS). Er wordt in dit proefschrift aangetoond dat het mogelijk is om met vluchttijd metingen (TOF) specifiek de staprand samenstelling te meten door in een speciale geometrie te werken waarin de strooihoek bijna gelijk is aan 180 graden (CAICISS). De metingen zijn vergeleken met de berekende staprand en oppervlakte samenstelling onder de aanname van het zogenaamde verbroken-binding model. Twee veel gebruikte model legeringen, het wanordelijk mengende PtRh en het chemisch geordende CuAu, zijn gekozen vanwege de beschikbare literatuur ten aanzien van de lage index vlakken. De resultaten in de hoofdstukken 4 tot en met 6 laten zien dat het verbroken-binding model met succes kan worden toegepast om de versterkte segregatie van Pt naar de stapranden van PtRh te verklaren terwijl de segregatie van Au naar de stapranden van CuAu juist wordt voorkomen door de chemische ordening. Hierbij moet worden opgemerkt dat er extra onderzoek nodig is om de veronderstellingen te controleren die er zijn gemaakt bij het verklaren van de verschijnselen bij onder andere PtRh(511).

In hoofdstuk 3 worden de resultaten van struktuur onderzoek aan het schone K/Fe(110) oppervlak getoond. Het kalium is bij kamertemperatuur tot de verzadigingswaarde op het ijzer gedeponeerd. Bij vrijwel loodrechte reflectie van de röntgen straling aan het ijzer rooster ontstaan er staande golven (NIXSW) die gebruikt zijn om via triangulatie de afstand tussen het ijzer en kalium en de positie van de kalium atomen aan het oppervlak te bepalen. Lage energie electronen verstrooiing (LEED) metingen aan K/Fe(110) laten de combinatie van een rechthoekige struktuur zien als gevolg van het bcc ijzer-rooster en een hexagonale struktuur als gevolg van het gedeponeerde kalium. Op basis van de XSW metingen is geconcludeerd dat het kalium geen perfect hexagonale laag op het ijzer vormt. Met behulp van een vervormde hexagonale struktuur, waarbij de kalium atomen een voorkeur zouden hebben voor de positie tussen de ijzer atomen, is het mogelijk om zowel de XSW als LEED resultaten te reproduceren, inclusief de extra spots in het LEED patroon die in de literatuur zijn toegekend aan dubbele strooiing. De waargenomen afstand van 2.11 ± 0.22 Å tussen het ijzer en het kalium behoort tot de hoogste waarden uit de literatuur. Dit is in overeenstemming met de tendens waarbij de straal van kalium toeneemt naarmate de coördinatie en de bedekkingsdichtheid van het kalium toenemen.

In hoofdstuk 4 wordt aangetoond dat de oppervlakte samenstelling van $Pt_{25}Rh_{75}(410)$ goed beschreven kan worden met het verbroken-binding model. De versterkte segregatie van Pt naar de staprand is echter zelfs sterker dan er verwacht zou worden op basis van de lagere coördinatie van de staprand atomen. Als er wordt aangenomen dat de bindingsenergie afhangt van de lokale struktuur van de atomen, bijvoorbeeld als gevolg van relaxatie, is het wel mogelijk om overeenstemming te bereiken tussen de meetwaarden en de theorie. Om de TOF metingen te verklaren is het noodzakelijk om de ionen banen te simuleren. Het pakket MATCH bleek hierin beter dan het tot nu toe gebruikte SISS-92. Met behulp van simulaties is de verhouding van de verschillende roosterposities aan de TOF opbrengst bepaald als funktie van de gebruikte hoek van inval. Juist voor $Pt_{25}Rh_{75}(410)$ is dit zo belangrijk, omdat de dubbele stappen van dit kristal ervoor zorgen dat de atomen tussen de stap-atomen in een relatief grote bijdrage hebben aan de TOF metingen.

In hoofdstuk 5 worden metingen getoond aan zuiver en geoxideerd $Pt_{50}Rh_{50}(511)$. De Pt concentratie van zuiver $Pt_{50}Rh_{50}(511)$ neemt bij 750°C ineens sterk af, terwijl de staprand samenstelling over het gehele gemeten temperatuur bereik vrijwel constant 100% Pt is. De Pt concentratie van de staprand is zelfs hoger dan verwacht op basis van de omgevingsafhankelijke bindingsenergie als in het geval van $Pt_{25}Rh_{75}(410)$. Zowel de sterke verandering in de oppervlakte samenstelling als de hoge Pt concentratie in de staprand zouden verklaard kunnen worden door een overgang van een gereconstrueerd oppervlak met verwijderde atoom rijen onder 750°C naar een niet gereconstrueerd oppervlak boven 800°C. Bij het geoxideerde $Pt_{50}Rh_{50}(511)$ is de gemeten oppervlakte samenstelling gelijk aan de staprand samenstelling. Dit geeft aan dat er geen voorkeur is voor Pt-O of Rh-O bindingen.

In hoofdstuk 6 wordt het chemisch geordende $Cu_3Au(17,1,1)$ behandeld. Op basis van metingen met de atomaire-kracht microscoop (AFM) en de LEED is het niet mogelijk een conclusie ten aanzien van het type stapranden van $Cu_3Au(17,1,1)$ te trekken. Van $Cu_3Au(13,1,1)$ is in de literatuur echter bekend dat het gepaarde stappen heeft (een specifieke combinatie van enkele en dubbele stappen). Vanwege de sterke overeenkomsten tussen $Cu_3Au(17,1,1)$ en $Cu_3Au(13,1,1)$ is er daarom aangenomen dat $Cu_3Au(17,1,1)$ ook gepaarde stappen heeft. De bij kamertemperatuur gemeten oppervlakte en staprand samenstelling van 43% Au is kleiner dan de gerapporteerde waarde voor het oppervlak van 50% Au bij $Cu_3Au(100)$. Boven de fase overgang benadert de gemeten oppervlakte samenstelling van $Cu_3Au(17,1,1)$ die van $Cu_3Au(100)$ terwijl de Au concentratie aan de staprand licht toeneemt. Er zijn Monte Carlo simulaties gedaan om de staprand en oppervlakte samenstelling van $Cu_3Au(17,1,1)$ over het gehele temperatuur bereik te bepalen. De resultaten komen uitstekend overeen met de gemeten waarden. De combinatie van de Monte Carlo simulaties en ionen banen simulaties met MATCH laten zien dat de toename van de staprand samenstelling bij het overschrijden van de ordening temperatuur waarschijnlijk wordt veroorzaakt door het overgaan van dubbele naar enkele stappen.

List of publications

Chapter 3
Determination of the K adsorption site on Fe(110) with XSW
B. Moest, T. Schmidt, W.C.A.N. Ceelen, A.W. Denier Van Der Gon, J. Falta, H. H. Brongersma
Surf. Sci. 520 (2002) 137

Chapter 4
Step-edge segregation of bimetallic alloys: A LEIS study of $Pt_{25}Rh_{75}$(410)
B. Moest, P.T. Wouda, A.W. Denier van der Gon, M.C. Langelaar, H.H. Brongersma,
B.E. Nieuwenhuys, D.O. Boerma
Surf. Sci. 473 (2001) 159

Chapter 5
The surface and step edge composition of clean and oxygen covered $Pt_{50}Rh_{50}$(511)
B. Moest, S. Helfensteyn, P. Deurink, M. Nelis, A.W. Denier van der Gon, H.H. Brongersma,
C. Creemers, B.E.Nieuwenhuys
Surf. Sci. 536 (2003) 177

Chapter 6
The step edge and surface composition of Cu_3Au(17,1,1) near the order-disorder transition
B. Moest, A.W. Denier van der Gon, H.H. Brongersma
To be published

Other

Study of Pd single crystals grown by crucible-less zone melting
B. Moest, V.G. Glebovsky, H.H. Brongersma, R.H. Bergmans, A.W. Denier van der Gon,
V.N. Semelov
Journal of crystal growth 192 (1998) 410

Segregation of Pt on Pd(110)
B. Moest, R. Bergmans, A.W. Denier van der Gon, H.H. Brongersma, V.G. Glebovsky, V.N.
Semelov
Poverkhnost 10 (2000) 18

Ultra thin Au layers on Si(100): surface silicide formation at room temperature
W.C.A.N. Ceelen, B. Moest, M. de Ridder, L.J. van Ijzendoorn, A.W. Denier van der Gon,
H.H. Brongersma
Appl. Surf. Sci. 134 (1998) 87

Morphology and composition of Au films on Si(100)
W.C.A.N. Ceelen, M. de Ridder, B. Moest, A.W. Denier van der Gon, H.H. Brongersma
Surf. Sci. 430 (1999) 146

Crystal-face dependence of Low-Energy Ion Scattering Signals
R. Cortenraad, S.N. Ermolov, B. Moest, A.W. Denier van der Gon, V.G. Glebovsky,
H.H. Brongersma
Nucl. Instr. And Meth. B 174 (2001) 173

Dankwoord

Tja, daar is dat proefschrift dan.... eindelijk. Een mooi moment om iedereen te bedanken die de tijd heeft genomen om er op te wachten en/of actief een bijdrage heeft gehad aan de totstandkoming. Als eerste bedank ik Hidde en Arnoud voor de mogelijkheid om bij FOG te promoveren en voor de goede begeleiding. Ik ben heel erg geschrokken van het plotselinge overlijden van Arnoud vorig jaar. Wat mij vooral bijblijft is het plezier dat Arnoud had in de natuurkunde en hoe dit overstraalde tijdens de discussies met hem over de resultaten. Hierdoor kreeg ik altijd weer zin om metingen verder te verklaren of simulaties toe te lichten (meestal met het nodige werk als resultaat) en ik hoop dan ook dat iedereen iets van zijn stijl en kritische blik herkent in de hoofdstukken van dit proefschrift.

Thomas Schmidt en Jens Falta bedank ik voor de prettige samenwerking aan het kalium op ijzer. Dit geldt zowel voor de metingen die bij HASYLAB in Hamburg zijn gedaan (altijd leuk om met z'n allen zo'n aparte uren te draaien) als voor het stuk "nazorg" bij het uitwerken van de gegevens. Peter Wouda en Ben Nieuwenhuys dank ik voor de hulp bij de metingen aan het PtRh en het beschikbaar stellen van de kristallen (met natuurlijk altijd de kans dat ze gesmolten terug komen...). Ook de bezoekers uit Leuven, Steve Helfenstyn en Patricia Deurink, worden van harte bedankt voor de prettige samenwerking en voor de moeite die zij hebben genomen om toch telkens heen en weer te rijden naar Eindhoven. Ik kan me voorstellen dat dit vooral voor Steve moeilijk is geweest met al die Nederlandse voetbalgekken tijdens de WK. Ik bedank Claude Creemers voor het uitlenen van zijn krachten en voor de pittige maar altijd interessante discussies die wij gehad hebben over het PtRh. Uit de PtRh periode komt ook de enige afstudeerder die ik heb mogen begeleiden, Mischa Nelis. Na hem zou sowieso iedere afstudeerder saai zijn geweest, dank voor deze ervaring... ik laat natuurlijk een Brand (zelf heb ik liever Duvel) voor je klaarzetten tijdens het feest. Marc Langelaar en Dik Boerma dank ik voor het beschikbaar stellen van MATCH en het mij uitleggen van belangrijkste eigenschappen ervan. Verder bedank ik Sonja Barends voor de zelfstandige manier van werken tijdens haar stage aan CuAu. Bedankt ook Rein voor de reanimatie van de electronica en de wijze lessen (als je het niet aanzet gaat het niet stuk) en Gerard voor de techniek in het algemeen, het vacuum in het bijzonder en het onbetaalbare gezicht dat je trok toen de EARISS van binnen met goud gecoat werd. Vanwege het vertroetelen van de EARISS analysator en manipulator dank ik ook Jos en Piet. Erwin bedankt voor het leveren van WordPerfect (jawel, dit proefschrift is in WP).

Natuurlijk gaat een AIO periode niet alleen over wetenschap, vandaar dat ik ook mijn groeps- en kamergenoten wil bedanken voor de fijne tijd op de TU. Als eerste bedank ik de "oude" groep: Rob, Jean-Paul en Will, de vaste krachten Wijnand, Kees en Rob, de post docs Coralie en Gunther, mijn kamergenoten Mireille en Liesbeth en van de studenten natuurlijk Birgitt. Verder bedank ik de "jonge honden": Marco, Marc en Wim. Veel dank gaat richting René, Bor en Camiel voor hun organisatietalent en drang (Iemand zin in een ATB-tochtje ? Ik heb weer tijd.. als ik tenminste niet hoef te handballen. Dank ook dus de gasten van mijn oude club Oktopus en mijn huidige honk PSV.).

Last but not least dank ik Annet, voor het geduld tot eindelijk dat *@#* proefschrift klaar was.

Curriculum vitae

29 jan. 1971   Geboren te Eindhoven

1983-1988   HAVO, Bisschop Beckers College, Eindhoven

1998-1992   Technische Natuurkunde, HTS Eindhoven, Eindhoven

1992-1995   Technische Natuurkunde, Technische Universiteit Eindhoven, Eindhoven

1996-2000   Promotieonderzoek in de groep Fysica van Oppervlakken en Grenslagen (FOG), Faculteit Technische Natuurkunde, Technische Universiteit Eindhoven, Eindhoven

sinds 2000 werkzaam bij ASML, Veldhoven